Physical properties of red blood cells in aggregation

Dissertation

im Rahmen eines Cotutelle-Verfahrens zur Erlangung des Grades
des Doktors der Naturwissenschaften
der Naturwissenschaftlich-Technischen Fakultät
der Universität des Saarlandes

Thèse

Dans le cadre d'une cotutelle pour obtenir le grade de
Docteur de l'Université Grenoble Alpes
Spécialité : Physique appliquée

Von/présentée par
François YAYA

Saarbrücken / Grenoble
2021

Tag des Kolloquiums: 04.01.2021

Dekan: Prof. Dr. Jörn Walter

Mitglieder des Prüfungsausschusses:

Vorsitzender: Prof. Dr. Rolf Pelster
Berichterstatter: Prof. Dr. Christian Wagner
Berichterstatter: Prof. Dr. Jochen Hub
Berichtstatterin: Prof Dr. Gladys Massiera

Akademischer Mitarbeiter: Dr. Herbert Wolf

Weiteres Mitglied: Dr.Thomas Podgorski
Weiteres Mitglied: Dr. Clément De Loubens
Weiteres Mitglied: Prof. Dr. Philippe Connes

Diese Arbeit wurde von der Deutsch-Französischen Hochschule (DFH)
Und CNES (Centre National d’Etudes Spatiales) finanziell gefördert.

Cette thèse a été subventionnée par l’université franco-allemande (UFA)
et le CNES (Centre National d’Etudes Spatiales).

Eidesstattliche Versicherung

Hiermit versichere ich an Eides statt, dass ich die vorliegende Arbeit selbstständig und ohne Benutzung anderer als der angegebenen Hilfsmittel angefertigt habe. Die aus anderen Quellen oder indirekt übernommenen Daten und Konzepte sind unter Angabe der Quelle gekennzeichnet. Die Arbeit wurde bisher weder im In- noch im Ausland in gleicher oder ähnlicher Form in einem Verfahren zur Erlangung eines akademischen Grades vorgelegt.

Saarbrücken, 21.09.2020

_____
François YAYA

Abstract

Physical properties of red blood cells in aggregation

by François YAYA

Red blood cells (RBC) are micron sized biological objects and the main corpuscular constituent of blood. It flows from larger arteries to very small capillaries. Utilizing a physical approach, this work aims to assess properties that govern blood flows and in particular the disaggregation and aggregation mechanisms of RBC at a single cell level. The interactions of RBCs are thus, investigated experimentally by measuring adhesive forces in the pN range in various model solutions thanks to optical tweezers. While two models for aggregation have been proposed: bridging and depletion, experimental evidence is still lacking to decide which mechanism prevails. The research presented here provides a new insight on the aggregation of RBCs and shows that the two models may not be exclusive. A complete 3 dimensional phase diagram of doublets has been established and confirmed by experiments by varying the adhesive forces and reduced cell volumes. Besides, the effect of aggregation was studied in vitro in a bifurcating microcapillary network and the distribution of aggregates and their stability in such a geometry are reported. Finally, experiments in flow allowed the characterization of the flow field around single RBCs at different velocities. Interesting vortical fluid structures have been also observed thanks to tracer nanoparticles.

Les globules rouges (GR) sont des objets biologiques de la taille du micron et l'un des principaux constituants du sang. Ils circulent des grandes artères aux très petits capillaires. En utilisant une approche physique, ce travail vise à évaluer les propriétés qui régissent les écoulements sanguins et en particulier les mécanismes de désagrégation et d'agrégation des globules rouges au niveau cellulaire. Les interactions des globules rouges sont ainsi étudiées expérimentalement en mesurant les forces d'adhésion qui sont seulement de quelques piconewtons et ce, dans différentes solutions modèles grâce aux pinces optiques. Malgré les deux modèles d'agrégation existants : le pontage et la déplétion, les preuves expérimentales font défaut. La recherche présentée ici apporte un nouvel éclairage sur l'agrégation des GR et montre que les deux modèles ne sont peut-être pas mutuellement exclusifs. Un diagramme de phase tridimensionnel complet des doublets a été établi et confirmé par des expériences en faisant varier les forces adhésives et en réduisant les volumes réduits des globules rouges. En outre, l'effet de l'agrégation a été étudié in vitro dans un réseau microcapillaire en bifurcation et la distribution des agrégats dans un tel modèle a été rapportée. Enfin, des expériences en écoulement ont permis de caractériser le champ d'écoulement autour de chaque globule rouge à différentes vitesses. Des structures de fluides en forme de vortex intéressantes ont également été observées grâce à des traceurs (nanoparticules).

Rote Blutkörperchen (Erythrozyten) sind biologische Objekte im Mikrometerbereich und der korpuskuläre Hauptbestandteil des Blutes. Es fließt aus größeren Arterien in sehr kleine Kapillaren. Unter Verwendung eines physikalischen Ansatzes zielt diese Arbeit darauf ab, die Eigenschaften zu bewerten, die den Blutfluss und insbesondere die Disaggregations- und Aggregationsmechanismen der RBC auf Einzelzellebene regeln. Die Interaktionen der Erythrozyten werden daher experimentell untersucht, indem Adhäsionskräfte im pN-Bereich in verschiedenen Modelllösungen mit Hilfe einer optischen Pinzette gemessen werden. Während mit Bridging und Depletion zwei Modelle für die Aggregation vorgeschlagen wurden, fehlen noch experimentelle Beweise, um zu entscheiden, welcher Mechanismus vorherrscht. Die hier vorgestellte Forschung liefert neue Erkenntnisse über die Aggregation von RBCs und zeigt, dass die beiden Modelle möglicherweise nicht exklusiv sind. Es wurde ein vollständiges dreidimensionales Phasendiagramm von Dubletten erstellt und experimentell durch Variation der Adhäsionskräfte und reduzierte Zellvolumina bestätigt. Außerdem wurde der Effekt der Aggregation in vitro in einem sich gabelförmigen Mikrokapillarnetz untersucht, und es wird über die Verteilung der Aggregate und ihre Stabilität in einer solchen Geometrie berichtet. Schließlich

erlaubten Strömungsexperimente die Charakterisierung des Strömungsfeldes um einzelne RBCs bei unterschiedlichen Geschwindigkeiten. Dank Tracer-Nanopartikeln konnten auch interessante wirbelartige Fluidstrukturen beobachtet werden.

Acknowledgements

First and foremost, I would like to thank my two supervisors Prof Dr Christian Wagner and Dr Thomas Podgorski for their support during this PhD cotutelle and letting me a complete freedom to do research on topics I am interested in. I started to work with optical tweezers and red blood cells during my master thesis and my job would have been more difficult without the valuable help of Dr Kisung Lee. The same person who introduced me to Prof Alexander Priezzhev from the Moscow State University. I will never forget his support and positive attitude towards our research. The same goes for his students and co-workers with whom I also enjoyed collaborating: Alexey Semenov, Petr Ermolinsky, Evgeny Shirshin and Andrei Lugovtsov. Talking about collaborations, I would like to thank the research groups from Jülich: Dimitry Fedosov, Masoud Hoore, Pavlik Lettinga, Olivera Korculanin and Mehrnaz Babaki but also the colleagues from Bayreuth: Stephan Gekle, Achim Guckenberger and Johannes Roemer for the fruitful discussions. Even if this work is new but promising to me, I also thank Laura Casanellas and Laura Casas Ferrer from Montpellier for their warm welcome and the interesting discussions during my stay.

Thanks a lot to Elke Huschens for simplifying administrative tasks, helping me improve my german (or saarländisch!) and also Karin Kretsch who made sure our experiments can run without lacking anything. A huge thanks to my lab colleagues and now lab friends from Saarbruecken and Grenoble for making every single day, an enjoyable day: Asena Abaye, Ettore Bernardi, Zakaria Boujja, Revaz Chachanidze, Viviana Claveria, Alexis Darras, Bernd Eberle, Thomas Fischer, Jorge Fiscina, Daniel Flormann, Luigi Giannelli, Rishab Handa, Sebastian Himbert, Mehdi Inglebert, Thomas John, Lars Kaestner, Alexander Kihm, Oliver Köhn, Sylvain Losserand, Julie Martin-Wortham, Javad Najafi, Mohamed Nouaman, Pankaj Pandey, Stephan Quint, Steffen Recktenwald, Francesco Rosati, Christian Ruloff, Greta Simionato, Emmanuel Terriac and Doriane Vesperini.

Finally, merci to my old time friends from France: Emrullah, Maxime, across Europe: Alex, Carla, Daniel, Joe, Marcus, Nico, Pete, Rafal, Rick, and of course my family, parents and sister for their support despite the distance and my lack of free time during this PhD.

Contents

List of Figures

List of Tables

List of Abbreviations

AFM atomic force microscopy
ATP adenine triphosphate
BSA bovine serum albumine
DNA deoxyribonucleic acid
EDTA ethylenediaminetetraaceticacid
FB Flat-Biconcave
FC Flat-Concave
FITC fluorescein isothiocyanate
HEPES 4-(2-hydroxyethyl)-1-pipérazine ethane sulfonique acid
HSA human serum albumine
LJ Lennard-Jones
LORCA Laser-assisted Optical Rotational Cell Analyzer
MAI microscopic aggregation index
MF Male-Female
NP nanoparticles
OT optical tweezers
PBS phosphate buffered saline
PDMS polydimethylsiloxane
PEG polyethylene glycol
RBC(s) red blood cell(s)
SB Sigmoid-Biconcave
SC Sigmoid-Concave
SE standard error
SEM scanning electron microscopy
SLM spatial light modulator
TEM transmission electron microscopy

Physical Constants

Avogadro number	$N_A = 6.02214076 \times 10^{23}\,\mathrm{mol}^{-1}$ (exact)
Boltzmann constant	$k_B = 1.38064852 \times 10^{-23}\,\mathrm{m}^2\,\mathrm{kg}^{-1}\,\mathrm{s}^{-2}\,\mathrm{K}^{-1}$ (exact)
Planck constant	$h = 6.62607004 \times 10^{-34}\,\mathrm{m}^2\,\mathrm{kg}\,\mathrm{s}^{-1}$ (exact)
Speed of light	$c = 2.99792458 \times 10^{8}\,\mathrm{m}\,\mathrm{s}^{-1}$ (exact)

Chapter 1

Introduction

Blood has been fascinating for humans throughout the ages. In the Greek mythology, blood coming out of the left vein of the Medusa was poisonous while the one flowing in her right arms could resurrect the dead. The purpose of blood but also whether it is healthy or noxious has always been questioned. Bloodletting i.e. getting rid of blood expecting to cure a disease is one of the example. This was performed from Antiquity until the 19th century and has been found to be harmful in the majority of cases. In the 17th century, Jean-Baptiste Denis tried to transfuse veal's blood to Antoine du Mauroy, a patient suffering from mania. Even if he survived the first transfusion, he died after the second one from a hemolytic accident. In fact, his red blood cells (RBC) underwent hemolysis. This accident showed that blood is a complex fluid that may have compatibility issues. In the same century, Malpighi and Swammerdam were the first to mention the existence of red blood cells. However, the discovery of RBC is often credited to the Dutch scientist Anthony van Leeuwenhoek for giving a better description of these cells. This discovery was made possible by his ability to manufacture single lens microscopes with a magnification of at least 250 times.

The twentieth century has been major in terms of medical techniques to deal with blood due to its better understanding. The young Antoine du Mauroy would have maybe survived if he was born in 1900. This is the year that Karl Landsteiner discovered the blood types. He was rewarded with the Nobel prize in medicine for this discovery and his date of birth was chosen to be the day of "blood donation" in the world. The two world wars, despite being deadly, brought some improvements for transfusion and blood handling with the appearance of the first anticoagulants like citrate or citrate-dextrose.

Despite having a better description of what blood is, research is still lacking to have an in-depth understanding of this complex fluid. This thesis is dedicated to the study of blood especially one particular type of cells : erythrocytes (or RBC) and their interactions between each others. Experimental work mainly using optical

tweezers (OT) and microfluidics platforms were backed up by numerical simulations. This doctoral research is split in two major parts. The first part will be dedicated to the study of red blood cells in stasis. We will emphasize on the aggregation of erythrocytes. A phenomenon that is very present in blood circulation but yet not fully understood despite the existing models and experiments. The process of aggregation affects a number of physiological processes and is considered as one of the most important factors affecting blood flow [1, 2, 3]. From a clinical point of view, understanding aggregation is crucial since this phenomenon is impaired in many diseases such as malaria [4, 5], diabetes [6, 7] or sickle cell [8, 9] disease to only cite a few. In fact, an enhanced aggregation of RBCs (hyperaggregation) is often considered as a risk factor in pathological states. To elucidate this part, we will treat of: adsorption of macromolecules onto RBC, the measurement of (dis)aggregation forces and the shape of RBC doublets.
The second part is about RBCs in flow with a focus on cells' interactions whether they are adhesive or hydrodynamic. It will deal with: the flow field around cells and the distribution of aggregates at bifurcations. But first, let us start with a detailed description of our experimental setups and with an in-depth view of the biological objects we investigate.

Introduction

Le sang a toujours été fascinant pour l'homme. Dans la mythologie grecque, le sang qui sortait de la veine gauche de la Méduse était toxique alors que celui qui coulait dans son bras droit pouvait ressusciter les morts. La fonction du sang, mais aussi son caractère sain ou nocif, a toujours été remis en question. La saignée, c'est-à-dire le fait de se débarrasser du sang dans l'espoir de guérir une maladie, en est un exemple. Elle a été pratiquée depuis l'Antiquité jusqu'au XIXe siècle et s'est révélée nocive dans la majorité des cas. Au XVIIe siècle, Jean-Baptiste Denis a tenté de transfuser du sang de veau à Antoine du Mauroy, un patient souffrant de démence. Même s'il a survécu à la première transfusion, il est mort après la seconde d'un accident hémolytique. En effet, ses globules rouges (GRs) ont subi une hémolyse. Cet accident a montré que le sang est un fluide complexe qui peut avoir des problèmes de compatibilité. Au cours du même siècle, Malpighi et Swammerdam ont été les premiers à mentionner l'existence des globules rouges. Toutefois, la découverte des GRs est souvent attribuée au scientifique néerlandais Anthony van Leeuwenhoek, qui a donné une meilleure description de ces cellules. Cette découverte a été rendue possible grâce à sa capacité à fabriquer des microscopes à lentille unique avec un

grossissement d'au moins 250 fois.
Le vingtième siècle a été majeur en termes de techniques médicales pour traiter le sang en se basant sur une meilleure compréhension de celui-ci. Le jeune Antoine du Mauroy aurait peut-être survécu s'il était né en 1900. C'est l'année où Karl Landsteiner a découvert les groupes sanguins. Il a été récompensé par le prix Nobel de médecine pour cette découverte et sa date de naissance a été choisie pour être le jour du "don du sang" dans le monde. Les deux guerres mondiales, bien que meurtrières, ont apporté quelques améliorations relatives aux transfusions et la manipulation du sang avec l'apparition des premiers anticoagulants comme le citrate ou le citrate-dextrose. Bien que l'on dispose d'une meilleure description de ce qu'est le sang, la recherche manque encore pour comprendre en profondeur ce fluide complexe. Cette thèse est consacrée à l'étude d'un type particulier de cellules : les érythrocytes (ou globules rouges) et leurs interactions entre elles. Des travaux expérimentaux utilisant principalement des pinces optiques et des plateformes microfluidiques ont été complémenté par des simulations numériques. Ce travail de recherche est divisé en deux grandes parties. La première partie est consacrée à l'étude des globules rouges en stase. Nous mettrons l'accent sur l'agrégation des érythrocytes. Un phénomène très présent dans la circulation sanguine mais encore mal compris malgré les modèles et les expériences. Pour élucider cette partie, nous traitons de : l'adsorption de macromolécules sur les globules rouges, la mesure des forces de (dés)agrégation et la forme des doublets des globules rouges.
La deuxième partie concerne les GRs en flux en mettant l'accent sur les interactions des cellules, qu'elles soient adhésives ou hydrodynamiques. Nous abordons également : le champ d'écoulement autour des cellules et la distribution des agrégats aux bifurcations. Mais tout d'abord, commençons par une description détaillée de nos installations expérimentales et par une vue approfondie des objets biologiques que nous étudions.

Einleitung

Blut hat den Menschen schon immer fasziniert. In der griechischen Mythologie war das Blut, das aus der linken Ader der Medusa austrat, giftig, während das Blut, das in ihrem rechten Arm floss, Tote auferwecken konnte. Die Aufgabe des Blutes, aber auch seine Gesundheit oder Schädlichkeit wurde immer in Frage gestellt. Das Aderlassen, d.h. die Entnahme von Blut in der Hoffnung, eine Krankheit zu heilen, ist ein Beispiel dafür. Sie wurde von der Antike bis ins 19. Jahrhundert praktiziert und hat sich in den meisten Fällen als schädlich erwiesen. Im 17. Jahrhundert versuchte

Jean-Baptiste Denis, dem an Demenz erkrankten Antoine du Mauroy Kalbsblut zu transfundieren. Obwohl er die erste Transfusion überlebte, starb er nach der zweiten an einem hämolytischen Unfall. Seine roten Blutkörperchen (Erythrozyten) wurden einer Hämolyse unterzogen. Dieser Unfall zeigte, dass Blut eine komplexe Flüssigkeit ist, die Kompatibilitätsprobleme haben kann. Im gleichen Jahrhundert waren Malpighi und Swammerdam die ersten, die die Existenz roter Blutkörperchen erwähnten. Die Entdeckung der roten Blutkörperchen wird jedoch oft dem niederländischen Naturforscher Anthony van Leeuwenhoek zugeschrieben, der diese Zellen besser beschreiben konnte. Diese Entdeckung wurde durch seine Fähigkeit ermöglicht, Einlinsenmikroskope mit mindestens 250-facher Vergrößerung herzustellen.
Das zwanzigste Jahrhundert war aufgrund seines besseren Verständnisses für die medizinischen Techniken im Umgang mit Blut von großer Bedeutung. Der junge Antoine du Mauroy hätte vielleicht überlebt, wenn er 1900 geboren worden wäre. Dies ist das Jahr, in dem Karl Landsteiner die Blutgruppen entdeckte. Für diese Entdeckung wurde er mit dem Nobelpreis für Medizin ausgezeichnet, und sein Geburtsdatum wurde zum Tag der "Blutspende" in der Welt gewählt. Die beiden Weltkriege brachten, obwohl sie tödlich waren, mit dem Erscheinen der ersten Antikoagulanzien wie Citrat oder Citrat-Dextrose einige Verbesserungen für Transfusionen und den Umgang mit Blut. Trotz einer besseren Beschreibung dessen, was Blut ist, mangelt es der Forschung immer noch an einem vertieften Verständnis dieser komplexen Flüssigkeit. Diese Arbeit widmet sich der Untersuchung eines bestimmten Zelltyps: der Erythrozyten (oder RB) und ihrer Interaktionen untereinander. Die experimentellen Arbeiten, die hauptsächlich mit optischen Pinzetten und Mikrofluidik-Plattformen durchgeführt wurden, wurden durch numerische Simulationen untermauert. Diese Doktorarbeit ist in zwei Hauptteile gegliedert. Der erste Teil ist dem Studium der roten Blutkörperchen in Stase gewidmet. Wir werden uns auf die Aggregation von Erythrozyten konzentrieren. Ein Phänomen, das im Blutkreislauf sehr präsent ist, aber trotz Modellen und Experimenten noch nicht vollständig verstanden wird. Um diesen Teil zu erläutern, werden wir folgende Themen behandeln: Adsorption von Makromolekülen an RBC, die Messung von (Dis-)Aggregationskräften und die Form von RBC-Dubletten.
Im zweiten Teil geht es um RBC in Strömung, wobei der Schwerpunkt auf den Interaktionen der Zellen liegt, unabhängig davon, ob sie adhäsiv oder hydrodynamisch sind. Wir beschäftigen uns mit: dem Strömungsfeld um Zellen und der Verteilung von Aggregaten an Bifurkationen. Beginnen wir jedoch zunächst mit einer detaillierten Beschreibung unserer Versuchsaufbauten und mit einer eingehenden Betrachtung der biologischen Objekte, die wir untersuchen.

1.1 Literature review

RBC aggregation since its discovery by Leeuwenhoek, is still a relevant subject. One way to "assess" aggregation, is to use the sedimentation rate. Even nowadays this is still a diagnosis tool for medical doctors. It has been observed that pathological blood often sediment faster than healthy blood. This is often attributed to the higher concentration of fibrinogen due to the inflammatory response [10, 11] of the body to a disease. Fibrinogen is responsible of the aggregation of RBC but it may not be the only factor and understanding the mechanisms of RBC aggregation becomes crucial in this context.

The easiest system to study the aggregation of RBCs consists of a cluster of two cells : the doublets. Numerical work has helped to acquire more knowledge taking into account specific physical parameters such as : contact area, volume but also shear elasticity and bending rigidity. A lot has already been done in this area but it was mainly supported by 2 dimensional analysis [12]. Initial models were considering the contact area between two RBCs to be plane. In fact, it is more subtle and a whole phase diagram has been discovered in 2 dimensions. Our recent work propose an entire phase diagram in a 3 dimensional space.

A first outlook on aggregation was made using techniques dedicated to the rheology of blood. This revealed the collective behaviour of RBCs in blood flow (Rheoscan-A, Myrenne Aggregometer [1], ektacytometer [13], LORCA [14]. One of the most significant result related to aggregation is, for instance, what is now described as blood shear-thinning. This phenomenon is attributed to dissociation of rouleaux under shear stress. Other techniques are also available to study aggregation from the most simple ones like microscopic image analysis [15] to more elaborate ones like laser beam scattering [16, 17, 18] or ultrasound scattering [19, 20] onto blood suspensions. Nevertheless, even if such techniques are useful to investigate both the aggregation and disaggregation of RBCs in a controlled manner by varying the shear stress, they fail to explain at a cellular level both phenomena and more local techniques become necessary. Single cell methods (AFM [21, 22], micropipet aspiration [23]) mostly focus on the disaggregation of RBCs. Compared to other methods [24, 25, 26, 21], OT allow a better control of the interaction area in diverse model solutions and thus, for both the aggregation and disaggregation process.

One of the way to promote aggregation between RBCs is the use of polymers. Early work by Chien et al. [25, 27], supported the hypothesis in which RBCs from

larger clusters by forming bridges between each others. Chien et al. favor a model based on the adsorption of macromolecules or proteins onto adjacent cell membranes and the formation of cross-bridges giving birth to the rouleaux formation. It is therefore, important to take into account the adsorption to verify this hypothesis. Experimental evidence has been considered as controversial and regarded as artefacts [28] and thus, neglecting the possible formation of bridges. More recent work by Neu et al. [29], rests on depletion forces. The difference in the concentration of macromolecules between the depletion layer and surrounding medium causes osmotic pressure pushing the RBCs between each other. Experimental work has been conducted in plasma and non-ionic polymers [30].

With the emergence of physical techniques to measure forces, questions about RBCs interactions at a single-cell level have been better addressed. Micropipette aspiration techniques have given a first insight about RBC interactions but they were carried out on liposome - RBC pairs [24] instead of RBC - RBC. Experiments with AFM revealed quantitatively the range of RBC interaction energy but found its limits at high concentrations of dextran. On a side note, all the single-cell methods are mechanical and only allow the measurement of disaggregation between cells. OT have shown to be versatile for measuring forces as they could be combined with other existing methods [31, 32, 33]. Several studies have reported about the assessment of forces between RBCs. OT opened new possibilities as it allows to control the dynamics of RBCs aggregation but also disaggregation [34, 35, 30]. Differences between the two mechanisms in terms of forces have already been shown but there is an absence of experimental evidences to verify the models and especially, in model solutions. The same lack can be found for the duration of interaction between the cells. Some work has already been done on this matter, showing that interaction energy may become greater after longer interaction time-spans but was still in early stage [30].

Force measurements are insightful but the (dis)aggregation of RBCs takes place in blood flow and the influence of hydrodynamic forces on shape and stability of aggregates cannot be neglected. To tackle this problematic, the development of microfluidic platforms have found a rising interest in blood research. Experiments in capillaries revealed that RBC's membrane could deform while travelling in narrow channels and give birth to several shapes. Early simulations [36, 37, 38, 39, 40] in 2D, modelled RBCs by considering them as vesicles. The flow field around a single RBC has already been simulated and a complete phase diagram has been established, showing the presence of a plethora of RBC shapes [38, 39]. This results were later

confirmed in 3D by Fedosov et al. [41]. Among all these possible shapes, two of them have been studied more in depth namely croissant and slippers. Experiments and simulations in 3D [42, 43] showed that these shapes are the most prominent in microchannels for, respectively, lower and higher cell velocities. However, despite the numerical work, the flow field around a single RBC and in particular, around these two prominent shapes has never been studied since the pioneer work of Gaehtgens et al. [44] although it is of utmost importance for the understanding of cell-cell interactions in flow. The flow field around hydrodynamically formed doublets is also lacking. In fact, experiments relying on the adhesive forces forming clusters in microchannels are rather new [45]. Even if the adhesive and hydrodynamic force contributions is better known in vitro for straight channels, more needs to be achieved in more complex geometries mimicking blood capillaries e.g. with bifurcations. It remains unclear how such bifurcations influence the blood rheology at a microscopic and more local scale by determining the actual distribution of aggregate sizes.

1.2 Blood composition

Blood represents about 7 % of our body weight. It is a non Newtonian fluid conveying necessary nutrients but also oxygen in the whole body. As depicted on Fig. 1.1, it is composed of:

- Plasma: This is the medium in which cells and proteins travel. Its volume fraction in blood depends from one individual to an other but is on average 55%. Water is the most present element and constitutes about 92 % of the volume. The remaining 8 % is mostly proteins. Albumin is the most prominent protein in plasma. However, the one held responsible for aggregation is mainly fibrinogen. It also contains various electrolytes such as sodium and chloride to keep osmolality at an optimum level. Other nutrients like glucose or amino-acids can also be found.

- Red blood cells: They are the most abundant cells in blood. Their volume fraction is about 45% of blood and vary between men and women and more generally between individuals. It is on average lower for women and is also influenced by many factors (e.g. life in altitude, physical activity...). The hematocrit is a valuable parameter since it is often in deficit for pathological cases. The purpose of RBCs is to transport oxygen through vessels into the whole body. Its color is due to the hemoglobin present in it, as the red wavelength is

the less absorbed. Hemoglobin molecules also have an iron component which helps capturing the oxygen thanks to its chemical affinity.

- Buffy coat: It is about 1% of the total volume and it contains about 0.2% of white blood cells (leukocytes), which are part of the immune system and remove obsolete cells. Platelets or thrombocytes (between 0.6 and 1%) are also present and make clotting possible after an injury, for example.

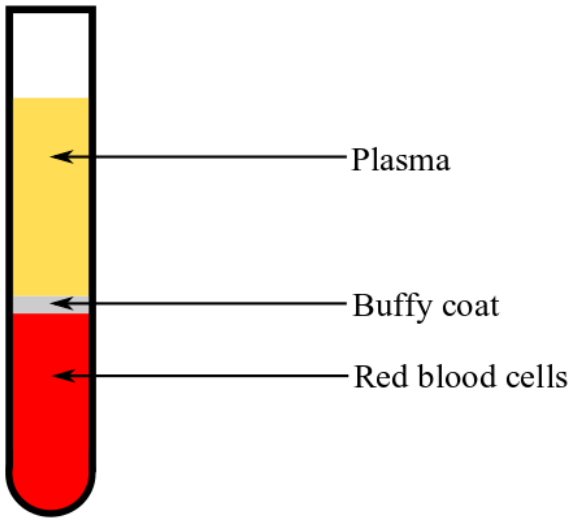

FIGURE 1.1: Scheme of a blood tube after centrifugation. 3 layers are separated by density. From top to the bottom: plasma, buffy coat (platelets, white blood cells) and red blood cells

1.3 Focus on the RBC

The formation of RBCs also known as erythropoiesis, takes place in the bone marrow and last about 5 days. It all starts with hemocytoblasts, a hematopoietic stem cell able to differentiate into different lines of blood cells. They are self-regenerating cells as they give birth to other cells of the same nature but also myeloid progenitors. From these cells, proerythroblasts get formed and go through different stages (basophilic, polychromatic and orthochromatic or normoblasts). At this stage, the nucleus is ejected and give rise to another type of cells called reticulocytes. These cells are expelled from the bone marrow and start traveling in the whole body. After maturation, these same cells become RBC (erythrocytes).
After circulating for about 120 days, senescent RBCs are detected by macrophages

and undergo erythrophagocytosis, a process during which senescent RBCs are engulfed by macrophages. They are then, mostly transported to the spleen where they will have to pass through very narrow channels. This causes the rupture of the RBCs and hemolysis takes place. During the process, hemoglobin contained in the RBC is released and salvaged. This summarizes the journey of a RBC during 120 days.

A healthy RBC has a biconcave shape at rest [46] but due to its deformability it can take other shapes such as slippers or parachutes in flow [43, 42]. Elementary geometrical parameters (Table 1.1) can be summarized as:

Diameter	$7.62 \pm 0.62 \mu m$	[47]
Minimum thickness	$0.81 \pm 0.35 \mu m$	[47]
Maximum thickness	$2.58 \pm 0.27 \mu m$	[47]

TABLE 1.1: Geometric properties of human red blood cells

The RBC membrane can be divided in three parts:

- Glycocalyx: This is the outer membrane present in a RBC. It is comparable to a brush of carbohydrates or saccharides.
- Phospholipid bilayer: It is a polar and double layer of lipid molecules. The head is hydrophilic while the tail is hydrophobic. It is also constituted of transmembrane proteins such as band 3 depicted in Fig. 1.2. Band 3 promotes the ion exchanges between the outer and inner environment of the cell but also regulates protein-protein interactions. Others like glycophorins carry sugar molecules.
- Membrane skeleton: We find proteins such as actin or larger ones like spectrin which is also the most abundant one in this layer. They help to keep the shape of the RBC and form the cytoskeleton.

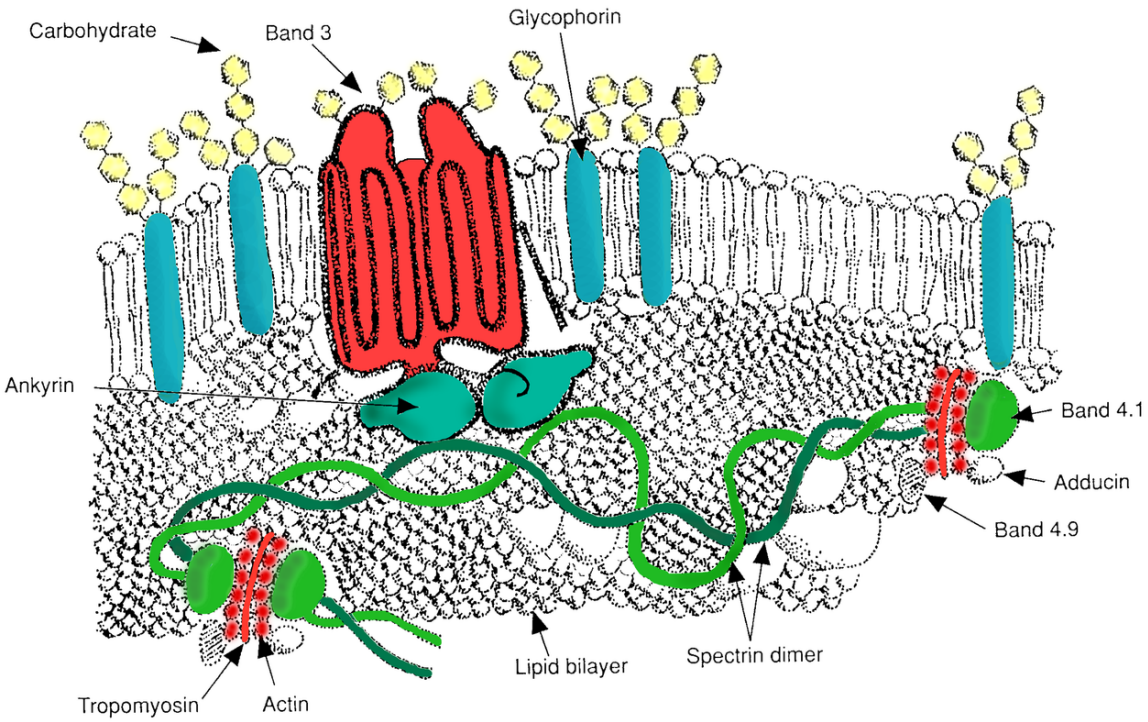

FIGURE 1.2: Sketch of the RBC membrane featuring from the top to the bottom : the glycocalyx mainly constituted of carbohydrates, phospholipidic bilayer and the membrane (actin, spectrin,...)

1.4 Aggregation

The aggregation of RBCs refers to the formation of cell clusters also known as "rouleaux". The term "rouleau" was used as RBCs form structures that resemble a stack of coins (Fig. 1.3). This entire process was studied by Fahraeus [11]. He understood that aggregation is directly linked to sedimentation rates. He observed that the formation and density of rouleaux is very often more acute for pathological blood and that at the same time sedimentation is faster. In pathological cases, the sedimentation time is shorter due to the formation of rouleaux falling faster than single RBC. This observation is still crucial in modern medicine as it is a diagnostic tool used by medical doctors to detect eventual diseases. Although it is a rather non-specific marker, it is now understood that inflammation, leading to higher fibrinogen levels [48, 10], is responsible of this aggregation increase.

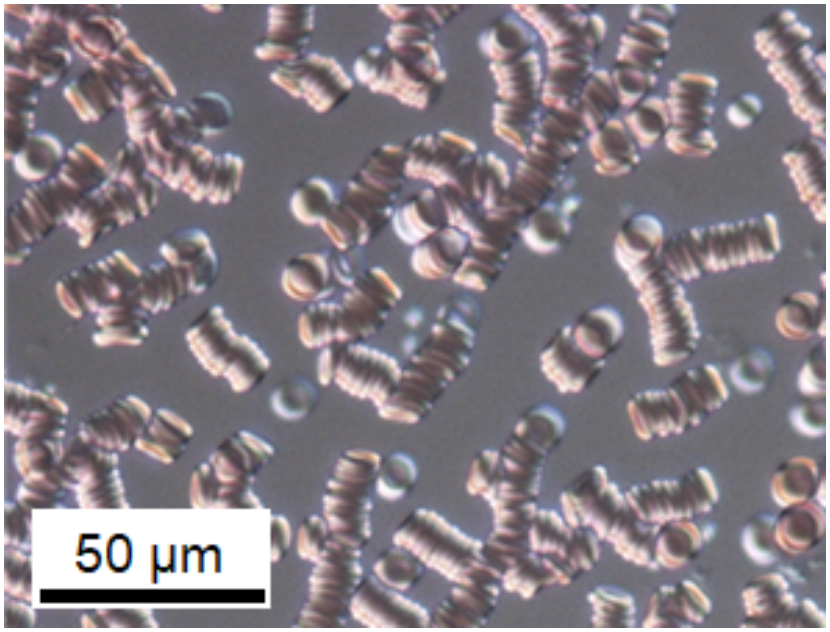

FIGURE 1.3: Microphotography of rouleaux seen under the microscope with a x40 objective

Comparisons regarding aggregation in other mammals have already been carried out and the results are somehow surprising. It shows that blood drawn from healthy horses have stronger aggregation, whereas calf or sheeps' blood have very low to no rouleaux formation at all [49, 50]. Nevertheless, their size and mechanical properties may be different and also play a role in aggregation. The underlying mechanism of RBCs aggregation, whether its for animals or humans remains unclear. Nevertheless, two models are privileged to describe rouleaux formation. These two models are **bridging and depletion**. The former relies on the adsorption of macromolecules onto the surface of RBCs causing their aggregation when the bridging forces overcome the electrostatic forces. The latter is based on the exclusion of macromolecules near the surface of RBCs leading to a gradient in osmotic pressure and also aggregation.

1.4.1 Aggregating factors

Fibrinogen has often been presented as the principal protein responsible of RBC aggregation. Nevertheless, other proteins such as γ -globulins show a similar behavior promoting aggregation. Albumine is also presented as an inhibitor in the literature but in presence of other proteins it can also be a promoter of aggregation. These examples show that aggregation, even at the protein level, is a complex process.

Different aggregating factors can be found in human plasma. They are in fact proteins of various nature. They all contribute in different ways to the aggregation of RBCs. Even though the effect of some are debatable, Table 1.2 lists some of them:

Antagonist	Molecular Weight (kDa)	Concentration (mg/mL)	Effect
Fibrinogen	340	1.8-4.0	$\uparrow$
Albumine	66	35-50	$\uparrow\downarrow$
γ -globulins	150	7-16	$\uparrow$
CRP	25	<0.006	$\uparrow$ (?)

TABLE 1.2: Proteins responsible of the aggregation in human plasma, their concentration and their effect on aggregation (whether it enhances $\uparrow$ or diminishes $\downarrow$)

Working with autologous plasma or serum can be achieved relatively with ease but to understand rouleaux formation within a physical approach, this system needs to be simplified as it involves too many factors. Therefore, model solutions such as dextran in buffer are often preferred over plasma. Dextran is a colloidal polymer from the glucan family. It is used in medicine as a volume expander [51] as a replacement for blood after severe losses. Even though, it can be found in the dental plaque, its production is now controlled via bacteria and thus, allowing mass production. It is a particularly versatile polymer by the fact that aggregation strength can be tweaked by varying the concentration and dextran of several molecular weights can be easily produced. We use it as a cross-bridger and more details on this aspect have been already exposed in 1.1. However, dextran has been used in experiments to verify both **depletion and bridging** models. For this reason, the aggregation mechanisms taking part in presence of dextran is still controversial.

Fd-virus wild type has been chosen as a long range depletant in our experiments for its well-known properties with a strong background in colloidal physics [52, 53, 54]. Fd-virus has a high aspect ratio due to its filamentous and rod-like structure (see Fig. 1.4). Its shape has been shown to be ideal to increase the range of the depletion interaction compared to spherical particles for example and therefore, is considered as a long range depletant due to its geometry and size. This system is also well-defined and numerical simulations can describe depletion potentials using first-order density approximation up to an Fd content of several overlap concentrations. Equations between two spheres or two plates have already been derived and can be applied to such system. Experiments using Total Internal Reflection Microscopy (TIRM) [55, 56] confirmed with accuracy the potential profile of such

depletion interaction.

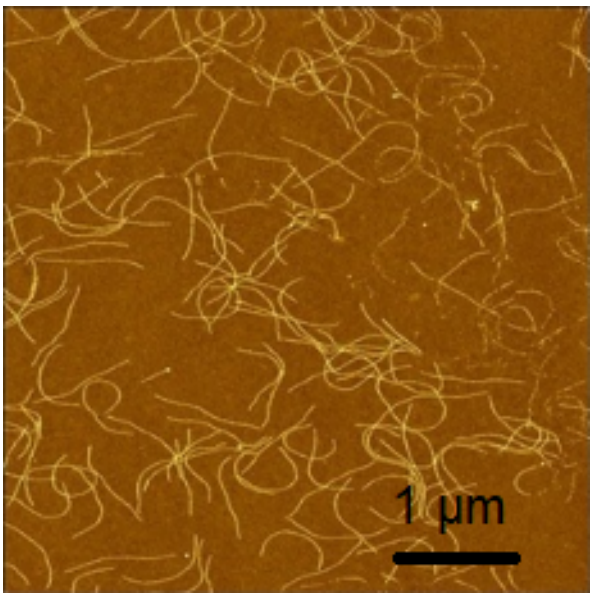

FIGURE 1.4: AFM image on a silica substrate of Fd-virus taken from [57]

1.5 Model descriptions

Over the last decades, diverse techniques have emerged attempting to make a breakthrough related to aggregation. One idealistic way to solve this problem would be to have a look at the gap between two aggregating RBCs. This is what Jan and Chien [15] did using scanning electron microscopy (SEM). They showed the dependence of inter-cellular distance in rouleaux with respect to the molecular weight of dextran (Fig. 1.5). This could indicate that dextran molecules are situated between cells and the interstitial gap would be bigger for higher molecular weights.

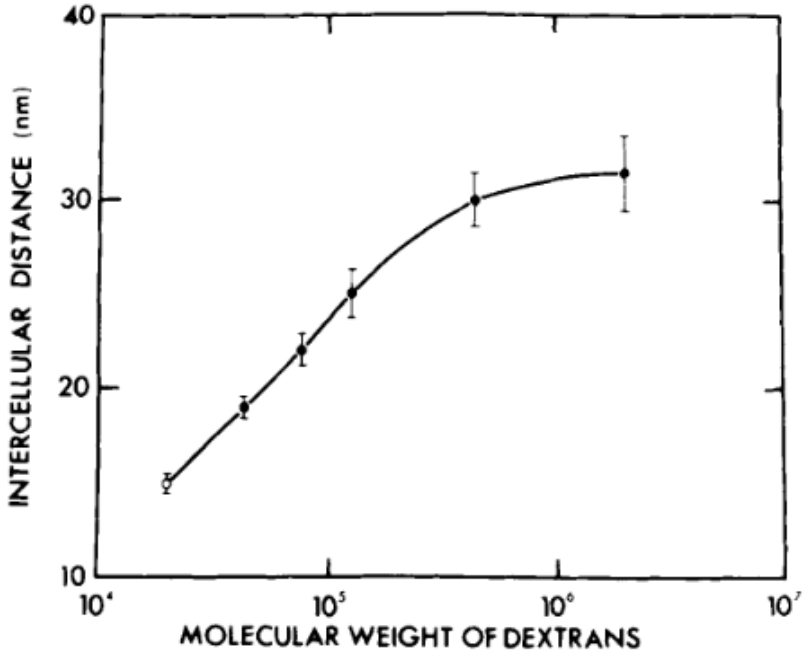

FIGURE 1.5: Intercellular gap as a function of dextran molecular weight. Graph taken from [15]

However, there was no clear observation of such 'bridges' and the gap seems to remain the same at higher molecular weight of dextran. To overcome this issue, some tried to look for hints or signatures instead. If bridging occurs, one could expect to see eventual adsorption of macromolecules onto the cells. It could be a hint for bridges remaining on the surface of RBCs. Despite some artifacts [28], different methods showed that adsorption of dextran takes place on the surface of RBCs. This is a convincing result but is unfortunately not enough to generalize it to plasma as the nature of proteins are different compared to dextran. Looking at the interaction energy for aggregation and disaggregation is also a possible way to discriminate **bridging** from **depletion**. One analogy would be to think about two glass slides brought into contact by a drop of water, there would not exist any difference in terms of interaction energy whether we pull a glass slide from the other or we push one onto the other in the direction of its length, as the interaction energy would depend only on the instantaneous distance between surfaces. Single cell experiments with micropipettes exhibited distinct interaction energies for aggregation and disaggregation. The relation between the interaction energy for two adhering cells as a function of the concentration of dextran is well known. It has a so called "bell shape" [58, 59, 60]. For low concentrations of dextran, there is little to no aggregation. Increasing the concentration of dextran macromolecules increases

the interaction energy between RBCs until it reaches a peak and decreases after that, as more dextran is added.

1.5.1 Bridging

S. Chien et al. [60, 15, 61, 62] supported the model of aggregation by cross-bridging. Two adjacent RBCs would interact by forming bridges in between the membranes. RBCs were put into macromolecule solutions with different macromolecular weights and were imaged using Transmission Electron Microscopy (TEM). This revealed that the intercellular distance varies depending on the macromolecule sizes [15]. Adding up to this, another characteristic of this model is therefore the adsorption of these macromolecules onto the RBCs to form bridges in between the two membranes. It was shown by Chien et al. [62] that neutral polymers such as dextran can adsorb onto the surface of RBCs.

One of the first explanation of the "bell shape" was attributed to the electrostatic forces that were investigated measuring the electrophoretic mobility and zeta potential on the surface of RBCs [15]. To better understand what forces are involved in the aggregation of RBCs in presence of dextran, Chien and Jan [15] summarized it as:

$$F_a = F_b - F_e - F_s - F_m \tag{1.1}$$

With F_a the net aggregating force, F_b the bridging force, F_e the electrostatic force, F_s the mechanical shear force and F_m the membrane bending force of RBCs.
The effective charge of erythrocytes' surface is negative mainly due to the presence of sialylated glycoproteins [63]. Past a certain threshold (peak of the bell shape), the electrostatic repulsion increases as more dextran is added to the solution. This causes a gradual decrease of the **bridging** forces and weakens the aggregation. Whereas for **depletion**, the bell shape is based on the penetration of macromolecules in the glycocalyx [29].

The nature of the bonding and the creation/destruction of those bridges remain unclear but two main ideas emerged. One is based on bridges getting formed and distributed homogeneously on the surface of the RBC, the other one promotes the idea that certain proteins bind on specific sites.

Non specific binding

In their recent work, Bagchi et al [64] proposed a model based on non-specific cross-linking. Similarly to chemical reactions, they used reaction rates to describe the formation of bonds. Figure 1.6 is a schematic representation of the model. These bonds are considered as homogeneously distributed with a density n_b Each bond was represented as Hookean spring and the force per bond f_b is therefore given by:

$$f_b = k_b\,(l - l_0) \tag{1.2}$$

l_0 is the initial length of the bond and l its stretched length. k_b refers to the spring constant of one bond. The reaction equation governing this system:

$$\frac{\partial n_b}{\partial t} = 2[k_+(n - \frac{n_b}{2})^2 - k_- n_b^2] \tag{1.3}$$

k_+ and k_- are respectively the forward and reverse reaction rate coefficients. n the density of cross-linking molecules on the membrane.

$$k_+ = k_+^0 e^{-\frac{k_{ts}(l-l_0)^2}{2k_BT}} \tag{1.4}$$

if $|x| = l < l_t$

$$k_- = k_-^0 e^{-\frac{(k_b-k_{ts})(l-l_0)^2}{2k_BT}} \tag{1.5}$$

where k_+^0 and k_-^0 are the rate coefficients at equilibrium, k_{ts} is the transition spring constant, k_b is Boltzmann's constant, T is the absolute temperature and l_t is the threshold distance below for bond formation assumed to be $l_t = 2l_0$

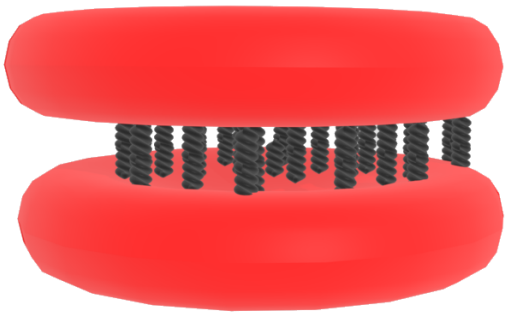

FIGURE 1.6: 3D sketch illustrating the non specific binding of proteins. Here, black bridges would bind on any site available. No particular interaction between bridges (proteins) is envisaged

Specific binding

Regarding human plasma, fibrinogen is seen in literature [65] as one of the main protein inducing RBCs aggregation. It is suspected to bind onto RBCs membranes [66, 67] and this process could be specific [68, 69]. Figure 1.7 illustrates this model. To a larger extent, one can speculate that proteins in plasma may interact in a same manner.

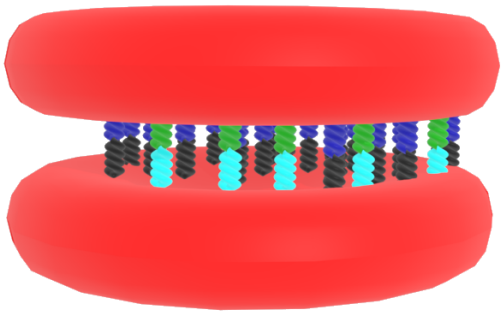

FIGURE 1.7: 3D sketch illustrating the specific binding of cells. In this example, cyan bridges would only interact with green ones and blue bridges with black ones. Each bridge would have its own type of site where it can bind

Based on previous work [70], Pereverzev et al. [71] proposed a two pathways model in an attempt to describe the binding of P- and L- selectins to oligosaccharide ligands. In their model, they show that receptor-ligand binding can be governed by "slip" and "catch" bonds. "Slip" bonds are subject to shorter lifetimes as the tensile force increase. Counter-intuitively, "catch" bonds see their lifetime enhanced as the tensile force increases until it reaches a critical force. One imaginative way to look at it is to think about chinese fingertraps. It's a toy in which one puts his/her finger and gets trapped if this finger is removed too quickly from the trap.

1.5.2 Depletion layers

The depletion model is supported by AFM measurements on single RBCs. However, it is subject to artifacts as energy quantification [12] may be influenced by the viscosity of the solution. Viscosity obviously changes as a function of the concentration of dextran macromolecules. The "bell shape" can also be reproduced qualitatively but the maximum for interaction energy together with the minima are often shifted from one technique to the other. In order to find this 'bell-shape' behavior the depletion model from Asakura and Oosawa [72] was adapted by Meiselman et al. [29] introducing penetration depth. It takes into account the fact that polymers can more or less penetrate the brushes of the RBC's membranes. Still, AFM promotes dissociation of RBCs in 'face to face' manner which is not really representative of what happens under physiological conditions, where all relative orientations can occur. With the emergence of optical tweezers, new measurements have been performed to elucidate the underlying mechanisms of RBCs' aggregation [73, 30, 35]. It allows RBCs to aggregate in a similar fashion to what happens in vessels (increasing contact area between two aggregating cells). It is also a non invasive method to measure both aggregation and disaggregation in which several parameters can be controlled (relative orientation, approach velocity). Even though depletion theory has strong grounds in the scientific community, experimental evidences are lacking. The fact that there is RBC aggregation despite their membranes being negatively charged and thus, repulsive, makes it even more interesting. This following section gives a 'case study' with detailed explanations for each model.

Interaction between two hard spheres

The well-accepted and more recent model relies on depletion layers. It was initially introduced by Asakura et al. [72]. It finds its roots in statistical physics as the system

is a canonical ensemble and consists of a large number of objects. To understand the fundamentals of depletion theory [74], let us start with an ideal case. We consider a simplified model, in which two large spheres are immersed in a solution of hard spheres (Fig. 1.8).

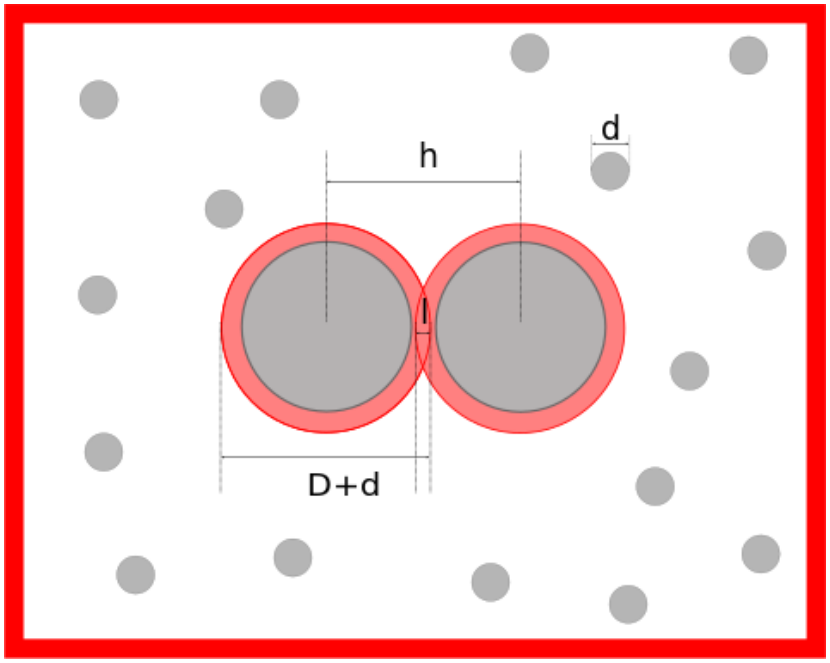

FIGURE 1.8: Scheme for the calculation of the depletion forces between two big spheres with a diameter D in a solution constituted of multiple small spheres with a diameter d. Their center to center distance is h and l represents half the width of the region formed by the two overlapping spheres in red

The forbidden volume which can't be accessed is "roughly" the volume of surrounding small spheres with a diameter d together with the volume of the larger spheres with a diameter D given by V_F:

$$V_F = \frac{\pi(D+d)^3}{6} \tag{1.6}$$

We define h as the distance between centres of two big spheres. For more accurate calculations, this volume needs to be reduced by the overlapping volume V_O which leads to a reduced volume $V_{F'}$:

$$V_{F'} = V_F - V_O = V_F - \frac{2\pi l^2}{3}\left[\frac{3(D+d)}{2} - l\right] \tag{1.7}$$

$$l = \frac{D+d}{2} - \frac{h}{2} \tag{1.8}$$

l represents half the width of the region formed by the two overlapping spheres in red (see Fig. 1.8).

The partition function Z for our canonical ensemble of identical small spheres is:

$$Z = \frac{1}{N!h^{3N}} \int e^{-\beta(T+\nu_p)} d\Gamma \tag{1.9}$$

where $\beta = \frac{1}{k_B T}$, N is total number of small spheres, h Planck's constant and T the temperature, ν_p the potential energy and Γ the phase space or Gibbs ensemble. After rearranging, solving the integral and neglecting the interaction between small and big spheres, we end up with:

$$Z = \frac{V_A^N}{N!\Lambda^{3N}} \tag{1.10}$$

with Λ being the De Broglie wavelength $\Lambda = \frac{h}{\sqrt{2\pi m k_B T}}$ and V_A being the volume that can be accessed by the center of small spheres and m their mass.

The Helmholtz free energy is defined as:

$$F_H = -k_B T \ln Z \tag{1.11}$$

$$F_H = -k_B T \ln \frac{V_A^N}{N!\Lambda^{3N}} \tag{1.12}$$

Using Stirling's approximation which is valid for $N >> 1$, $lnN! \approx N \ln N - N$

we get the Helmholtz free energy F_H:

$$F_H = -Nk_B T(1 - \ln(\frac{N\Lambda^3}{V})) - Nk_B T \ln(\frac{V_A(h)}{V}) \tag{1.13}$$

From here, two configurations are possible:
- Big spheres are enough separated to let small spheres penetrate in between them.
- Big spheres are too close and small spheres cannot get between them.

Mathematically and in the same order V_A can be seen as the difference between the total volume V and the forbidden volume V_F:

$$V_A = V - V_F, \qquad h \geq d + D \tag{1.14}$$

or

$$V_A = V - V_F + \frac{\pi}{6}(D + d - h)^2(D + d + \frac{h}{2}), \qquad h < d + D \tag{1.15}$$

We can then linearise and approximate:

$$ln(\frac{V_A}{V}) \approx -\frac{V_F}{V} + \frac{\pi}{6V}(D + d - h)^2(D + d + \frac{h}{2}) \tag{1.16}$$

As we known from thermodynamics that:

$$F_{dep} = -\left(\frac{\partial F_H}{\partial h}\right)_T \tag{1.17}$$

We finally get the depletion force F_{dep} (only if big spheres are close enough):

$$F_{dep} = \frac{N}{4V} k_B T \pi (D + d - h)(D + d + h) = -p_o S \tag{1.18}$$

Nevertheless, this model shows its limits in the case of RBCs and needs to be better defined. This is what Neu and Meiselman did, based on the depletion theory from Vincent et al. [75].

Penetration depth and interaction of RBC

For a more accurate model, RBCs cannot be considered as hard spheres. RBCs are known to be very flexible objects and their structure is more complex than spheres. The glycocalyx of the cell is made of polysaccharides and the surrounding macromolecules can penetrate into that outer layer. However, the system is considered non absorbing. Taking into account the elastic free energy of RBCs but also the osmotic forces exerted on its surface by the surrounding macromolecules, Vincent et al. [75] determined the depletion layer thickness to be:

$$\Delta = -\frac{1}{2}\frac{\Pi}{D} + \frac{1}{2}\sqrt{(\frac{\Pi}{D})^2 + 4\Delta_0^2} \tag{1.19}$$

with Δ_0 the depletion thickness for vanishing polymer concentrations. In the case of dextran it is taken to be 1.4 R_g the radius of gyration. Π is the osmotic pressure and D is a parameter which is dependent of the bulk polymer concentration and is given by:

$$D = \frac{2k_B T}{\Delta_0^2}(\frac{c_2^b N_a}{M_2})^{\frac{3}{2}} \tag{1.20}$$

M_2 is the molecular weight of the macromolecules in the solvant and c_2^b the bulk polymer concentration. k_B and N_a respectively Boltzmann and Avogadro's constant.

Despite the lack of information on the penetration depth, one can expect its form to be as:

$$p = \delta(1 - e^{\frac{c_2^b}{c_2^p}}) \tag{1.21}$$

c_2^p is the penetration constant.
Let δ be thickness of the glycocalyx and d the cell to cell distance. The energy of interaction, taking into account the possible penetration of the glycocalyx, is this time calculated as:

$$w_D = -2\Pi(\Delta - \frac{d}{2} + \delta - p) \tag{1.22}$$

The surface of a RBC is negatively charged and thus, electrostatic repulsion needs to be taken into account in the process of aggregation. The electrostatic free energy w_E is as follows:

We can distinguish two cases: - $d \geq 2\delta$

$$w_E = sinh(\kappa\delta)e^{\kappa\delta - \kappa d} \tag{1.23}$$

- $d < 2\delta$

$$w_E = (2\kappa\delta - \kappa d) - e^{-\kappa\delta}sinh(\kappa\delta - \kappa d) - sinh(\kappa\delta)e^{-\kappa d} \tag{1.24}$$

Finally, based on the depletion theory, we can sum up the aggregation as the addition of both electrostatic w_E and interaction w_D energy taking into consideration the possible penetration of the glycocalyx. We denote it as w_{total}

$$w_{total} = w_D + w_E \tag{1.25}$$

The fact that macromolecules may penetrate the glycocalyx plays a major role in explaining the so called "bell-shape" behavior of the interaction energy for a given concentration of macromolecules.

Depletion induced by an ideal polymer

To get a better description of our system, the two interacting membranes of RBCs can be approximated as two plates and dextran as an ideal polymer with a radius of gyration R_g and M_w its molecular weight (Fig. 1.9). Due to its complex geometry, this quantity is useful to grasp the size of a given polymer. The radius of gyration is the distance between a given axis of rotation and a point with the same mass as the polymer must be placed in order to have the same moment of inertia as this polymer. For dextran and using Kuhn–Mark–Houwink–Sakurada equations [76, 77] it can be expressed as:

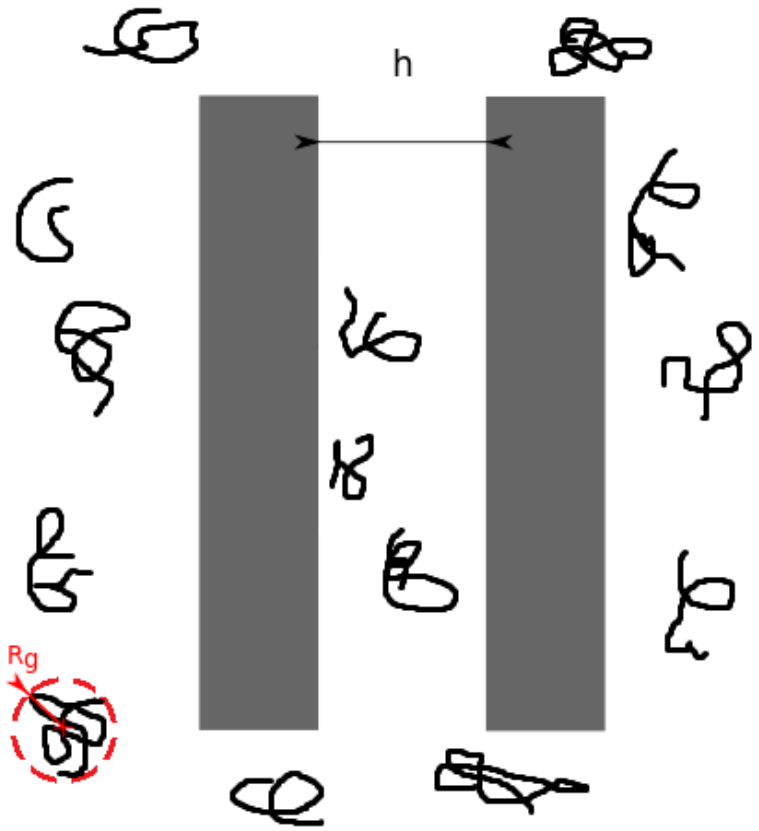

FIGURE 1.9: Schematic of depletion induced by an ideal polymer between two plates. The radius of gyration R_g is represented in red and h is the distance between the plates

$$R_g = 0.66 M_w^{0.43} \tag{1.26}$$

and in the case of dextran:
$M_w = 70000 g/mol$

Using the same methodology as for the case with two spheres, we end up with an interaction potential:

$$W(h) = -n_{bulk} k_B T (\frac{4R_g}{\sqrt{\pi}} - h + h\chi(h)) \tag{1.27}$$

$\chi(h)$ is the segment density profile of the polymer near the plates and h the distance between these plates.

For $0 \leq h \leq \frac{8R_g}{\sqrt{\pi}}$:

$$\chi(h) = \frac{8}{\pi^2} e^{\frac{-\pi^2 R_g^2}{h^2}} \tag{1.28}$$

For $h > \frac{8R_g}{\sqrt{\pi}}$:

$$\chi(h) = 1 - \frac{4R_g}{h\sqrt{\pi}} \tag{1.29}$$

To further simplify the system, one should keep in mind the work of Eisenriegler [78] who showed that the interaction potential of ideal polymers is the same as for penetrable hard spheres with a diameter σ. This leads to an interaction potential that can be written as follows:

For $h < \sigma$:

$$W(h) = -n_{bulk} k_B T (\sigma - h) \tag{1.30}$$

For $h \geq \sigma$:

$$W(h) = 0 \tag{1.31}$$

Introducing d, as the "center to center" distance between the cells and approximating the two interacting RBCs as disks (Fig. 1.10), the contact area can be calculated as following:

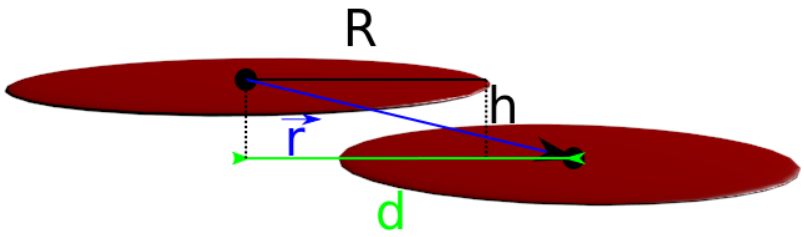

FIGURE 1.10: Schematic representation of two interacting disks with a radius R, separated by h the height and d being the center to center distance.

$$\mathcal{S} = 2R^2 \cos^{-1}\left(\frac{d}{2R} - \frac{1}{2}\sqrt{4r^2 - d^2}\right) \tag{1.32}$$

After derivation, the infinitesimal surface is:

$$\frac{d}{dd}\mathcal{S} = -\sqrt{4r^2 - d^2} \tag{1.33}$$

Plugging 1.33 into 1.30 we obtain the force as a function of the overlap distance d between the two RBCs:

$$F(d) = -n_{bulk} k_B T \frac{4R_g}{\sqrt{\pi}} \sqrt{4R^2 - d^2} \tag{1.34}$$

R_g is the radius of gyration (see Eq. 1.26), $R = 3.7\mu m$ as the radius of the two disks (average radius of a RBC), T the room temperature and d is the distance between the two disks "center to center"

Rod-like particles

The shape of the depletant has a major effect on the depletion forces. Fibrinogen is the longest protein in plasma and this model can be of interest to understand its role in aggregation of RBCs. In our work, we use rod-like particles also known as Fd-wt virus as a pure depletant. Let L be the length of the rod and D its diameter. Based on the work from Lekkerkerker et al. [79], we will approximate RBCs not as big spheres but as large plates, parallel to each other. We consider rods to be infinitely thin and thus L»D (Fig. 1.11)

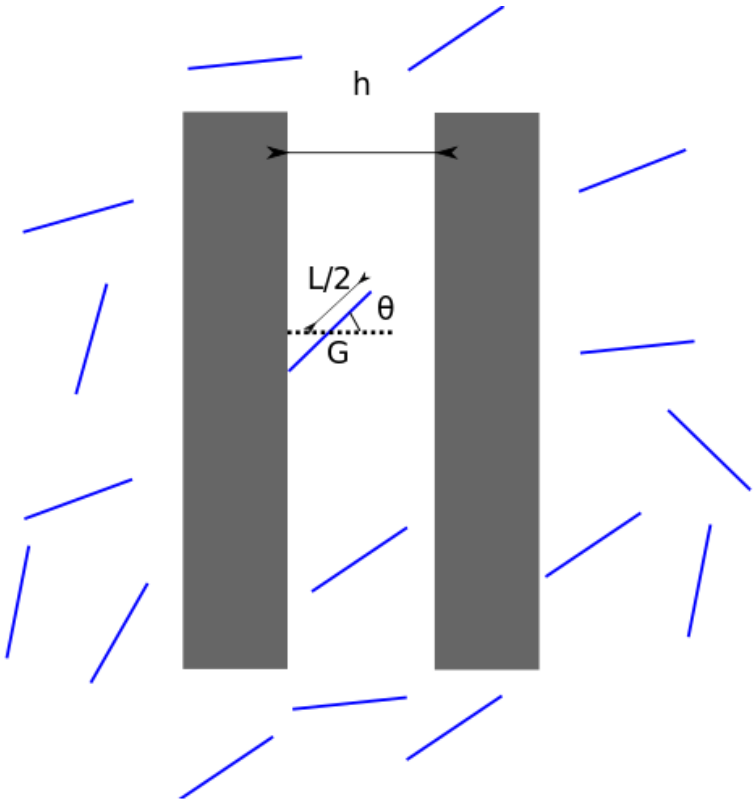

FIGURE 1.11: Scheme representing two plates separated by a distance h in presence of a rods-like depletant of length L and G being their center of mass

Here we used the force method to find the interaction energy as a function of the distance between two plates.
If a rod is in contact with the wall, the distance between its centre of mass G and this given wall is smaller than L/2 and the contact angle is:

$$\theta_x = acos(\frac{x}{L/2}) \tag{1.35}$$

x being the horizontal distance from the wall. Switching to spherical coordinates, the number density outside the plates n_o is therefore:

$$n_o = n_{bulk} \int_0^{\pi/2} sin\theta d\theta = n_{bulk} \tag{1.36}$$

n_{bulk} being the bulk number density and:

$$n_{bulk} = \frac{N_a}{M_w} c_b \tag{1.37}$$

And the osmotic pressure, at a temperature T, outside the plates P_o can be summarized as:

$$P_o = n_{bulk} k_B T \tag{1.38}$$

Inside the plates, the number of configurations is somehow limited by the opposite plate. Hence, the number density inside the plates must be split in two cases and the resulting osmotic pressure inside the plates P_i is:

-For $h \in [0, L]$:

$$P_i = n_{bulk} k_B T \int_{\theta_{h/2}}^{\pi/2} sin\theta d\theta = n_{bulk} k_B T \frac{h}{L} \tag{1.39}$$

-For $h > L$:

$$P_i = n_{bulk} k_B T \tag{1.40}$$

Finally, we get the depletion force F_{dep} which is attractive between the plates:

$$F_{dep}(h) = P_i - P_o = -nk_B T(1 - \frac{h}{L}) \tag{1.41}$$

-For $h > L$:

$$F_{dep} = 0 \tag{1.42}$$

And its associated interaction potential after integrating the depletion force:

$$W(h) = -\frac{1}{2} n_{bulk} k_B T \frac{(L-h)^2}{L} \tag{1.43}$$

and outside the plates:

$$W(h) = 0 \tag{1.44}$$

Now, plugging 1.33 into 1.43, the resulting force for two interacting RBCs with a distance center to center d is:

$$F(d) = -\frac{1}{2} n_{bulk} k_B T L \sqrt{4R^2 - d^2} \tag{1.45}$$

and in our case: $L = 880nm$, R the radius of the disks, averaged to $R = 3.7\mu m$ (radius of a RBC) and n_{bulk} the bulk number density (see Eq. 1.37). For Fd-virus, $M_w = 1.64 * 10^7 g/mol$

Later on, the depletion theory had a rising interest in the hemorheology community and the interaction between RBCs has been described inspired by this theory [80, 58]. It promotes the idea of two RBCs interacting between each other due to the difference in osmotic pressure caused by the surrounding macromolecules.

1.6 Summary

In this introductory chapter, context and motivation about blood research is brought. Blood has been described starting from its main constituent plasma to more detailed compounds such as cells that constitute it. We dove into the complex structure of a RBC which is the main biological object we studied in this thesis. Besides, we focus on a phenomenon that takes place in our body: the aggregation. The current knowledge is exposed thanks to an extended literature review. The two plausible models, namely **bridging and depletion**, to describe this phenomenon are discussed together with the issues that still need to be elucidated. A mathematical description of the bridging model and calculations starting from the basis of depletion to more complete concepts are detailed.

Chapter 2

Material and methods

Working with blood requires a particular care in order to be studied properly. Methods to handle blood cells and in particular RBCs are here detailed from its withdrawal to the sample preparation. Experimental techniques are also presented in this chapter. Starting with microfluidic devices, the fabrication of chips for the study of RBCs in flow is depicted. This method can be combined with optical tweezers, for a non invasive manipulation of cells but also for the measurements of forces involved between RBCs. Different calibration methods to measure these forces together with an extensive presentation of both experimental setups are here exposed.

Matériel et méthodes

Le travail avec le sang nécessite un soin particulier pour être bien étudié. Les méthodes de manipulation des cellules sanguines et en particulier des globules rouges sont ici détaillées depuis leur prélèvement jusqu'à la préparation de l'échantillon. Des techniques expérimentales sont également présentées dans ce chapitre. En commençant par les dispositifs microfluidiques, la fabrication de puces pour l'étude des globules rouges en écoulement est décrite. Cette méthode peut être combinée avec des pinces optiques, pour une manipulation non invasive des cellules mais aussi pour la mesure des forces impliquées entre les GRs. Différentes méthodes de calibration pour mesurer ces forces ainsi qu'une présentation détaillée des deux dispositifs expérimentaux sont ici exposés.

Materialien und Methoden

Die Arbeit mit Blut erfordert besondere Sorgfalt, um gut untersucht zu werden. Die Methoden zum Umgang mit Blutzellen und insbesondere mit Erythrozyten werden

hier von der Entnahme bis zur Probenvorbereitung detailliert beschrieben. Auch experimentelle Techniken werden in diesem Kapitel vorgestellt. Ausgehend von mikrofluidischen Geräten wird die Herstellung von Chips für die Untersuchung von RB im Fluss dargestellt. Diese Methode kann mit einer optischen Pinzette kombiniert werden, für eine nicht invasive Manipulation der Zellen, aber auch für die Messung von Kräften, die zwischen den Erythrozyten wirken. Verschiedene Kalibrierungsmethoden zur Messung dieser Kräfte zusammen mit einer ausführlichen Darstellung beider Versuchsaufbauten werden hier vorgestellt.

2.1 Blood handling

2.1.1 From finger prick to venous blood

For small volumes of blood, the finger prick method is the fastest to obtain fresh blood from a donor. We can collect up to hundreds of microliters. It is very adapted to optical tweezers experiments since only a small amount of "fresh" RBCs is needed for this purpose. The finger tip is punctured utilizing a small device (same as for diabetes patients). Before and after the procedure, hands are disinfected with 70% alcohol solution. Drawn blood can then be resuspended in various solutions.
When larger volumes are needed, blood can be drawn via venipuncture. A needle connected to a MONOVETTE ® vacutainer is inserted into the vein and blood is collected due to the pressure difference between the tube and the volunteer's vein. This method is necessary for collecting plasma, serum or other blood cells that are less present in blood such as white blood cells, for instance. Several anticoagulants are available and are already coated on tubes' inner walls. Either $K_3 - EDTA$, $Li - heparin$ or $Na_2H - citrate$ to prevent the coagulation. Very little literature can be found about the effect of the anticoagulant on physical properties of RBCs. Nevertheless, measurements performed with LORCA show that no significant effect could be reported for RBCs' deformability and aggregation [14].

2.1.2 Blood preparation

After collection, blood is centrifuged at 1800 g during 10 mins to obtain three distinct layers. The first layer containing plasma with all the proteins (albumin, fibrinogen, γ -globulins,...) is isolated and placed in aliquots. The middle layer is not of interest in this thesis and is usually discarded. Finally, the bottom layer with RBCs is

collected and resuspended in a buffer solution. RBCs are washed twice. This procedure consists of mixing RBCs with a buffer solution (PBS), centrifuging with the same G-force/time as stated above and removing the supernatant (PBS in this case).

2.1.3 Buffer solutions

RBCs are often washed or resuspended in buffer solutions. The most common one is probably phosphate buffered saline (PBS) solution but it may not be the most adapted for long term. In fact, these solutions aim to preserve the shape and physical properties of RBCs by preserving their integrity. A good buffer solution meets 3 criteria: pH, osmolality and sustaining nutrients. Despite having two of them, PBS, for instance, lacks the third one.
pH needs to be kept similar to the value in plasma $pH = 7.4$ since an acidic buffer solution can lead to less deformability [81]. Buffer solutions like HEPES are known for their pH stability. This is one of the reason of its broad use in cell culture.
Osmolality needs to be carefully controlled. Healthy RBCs keep their biconcave shape if osmolality is in the range of 290-310 mOsm. This is particularly relevant when working with fibrinogen, for example. Some proteins are usually sold with salt to avoid their degradation and in order to preserve them for longer time. This is problematic in a sense because it raises the osmolality of the buffer. Since the mass of salt in the container is usually not accurately specified, one must adjust the osmolality of the buffer solution. Three kind of solutions for RBCs can be distinguished :

- Isotonic: This corresponds to solutions in which the volume of RBCs is not changed such as plasma, for instance. In fact, no exchange of water can be observed through the membrane of the cell. The cell conserves its discocytic shape. (Fig. 2.1 (b))
- Hypertonic: There is an exchange of water from the inside of the cell to the outside. This aims to counterbalance a too high concentration of solute outside the cell. The characteristic shape of a RBC in such solution is an echynocyte (Fig. 2.1 (a))
- Hypotonic: For solutions with a too low concentration of solute, the intake of water by the cell becomes more important. We observe, in this case, mostly spherocytes (Fig. 2.1 (c)). Some cells can even "explode" releasing their content. This phenomenon is called lysis.

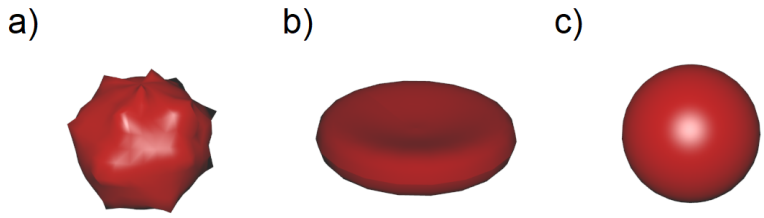

FIGURE 2.1: 3 dimensional representation of: (a) an echynocyte (crenated cell) (b) a discocyte (normal shape of a RBC) and (c) a spherocyte

For longer storage, RBCs need sustaining nutrients (usually glucose). Buffer solutions like Tyrode's buffer usually include it in the preparation. RBCs only carry oxygen and don't use to produce their energy. Adenine triphosphate (ATP), the energy carrier in RBCs, is released by glycolysis.

2.1.4 Dealing with the glass effect

The "glass effect" [82] occurs when RBCs are in contact with an artificial surface. Healthy discocytic RBC turn into echinocytes. This crenation of RBCs is less present or absent when RBCs are in their native medium. To prevent it, we prepare a 1% solution of Human Serum Albumine (HSA) in distilled water. It is known that HSA inhibits RBCs' aggregation. The surface on which RBCs lie can be passivated by using this solution as a coating. After drying out, only HSA remains on the surface.

2.1.5 Blood storage

Unless stated otherwise, all experiments were performed with fresh blood. However, due to laboratory regulations or long time measurements, it can happen that blood need to be stored and properties of RBCs may be altered [83]. For instance, we sometimes store autologous plasma since it can be used to resuspend RBCs. We follow the conventional procedure used by blood banks and freeze plasma in 2 ml aliquots under -18 °C for ulterior use [84]. Concerning RBCs, it really depends on the properties that are studied. For microfluidic measurements, deformability and rigidity of RBCs may be of interest. According to Uykulu et al. [85], RBCs could be stored up to 6 hours at room temperature without any significant change that could be measured by ekacytometer. Longer storage time tends to stiffen the RBCs. For optical tweezers measurements where (dis)aggregation is measured, this storage time can be prolonged to 12 hours if RBCs are stored at 4 °C.

2.2 Microfluidics

2.2.1 Microfluidics setup

To perform microfluidic experiments, an ELVEFLOW © microfluidic device is used. It applies a precise pressure drop and pushes a fluid through a microfluidic chip. Using a x60 oil immersion objective and a high speed camera, image sequences can be recorded (Fig. 2.2). To facilitate the experiments, the illumination, the microfluidic device together with the high speed camera can be controlled via computer.

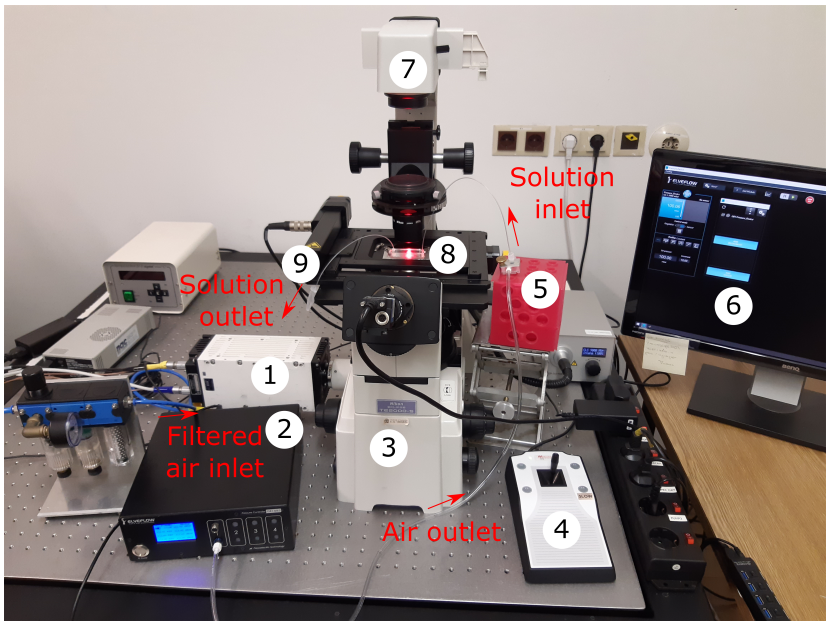

FIGURE 2.2: Setup for microfluidic experiments. 1:High speed camera, 2: Pressure controller, 3: Inverted microscope, 4: Joystick for X-Y piezostage, 5: Sample holder, 6: Software interface, 7:Red illumination, 8:Microfluidic chip, 9: Sample outlet.

2.2.2 Microfluidics chips preparation

A wafer with the desired channel design is used for the production of microfluidic chips. An elastomer, PDMS (Polydimethylsiloxane), is mixed together with a curing agent RTV-615 with a ratio of 1:10. The fluid mixture is poured into the wafer (Fig. 2.3). To prevent the presence of air inside the mixture the wafer containing the mixture is placed under vacuum by applying a negative pressure. After 30 mins, the system is brought back to the atmospheric pressure and put into the oven at 75 °C for at least one hour. The hardened PDMS chip can then be cut and removed from the wafer. The final step consists of bonding the PDMS chip onto a microscopic glass

slide. The microscopic slide is cleaned once with isopropanol and then, water before being dried out with pressured air. Finally, the microscopic slide and the PDMS chip are placed in a plasma chamber for 30 s before being bonded together.
These steps can be repeated as many times as one wants to produce chips. The final result after all these steps is shown on Fig. 2.3.

FIGURE 2.3: Photography of a wafer containing the PDMS and curing agent mixture (left) and the final microfluidic chip after bonding it to a glass slide with plasma exposure (right)

2.3 Optical tweezers

2.3.1 History and principle

Back in 15th century, Leonardo Da Vinci brought the idea of a moving sail using the energy of the Sun. Two centuries later, Johannes Kepler was the first to talk about a "radiative pressure", as he observed that comets have their tails always pointing away from the sun. During his research in Bell Laboratories, in 1970, Arthur Ashkin publishes his article [86, 87] in which he reported being able to trap micron-sized objects using the same radiation pressure. In 2018, he was rewarded with the Nobel prize for his work on optical tweezers. It's a novel method which opened many

opportunities in the field of biophysics. To cite only a few, it allowed manipulation of sperm cells [88, 89], bacterial flagella [90] or even viruses [91].

An optical trap can be obtained when a beam is tightly focused using a high numerical aperture objective. Three physical components come into play: the refraction, the radiation pressure and the electrical field. Trapped object needs to be transparent as the light must go through it. In fact, the light carries momentum which, according to the law of physics, has to be conserved. Due to the Gaussian profile of the laser beam (Fig. 2.4), the center of the beam has more power than its periphery which gives birth to a gradient force. When the light displaces out of the center the object, this one acquires momentum to counter-balance it. This is the reason, why refraction keeps the object in the middle of the beam. However, this doesn't explain why light can trap. A part of the momentum is absorbed by the object which pushes it away from the light source. The first idea was to use gravity to counter the force induced by the radiation pressure [92, 93] or two beam traps [86]. Nevertheless, these experimental setups were not very stable. Ashkin's idea to establish a stable trap was to add a strong lens just before the object, which can be easily achieved using a high numerical aperture objective. By focusing the beam directly on the object, this also creates a gradient force and pushes the object in the opposite direction (closer to the source). Forces are schematically represented on Fig. 2.4

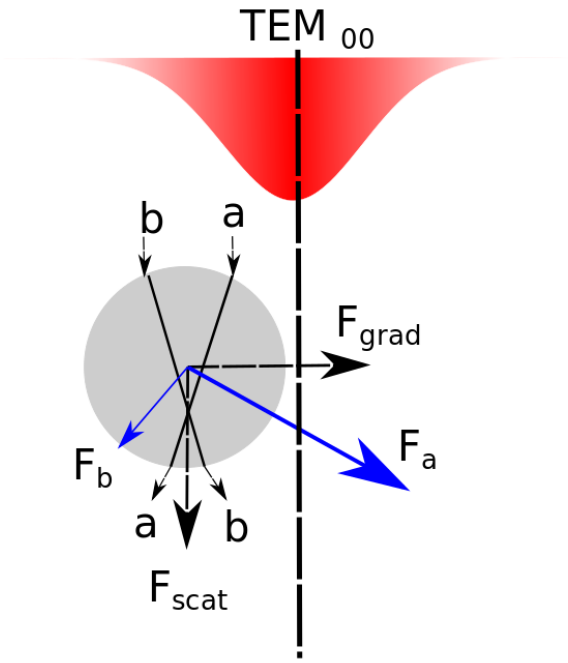

FIGURE 2.4: Scheme representing a Gaussian beam going through a bead and the related optical forces. Due to the beam geometry, more energy is emitted at the center which gives birth to a net force towards the center in opposite direction from the source.

2.3.2 Holography: The Spatial Light Modulator

One of the major component of our optical tweezers is the use of a Spatial Light Modulator (SLM). Different ways to generate and optimize optical traps exist [94, 95]. It can be performed via a single mirror that will reflect the beam and by moving the mirror the operator can control the position of this single trap. A simple way to achieve a two traps configuration is to use a polarizer. This can split the beam in two but it also allows to tweak the optical force by letting pass a certain polarization. Nevertheless, we chose to build our optical tweezers using a SLM. There exists SLM that can modulate the phase or the amplitude of a beam. In our case, we use a monochromatic laser with a wavelength of $\lambda = 1064$ nm. Its electrical field E is governed by the following equation:

$$E(r,z) = E_0 \frac{w_0}{w_z} e^{\frac{-r^2}{w^2(z)}} e^{-ikz - ik\frac{r^2}{2R(z)}} + i\zeta(z) \tag{2.1}$$

with r: the radial distance from the central axis of the beam, z: the axial distance from the beam's waist, k is the wave number and $k = \frac{2\pi n}{\lambda}$, E_0 the amplitude of the

electric field, w_0 is the waist radius and w the radius along the beam at which the amplitude falls to $\frac{1}{e}$, R the radius of curvature of the beam and finally $\zeta(z)$ the Gouy phase along the z-axis.

We have a SLM that modulates the phase of the beam, i.e. it will change the phase term in the exponent. The SLM can be seen as a grid constituted of liquid crystals. The optical properties of each crystal can be modified by applying a voltage. The whole idea behind holographic optical tweezers is to create a phase pattern on the SLM (Fig. 2.5 (a) and (b)) so that, when the laser beam hits the SLM traps can be generated in the focal plane of the high numerical aperture objective (also used for imaging purpose as it can be seen on Fig. 2.5 (c) and (d)). In terms of complex amplitudes, the amplitude in the focal plane is simply the Fourier transform of the amplitude of the beam. However, in practice, the intensity distribution in the focal plane is usually not the one expected. One easy fix is to adjust the intensity distribution in the focal plane (with the same phase) but this cannot be done without changing the intensity distribution from the beam. Such tuning can be achieved by an algorithm going through an iterative process until it converges to the desired intensity and phase in the focal plane.

To do so, we found the Gerchberg-Saxton algorithm [96] to be the most reliable in our case as it allows a good compromise between the time calculation of the phase and the spatial accuracy.

We note that in order to get valid measurements, generated traps must be reasonably far away from the undiffracted laser beam situated in the middle of the SLM grid.

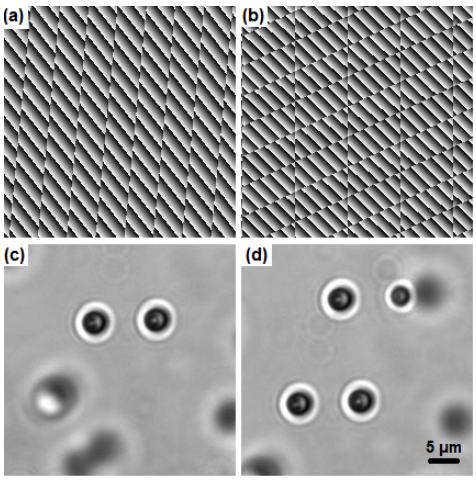

FIGURE 2.5: Phase holograms generated for 2 (a) and 4 (b) optical traps and their associated microscopic images of trapped beads with a diameter of $5\mu m$ respectively (c) and (d)

2.3.3 Mathematical formalism

Depending on the size of the object, we can distinguish two regimes for optical trapping. For objects with size smaller than the wavelength of the laser such as $D < \lambda$, the system is in the Rayleigh regime. For $D > \lambda$, we are in the Mie regime.

Since the trapped object has to be dielectric, it can be seen as a dipole. The electric component of the Lorentz force is in the form of:

$$\vec{F_L} = q\vec{E} \tag{2.2}$$

Where q is the electric charge of the dipole and E the electric field.
In the Rayleigh regime, the trapped particle can be approximated as a point. The force induced by the laser onto the dipole is proportional to the gradient of the electric field and therefore, to the intensity of the laser. This "gradient" force F_g can be written as:

$$F_g = \frac{2\pi r^3 n_1}{c}\left(\frac{m^2-1}{m^2+2}\right)\nabla I \tag{2.3}$$

r is the radius of the trapped object, n_1 is the refractive index of the medium, n_p is the refractive index of the particle and m the effective index such as: $m = \frac{n_p}{n_1}$. I is the intensity of the laser and c the speed of light.
The scattering force is directly proportional to the intensity of the laser and is:

$$F_s = \frac{128\pi^5 r^6 n_1}{3\lambda^4 c}\left(\frac{m^2-1}{m^2+2}\right) I \tag{2.4}$$

For the Mie regime, ray optics can help to understand how optical trapping takes place. Ashkin demonstrated that in this case the gradient force F_g and the scattering force F_s are:

$$F_g = \frac{n_1 P}{c}\left(R\sin 2\theta - T^2\frac{\sin(2\theta-2\phi)+R\sin 2\theta}{1+R^2+2R\sin 2\phi}\right) \tag{2.5}$$

$$F_s = \frac{n_1 P}{c}\left(1+R\cos 2\theta - T^2\frac{\cos(2\theta-2\phi)+R\cos 2\theta}{1+R^2+2R\cos 2\phi}\right) \tag{2.6}$$

with P being the power of the ray, R and T are respectively the Fresnel coefficients in reflection and transmission. θ refers to the angle of incidence and ϕ the angle of refraction of a given ray (Fig. 2.6). Interestingly enough, the front coefficient corresponds to the momentum transferred by a ray in a second.

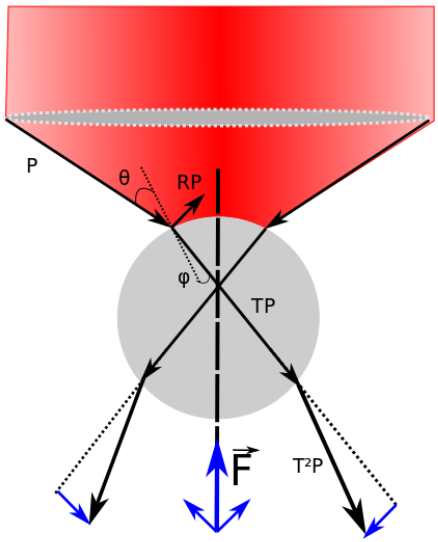

FIGURE 2.6: Scheme representing a gaussian beam going through the lens of a high numerical aperture objective. Trapping is explained using ray optics and Fresnel coefficients (T: transmission, R: reflection and P:initial power). In this configuration the net force points towards the source and trapping takes place.

2.3.4 Experimental setup

Our current experimental setup (Fig. 2.7) was designed by Achim Jung and Christian Ruloff. Their work represents a starting point for the maintenance and to the

further development of holographic optical tweezers. A continuous wave laser with a wavelength of $\lambda = 1064$ nm was carefully chosen to prevent the absorption of light by RBCs. The beam goes through a beam expander constituted of two lenses before being collimated onto the spatial light modulator (SLM). Our SLM works in phase-mode

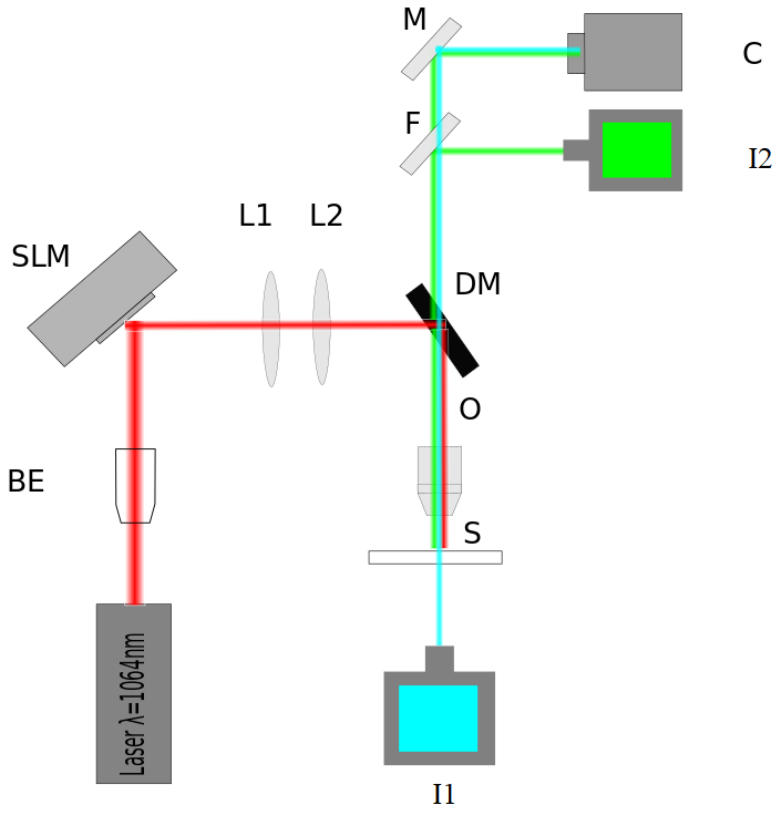

FIGURE 2.7: Simplified scheme of the holographic optical tweezers. BE: beam expander, SLM: Spatial Light Modulator, L1 and L2: lenses, DM: Dichroic mirror, C: Camera, O: High numerical aperture x60 objective and S: Sample. I1: main illumination, I2: mercury lamp, F: fluorescent filter and M: mirror

2.3.5 Calibration

Stokes calibration

Several calibrations procedures can be used. The most practical and wide spread one is probably the Stoke's calibration. It is based on Stokes' law which gives the force exerted on a small object dragged in a viscous medium. The force can be

described as follows:

$$F_{drag} = 6\pi\eta r v \tag{2.7}$$

where r is the radius of the dragged spherical object, η the dynamic viscosity of the medium and v is the dragging velocity of the object in the medium.

However, we manipulate RBCs which are known to be particularly soft and non spherical. For this reason, we adapt the Stokes' law by adding two factors for the geometry of the object which differs from a bead. We also need to take into account the proximity of the cover glass while moving the object with a piezo-stage [97].

These factors can be written as:

$$\beta = \frac{1}{1 - \frac{9}{16}(\frac{a}{h}) + \frac{1}{8}(\frac{a}{h})^3 - \frac{45}{256}(\frac{a}{h})^4 - \frac{1}{16}(\frac{a}{h})^5} \tag{2.8}$$

$$K = \frac{\frac{4}{3}(\alpha^2 - 1)}{\frac{2\alpha^2-1}{\sqrt{\alpha^2-1}} ln(\alpha + \sqrt{(\alpha^2 - 1)}) - \alpha} \tag{2.9}$$

where a: radius of the dragged sphere, h: distance from the microscopic slide and α is the ratio between the long and short axis of an ellipse.

The corrected drag force then becomes:

$$F_{trap} = 6K\beta\pi\eta r v \tag{2.10}$$

Thermal noise for stiffness measurements

Based on the equipartition theorem, one can calculate the stiffness of an optical trap. For a system which is at thermal equilibrium, its energies involved are equally distributed. This method presents a considerable advantage since it's independent of the size or shape of the bead but also it gets rid of any viscosity measurements. However, it's very sensitive to environment noise. An object in an optical trap can be approximated by a harmonic potential and counter-balanced by its thermal fluctuations.

$$\frac{1}{2}K_{OT} < x^2 >= \frac{1}{2}k_B T \tag{2.11}$$

Thus, the stiffness of an optical trap is given by:

$$K_{OT} = \frac{k_B T}{< x^2 >} \tag{2.12}$$

With x the position of the centre of a bead and T the absolute temperature. Fig. 2.8 shows an exemplary distribution of the bead centroid's position over time.

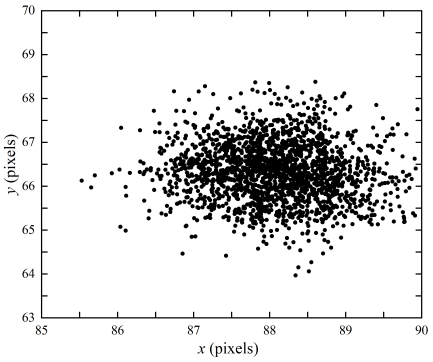

(A) Position of the bead centroid for a power of 38 mW

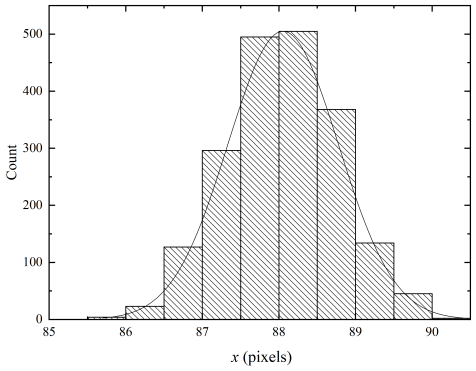

(B) Spatial distribution along the X axis for 38 mW

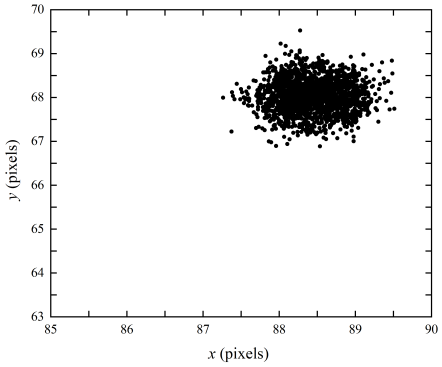

(C) Position of the bead centroid for a power of 161 mW

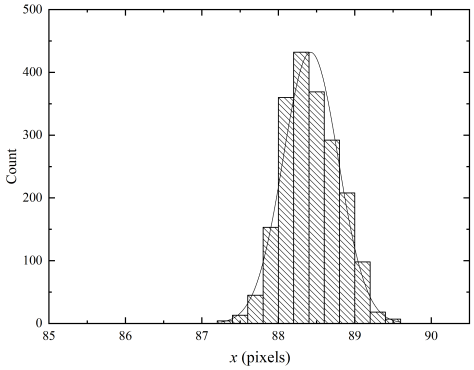

(D) Spatial distribution along the X axis for 161 mW

FIGURE 2.8: Stiffness measurements using thermal noise and based on the position of bead centroid

Using equation, Eq. 2.12 one can plot the stiffness of a single trap in the measurement configuration (2 traps) as a function of the laser output power (Fig. 2.9). The relation between the two quantities follows a linear trend. Even though higher laser intensities can be reached, they were discarded since they are never used in our studies for RBCs. This is mainly to avoid heating effects or damaging of the RBC's membrane (hemolysis, pear-shape deformation, ...), Another reason, more practical, is concerning the limit that our SLM can undergo.

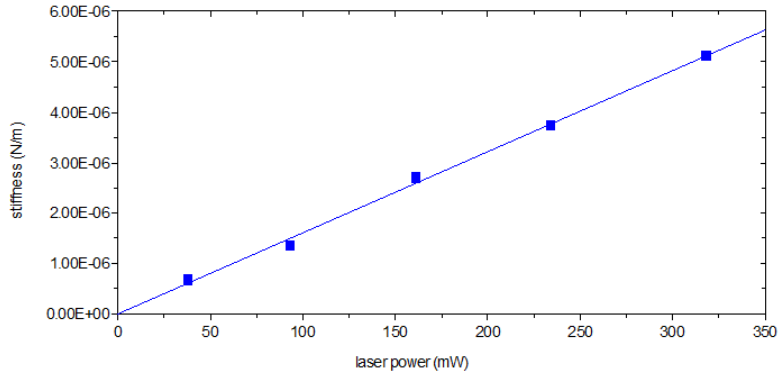

FIGURE 2.9: Stiffness calibration using the thermal noise method for a generated trap as a function of the laser power

Bead-Cell calibration

Calibration of optical tweezers using beads has been quite extensively studied [98, 99, 100]. Nevertheless, in terms of forces applied on RBCs it is subject to discussion. In fact, trapping RBCs differs from trapping a quasi-perfect spherical object such as beads. In the case of RBCs, this is the haemoglobin which is trapped and thus, the forces applied on the cell should be reconsidered. To do so, we attached a $5\,\mu m$ in diameter, glass bead to a cell for several trapping power as depicted in Fig. 2.10.

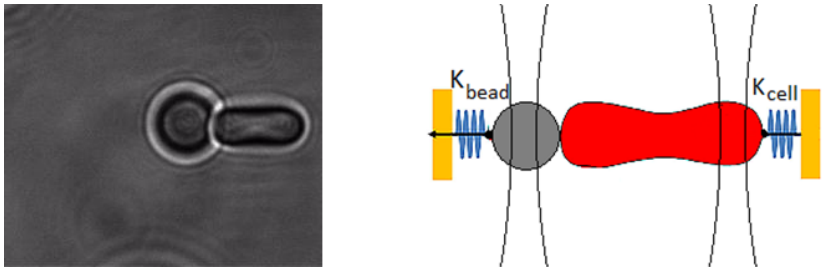

FIGURE 2.10: (a) Experimental and (b) scheme of the force calibration using a $5\,\mu m$ bead and a RBC lifted at $15\,\mu m$ from the cover glass.

Thanks to the methods exposed above, the stiffness and the force applied on a bead are well determined. We approximated the cell as a solid body, which is reasonable for low trapping forces. We observed that for long trapping span time and rather high powers P (P>5 mins and P>150 mW), RBCs may elongate.

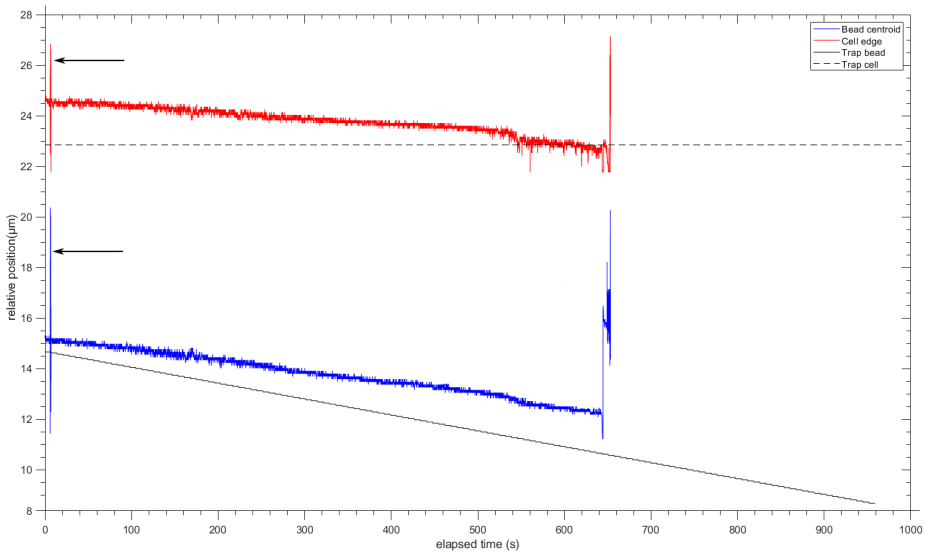

FIGURE 2.11: Output graphs for bead-cell calibration with laser power of 38 mW. The dashed (cell) and continuous black lines show the position of the trap during the measurement procedure. The red curve shows the position of the edge of the cell and the blue curve the centre of the bead over time. Arrows depict the synchronization signals

Prior to the measurements, we inspected that the position of the two traps (one for the bead, another one for the edge of the cell) generated by the computer have a well defined distance in between them. The camera started recording at 30 frames per second and was synchronized with the first step. Two arrows on Fig. 2.11 shows the synchronization signal. The trap close to the edge of the cell doesn't move. Hence, the dash line showing always the same position. The trap holding the bead moves relatively to the trap holding the cell with spatially and temporally regular steps. The chosen steps were: $d_{steps} = 50$ nm and $t_{steps} = 7$ s. We found this one to be reasonable, as it allows us to have a sub-pixel resolution and it lets the system enough time to get back to equilibrium. Fig. 2.11 shows an exemplary output graph. In the equilibrium, we have the following equation:

$$-k_{cell}\Delta x_{cell} = -k_{bead}\Delta x_{bead} \tag{2.13}$$

where Δx_{cell} and Δx_{bead} is the difference in position along the X axis between 2 consecutive frames of the position of the edge and the position of the bead, respectively. k_{bead} is the spring constant of the trap applied on the bead determined as mentioned in section 2.3.5. Finally, k_{cell} is the spring constant related to the force applied on the

RBC. For our experiments and over a range of power (below 350 mW) we found the relation between to be:

$$k_{cell} = \frac{\Delta x_{bead}}{\Delta x_{cell}} k_{bead} \tag{2.14}$$

2.3.6 Measurement procedure

In order to measure forces between two RBCs and investigate the interaction mechanisms, we established two protocols. One for the aggregation and another one for the disaggregation.

Aggregation

Two RBCs are selected using 4 generated optical traps. Each cell has one trap at its extremity (2 traps per cell). The distance between two "extremal" traps is $6\mu m$ and the distance separating the top from the bottom traps is $8\,\mu m$ (a). The bottom RBC remains static while the top one is brought into contact (b). The overlap distance between the cells is determined by our program. The two middle traps are removed (c) once cells find an equilibrium. We, then, step-wisely decrease the power of the laser which means, the force applied on the cell also drops (d). A script is run to make sure that time-force steps are constant. In most of the measurements and unless specified otherwise, we use steps of $-0.5\,pN$ every $5\,s$. This allows the system to equilibrate. At a certain time, RBCs spontaneously aggregate as the force to prevent them from aggregating is not high enough (Fig. 2.12). This is the force that we denote as the aggregation force F_A.

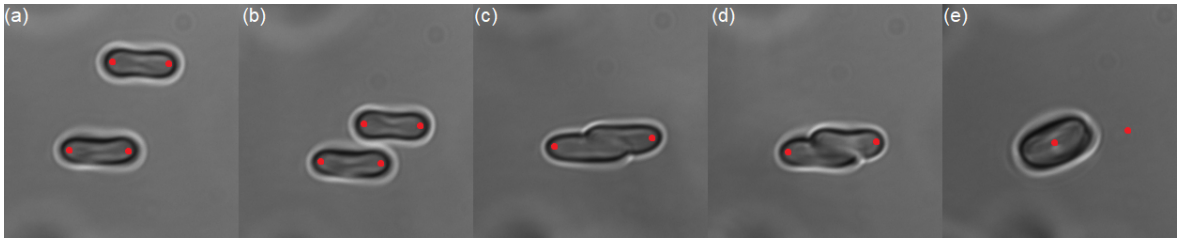

FIGURE 2.12: Time-lapse showing the force measurement procedure for the aggregation between two selected red blood cells. Red dots represent the position of the optical traps

Disaggregation

To measure disaggregation, we start from the same configuration as for the aggregation measurements. One trap is placed at each extremity of the RBC (a), cells are

brought together (b) and middle traps are removed (c) until cells are at equilibrium. To know the disaggregation force F_D, the power of the laser is fixed and thus, also the force. We, then start pulling with a constant velocity step-wisely (d). Two scenarios are then possible. Either the cells separate (e) or they do not. In most of the solutions (dextran, plasma, serum, ...), once cells snap back, they cannot be separated anymore and new cells must be taken for measurements (Fig. 2.13). This is the reason why, we need to scan several forces to have a good estimation of the disaggregation force F_D. We arbitrarily consider F_D to be the force at which more than 70% of the pairs can be separated (unless stated otherwise) not to have "probabilistic" representation of the force.

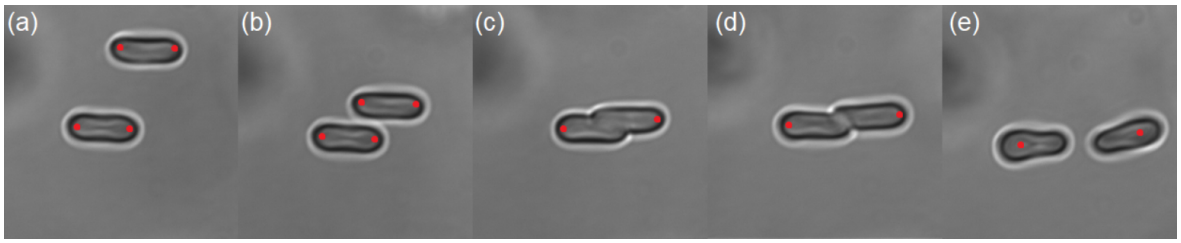

FIGURE 2.13: Time-lapse showing the force measurement procedure for the disaggregation between two selected red blood cells. Red dots represent the position of the optical traps

2.3.7 Effect of laser traps on haemoglobin

One must keep in mind that RBCs are biological objects and thus, more sensitive to the radiation pressure than inert objects. During our measurements, we always make sure to optimize the time of measurements to avoid damaging RBCs. Moreover, our laser is in the infrared range ($\lambda = 1064$ nm) and aims to limit the absorption of light by the hemoglobin enclosed in RBCs membrane. Curves B and C (in Fig. 2.14) are representative of the most prominent hemoglobin present in human RBCs. Carboxyhemoglobin (A) and methemoglobin (D) can be neglected as they constitute less than 2% of the total hemoglobin present in RBCs. The former can reach higher levels (up to 9%) for a smoker as it is synthesized when carbon monoxide is inhaled, the latter mostly comes from certain food or medication.

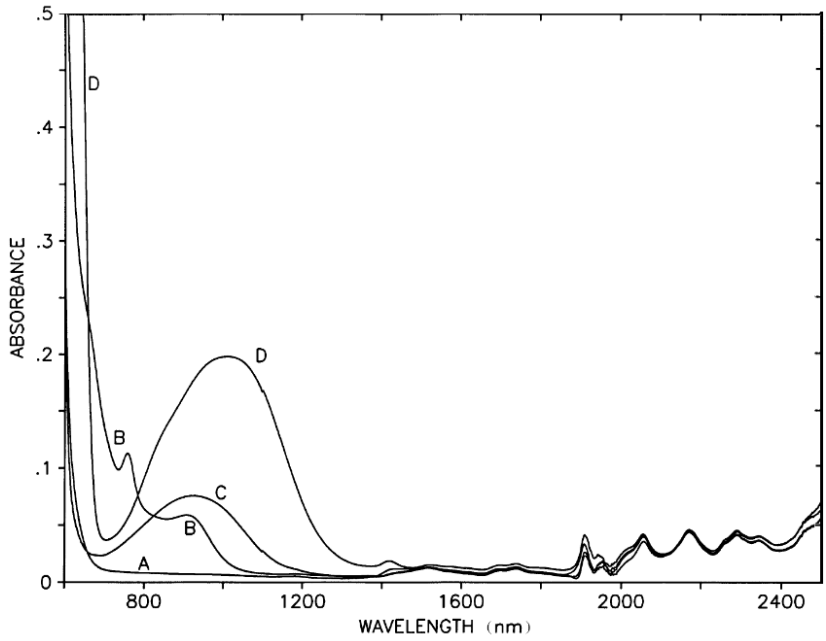

FIGURE 2.14: Absorption of light by A: carboxyhemoglobin, B: deoxyhemoglobin (Hb) C:oxyhemoglobin (HbO_2) and D: methemoglobin for different wavelength obtained by spectrophotometry from [101]

Nevertheless, we performed experiments with the undiffracted trap which is the most powerful we can get to see the deformation of RBCs under high power and better prevent the possible alteration of RBCs during measurements (Fig. 2.15).

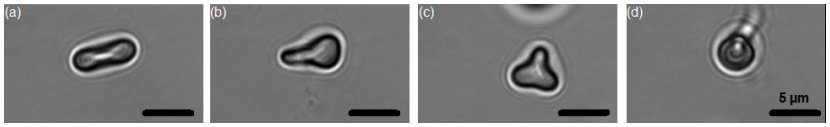

FIGURE 2.15: Single RBC trapped in autologous plasma with the undiffracted laser trap. Possible shapes than can be observed from low (<300mW) to high (up to 500 mW) power: (a) biconcave, (b) "pear" shape, (c)trilobe and (d) hemolysing RBC

All (dis)aggregation measurements rarely require laser powers higher than 300 mW. However, trapping time plays a role. We observed that for measurements involving the undiffracted trap (adsorption experiments) some changes in shape may occur for trapping timespans of the order of the minute. Most of the time, RBCs take a so called "pear" shape as depicted in Fig. 2.15 (b). The trilobe shape as seen in Fig. 2.15 (c) is more rare. After a too long exposition to the laser, the cell hemolyses and releases its hemoglobin (Fig. 2.15 (d)).

2.4 Image analysis

In this thesis, various algorithm are used for background subtraction or object detection. It often relies on the segmentation of images, i.e. extracting regions of images corresponding to object or areas of interest. This is particularly useful to track particles but also to avoid manual analysis which can be repetitive and time consuming. There exists multiple advanced segmentation methods such as: thresholding [102, 103], region growing [104] or even "Merge and split" [105, 106]. One of the basic method used in this work is based on the threshold of the image using Otsu's method [107]. Fig. 2.16 shows a good example of Otsu's method. Most of the experimental images are so-called black and white images but in fact each pixel corresponds to a value between 0 and $2^8 - 1$ or even $2^{16} - 1$ for more sensitive cameras. Dark areas have low values and bright areas high values. Segmentation based on Otsu's method regroups pixels with a value higher or lower than a selected threshold.

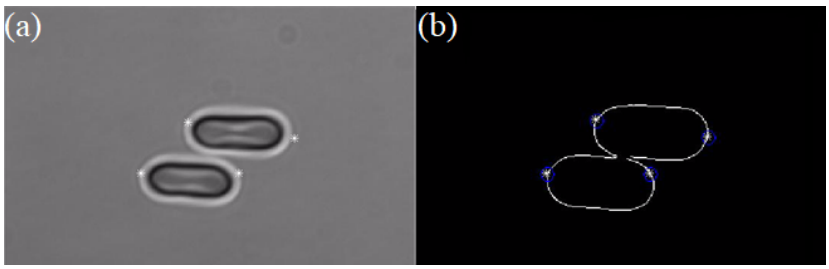

FIGURE 2.16: (a) Micro-photography of two trapped red blood cells and (b) its associated segmentation using Otsu's method

2.5 Summary

This chapter presents the physical methods used to study the properties of RBCs. Possible protocols to draw blood together with proper handling are also described. Two experimental techniques are exposed: optical tweezers and microfluidics. The former dedicated to the study of aggregation at a single cell level and the latter to observe the properties of RBCs in flow. After illustrating both experimental setups, the protocol for measuring (dis)aggregation of RBCs by OT has been specified together with the procedure for the calibration of pN-forces. Finally, the procedure for manufacturing microfluidic chips but also the way experiments were carried out are exhibited.

Chapter 3

Adsorption of macromolecules revisited

To elucidate whether bridging or depletion can better explain the aggregation of RBC, one needs to verify whether adsorption occurs onto the RBC's membrane. A more extensive study based on this work, including this chapter, has been published [108]. The depletion model suggests that the contact area between two aggregated RBCs is depleted of any proteins. Now considering the bridging hypothesis, one can expect that binding sites exist on the surface of RBCs on which proteins can be attached. Even though adsorption of macromolecules onto RBCs has already been observed thanks to various methods such as: electron microscopy [109], radiolabelling [62, 110], fluorescent labelling [111] or zeta-potential measurement [110], it was subject to potential artefacts such as the trapped fluid[28]. The method proposed here offers a versatile way to detect the adsorption of macromolecules (here dextran) onto RBCs by combining optical tweezers with a microfluidic platform. This can be done by incubating RBCs in a solution of macromolecules and by quickly changing the medium thanks to an optical trap dragging the cell against the flow. An immediate adsorption of 10^4 molecules per cell was quantified and during the incubation of RBCs with dextran, a gradual tenfold increase of adsorption was found.

3.1 Single cell level quantification of dextran on RBC

The experimental setup used for quantifying the dextran adsorption onto a single RBC was similar to the one used in a previous work [112]. The initial design of the experiment was imagined by Kisung Lee and Evgeny Shirshin. My experimental work is the continuation of Nataliya Rovnyagina's (from Lomonosov Moscow State University) experiments and helped to make the technique more reliable. A major part of this chapter has already been published [108]. It is based on the inverted microscope (TE 2000, Nikon, Japan), and the schematic layout of the setup is the

same as described in the materials section 2.3.4 of this thesis. Optical traps were formed using a laser beam from single-mode Nd:YAG laser (1064 nm, 1.5 W, Ventus 1064, Laser Quantum, UK) reflected by the parallel aligned nematic liquid crystal spatial light modulator (PAL-SLM, PPM X8267-15, Hamamatsu Photonics, Japan) and focused with a large numerical aperture oil immersion objective (N.A. 1.40, 60x, Nikon, Japan). We used laser power up to 40 mW at the focal point.

At the given wavelength and power, the heating of the sample can be considered negligible [18]. The positions of the traps were controlled independently in XYZ-plane within the focal plane of the objective using PAL-SLM. Visual control (in the reflection mode) of the trapped objects and detection of fluorescence intensity of the sample was performed in a transmission configuration using the CMOS camera (ORCA Flash 4.0 V3, Hamamatsu, Japan). When measuring fluorescence signal, the exposure time was set to 33 ms, and 4×4 binning of the images was used. The fluorescence excitation and registration was performed using a mercury lamp (HB-10103AF, Nikon, Japan) and FITC dichroic cube (fluorescein isothiocyanate-filter, Nikon, Japan) with a 480/30 nm excitation and 535/45 nm emission bands, correspondingly. Two values of excitation intensity were used: $I_0 \approx 5$ mW, when no filter was used, and $I_0/24$, when the ND filter was installed. When measuring the fluorescence signal from the dextran molecules adsorbed on RBCs, excitation intensity was set to I_0, if not mentioned otherwise. In the case of calibration measurements with fluorescence beads excitation intensity was set to $I_0/24$. Microfluidic flow control system (MK-1, ELVEFLOW©, France) was used to pump the samples through the microfluidic device.

The sample preparation protocol was as follows: (1) fluorescent dextran solution (20 mg/ml, FITC-conjugated dextran 70 kDa, Sigma, catalog no. 46945) was prepared in phosphate buffered saline (PBS, pH 7.4, 290 mOsm, INVITROGEN); (2) blood was taken by finger prick method (see 2.1.1) and a small amount was added to the dextran solution to achieve the final concentration of RBCs $\sim 0.05\%$; (3) the suspension was incubated at 22°C for a certain period of time and used for the measurements. For the experiments with pre-incubation, the cells were kept in PBS for 120 minutes, and then re-suspended in the fluorescent dextran solution followed by additional incubation for a given period of time. The experimental cuvette consisted of a microchannel S2 (Fig. 3.1 (a)) connected to a chamber or "pool" S1 (Fig. 3.1 (b)). The chamber was much larger ($3x2x0.5cm$) than the microchannel ($100x40x30\mu m$), which was connected to a micro-pump and used to maintain two different solutions. The microchannel chip was made based on PDMS (Polydimethylsiloxane), and attached to the borosilicate cover glass. The larger chamber was also covered

with a cover glass to avoid evaporation. Gentle flushing of a solution from the microchannel towards the chamber allowed for maintaining two different solutions. Due to the significant difference in the volumes, we could neglect the changes in concentration of the solution in the chamber.

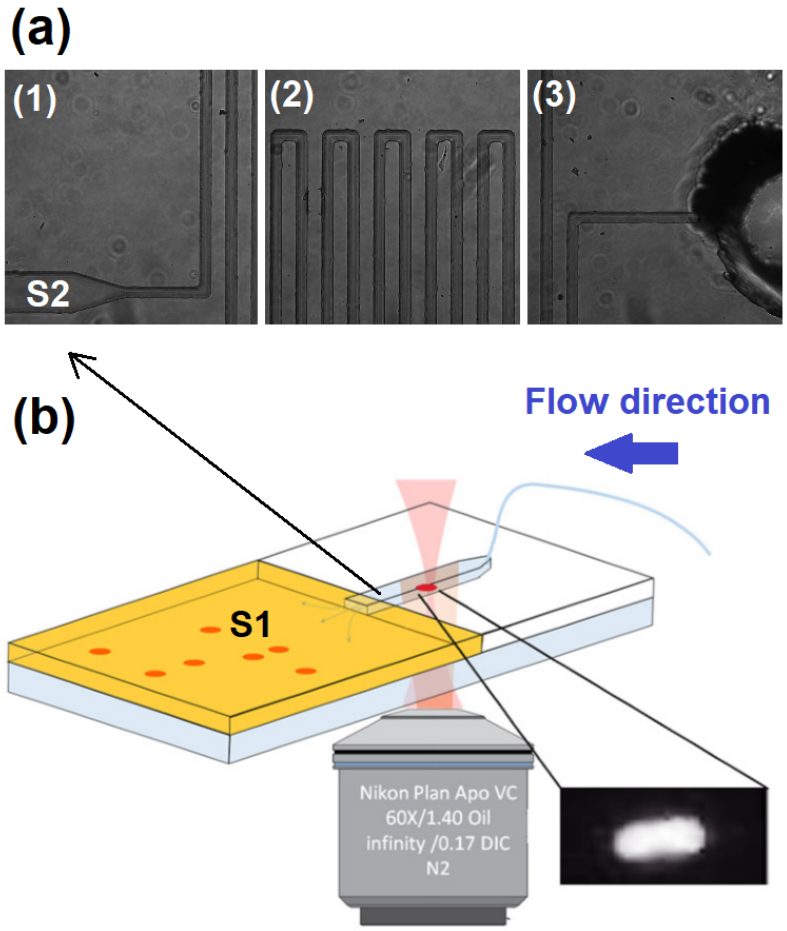

FIGURE 3.1: (a) Microfluidic chip used for investigating the adsorption of macromolecules onto RBCs.(1): Area of observation situated at about 500 μm from the "pool" (S1), (2) resistance-channel to decrease the flow velocity and (3) inlet where the buffer solution is injected. (b) Sketch representing a single RBC dragged from a macromolecule solution (in the "pool" S1) to a buffer solution "S2"

The microchannel (S2) (Fig. 3.1 (a)) was initially filled up with PBS solution, afterwards 200 µL of RBCs suspension in fluorescent dextran solution was put into the chamber (S1). The diffusion was prevented by continuously flushing S2 towards S1 at flow velocity $v_{flush} = 20$ µm /s. Test measurements have shown that at the given v_{flush} the diffusion does not take place for at least 30 minutes and the fluorescent

signal in S2 remains almost at the level of noise. In order to measure the adsorption of dextran, we trapped a single RBC with the laser tweezer, and lifted it up by 15 µm relative to the surface, and quickly transferred it from the larger chamber into the microchannel (see Fig. 3.1 (b)). Then, the fluorescence signal was recorded as shown in Fig. 3.1 (b).

To ensure that the observed RBC's fluorescence is due to the adsorption of dextran, but not due to the FITC detachment from dextran macromolecule and its adsorption on RBCs, we performed an additional test using 3 kDa filtration and size-exclusion chromatography, and confirmed that there is no FITC desorption from dextran, at least on the time scale of a typical experiment. FITC-conjugated dextran 70 kDa (Sigma, catalog no. 46945) was used in the adsorption experiments. Prior to the measurements, we verified the absence of free FITC in dextran solution and the absence of FITC desorption from dextran with time. For this, 3 kDa centrifugal filter (Amicon Ultra, Sigma) was used. The solution of fluorescently labeled 70 kDa dextran ($20 mg/ml$ in PBS) was filtered through a 3 kDa membrane, and fluorescence of the solution after filtration was measured. It was observed that only the part of solution, which did not pass through the membrane, exhibited fluorescence, thus confirming the absence of free or desorbed FITC in the system.

For the calibration measurements $2\,\mu m$ fluorescent red carboxylate-modified polystyrene latex beads (Sigma, catalog no. L3030) were used. To measure the z-profile of the fluorescence detection volume, the bead was moved stepwise in the vertical plane using the PAL-SLM without moving the objective, i.e. the parameters of excitation and detection were kept constant. Positioning of the trap to the center of the excitation beam was performed using the coordinates of the point with maximum fluorescence intensity obtained in the experiments with dextran solution. The error was taken as standard deviation calculated from three independent measurements. Fluorescence intensity was calculated as the average over the 25% of points with the highest intensity.

3.1.1 Time course of dextran adsorption onto RBC

Figure 3.2 demonstrates the time course of normalized integral fluorescence intensity for cells moved from the pool (S1) to the channel with PBS (S2). As RBCs are essentially non-fluorescent under the excitation wavelength used (550 nm), the detected fluorescence signal from the cell area was indicative of dextran adsorption. After moving an individual RBC from the solution with fluorescent dextran to PBS, we could observe a significant fluorescence signal (see Fig. 3.2, Fig. 3.3 and Fig. 3.4).

As in the channel with PBS, desorption of dextran and photobleaching were observed, which occurred on the time scale of a minute (see Fig. 3.3 and Fig. 3.4); the fluorescence intensity values in Fig. 3.2 were taken as the maximum initial values. The excitation intensity in Fig. 3.3 is 24 times higher compared to Fig. 3.4, while the corresponding decay times are 25 and 100 s. Considering the fact that the rate of photobleaching $k_{bleaching}$ is determined by the excitation intensity I (in the case of a single fluorophore $k_{bleaching} \approx I$), one can conclude that the decay of fluorescence intensity in Fig. 3.4 is mainly due to dextran desorption from the cell. Hence, the desorption rate was estimated as $\sim 0.01\, s^{-1}$.

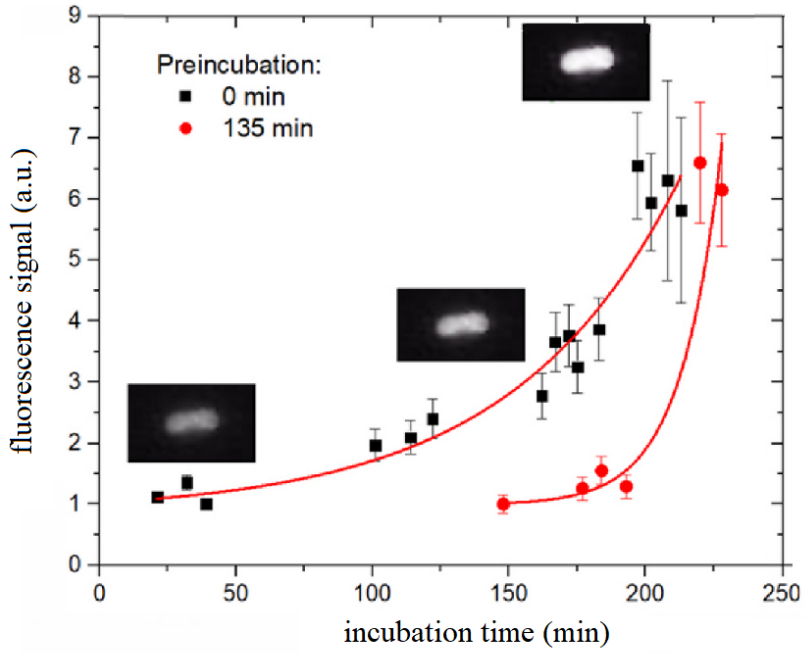

FIGURE 3.2: The dependence of maximum fluorescence intensity on incubation time: black and red dots correspond to 0 and 135 minutes of RBC preincubation in PBS respectively. The microphotographs in the insets illustrate the changes in the fluorescence intensity detected in the channel with PBS. Here, the fluorescence intensity was normalized to the value obtained in the first point. Intensity of excitation was kept the same and was roughly estimated as 5 mW at the sample. The error bars correspond to the averaging over three independent microchannels used in the experiment.

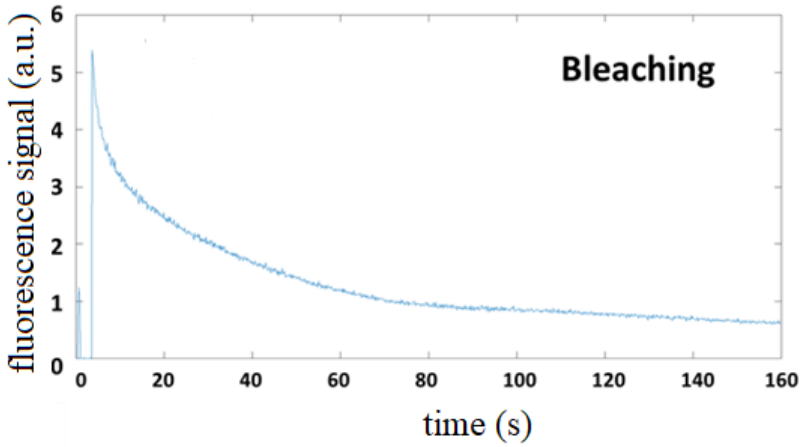

FIGURE 3.3: Fluorescent signal corresponding to bleaching

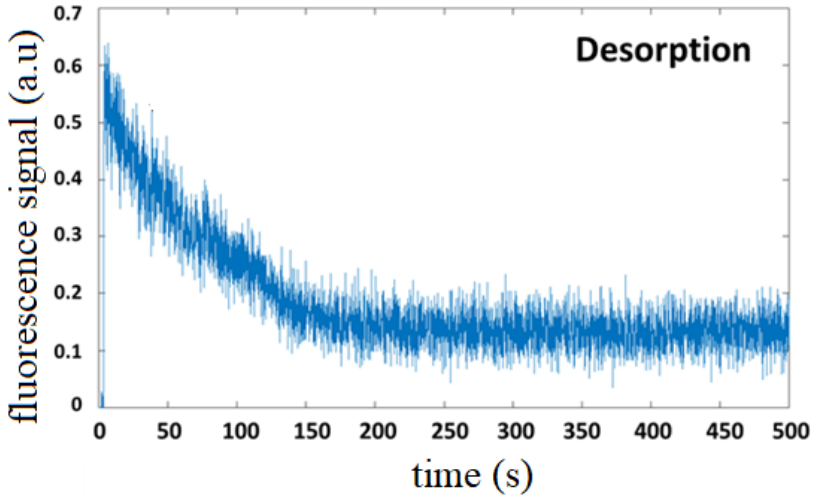

FIGURE 3.4: Fluorescent signal corresponding to the actual desorption of dextran macromolecules

The kinetics of dextran adsorption was followed by measuring the incubation time dependence of fluorescence signal. For this purpose, RBCs were sequentially moved to the channel with PBS, and the total times of cells incubation correspond to the values in the X-axis in Fig. 3.2. As a result, we observed that dextran adsorption increases gradually as a function of time (Fig. 3.2). To investigate the influence of RBCs pretreatment, adsorption kinetics were measured after 2 and 4 hours of RBCs preincubation in PBS. After preincubation, the cells were resuspended in the fluorescent dextran solution in the microfluidic chip, and the time course of fluorescence intensity was studied. In this case, after preincubation for 2 hours the initial signal was close to that in the absence of preincubation, but increased more rapidly with

time. Longer preincubation (4 hours) also did not result in the immediate enhancement of signal.

For the next step, we aimed at a quantitative estimation of the number of adsorbed molecules per cell. For this, the measurement of the fluorescence detection volume was performed with microbeads.

3.1.2 Quantification of the number of adsorbed molecules

First, to obtain the calibration curve, the microchannel was filled with the solution of dextran at different concentrations and the fluorescence signal was recorded (Fig. 3.5). To obtain the calibration curve, we used the following protocol: (1) Empty channel was filled with the solution of fluorescent dextran of different concentration; (2) Fluorescence signal of the sample was measured, and the initial (i.e. maximum) value was used for the calibration curve. The signal was averaged over the central area of the image with the highest intensity, and this area was selected in a similar manner for all concentrations; (3) For lower concentrations, exposure was increased, and the detected fluorescence signal was divided by the exposure enhancement (i.e. the intensities were normalized to the exposure); (4) After that, the dependence of fluorescence intensity on fluorophore concentration was plotted (see Fig. 3.5).

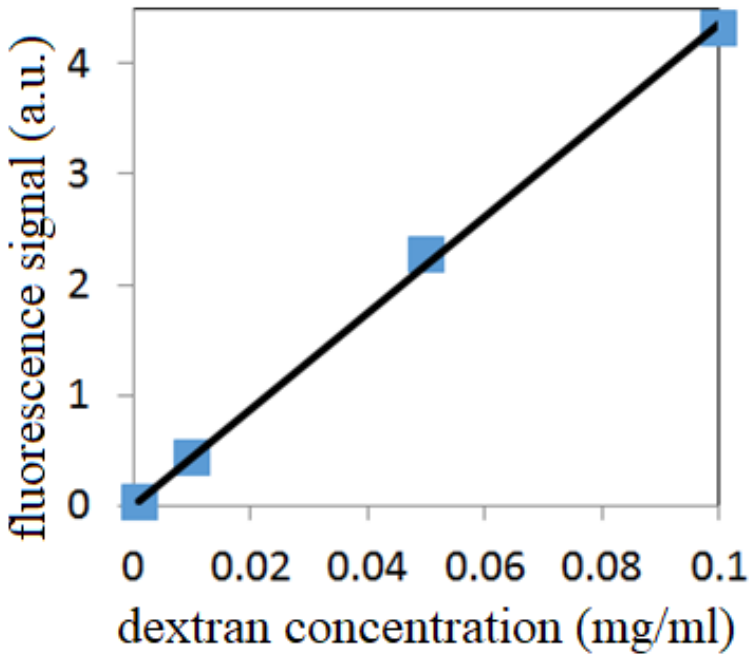

FIGURE 3.5: Dependence of the dextran concentration on the recorded fluorescent signal

To properly calculate the number of molecules, which contributed to the overall fluorescence signal, the geometry of the detection volume was assessed. For this purpose, the z-dependence of fluorescence intensity (i.e. the depth of field) was determined using 2 µm fluorescent beads. The bead was trapped and moved in the Z-direction in a stepwise manner relative to the focal plane of the objective. The measurements were performed in the microchannel filled with PBS. The position of the trap was changed by adjusting the PAL-SLM mask parameters while keeping the objective position constant, that allowed moving the trap relative to the excitation beam without changing the geometry of the latter in the sample (Fig. 3.6).

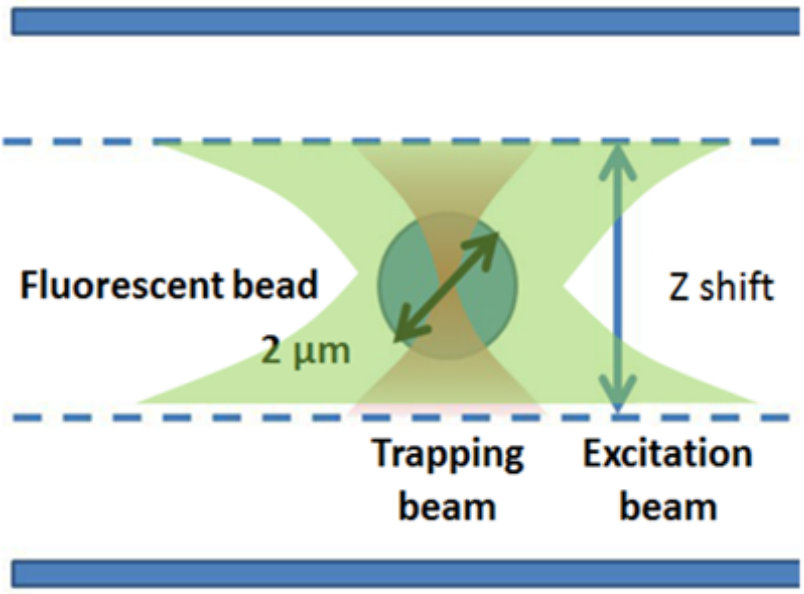

FIGURE 3.6: Sketch describing the method used to obtain the detection volume in z using a 2 μm in diameter bead

The fluorescent signal from the bead was strong enough to use low level excitation and avoid photobleaching within the time scales of the calibration procedure. The obtained dependence of fluorescence intensity on z-shift is shown in Fig. 3.7.

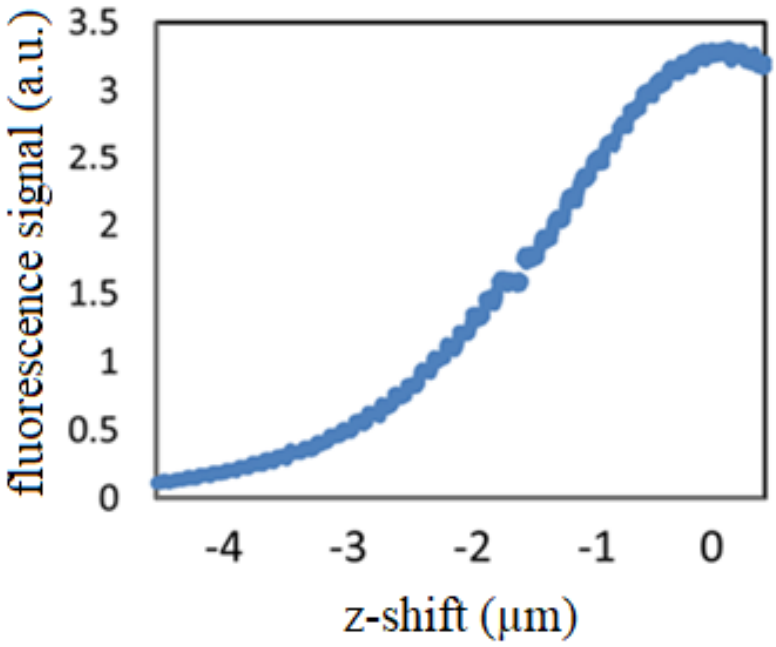

FIGURE 3.7: Recorded fluorescent signal using a 2 μm in diameter bead at different z

We assumed that the excitation intensity is constant along the Z-axis in the detection volume and the obtained Z-profile is due to the depth of field profile of the optical system of the microscope. The lateral dimensions and beam profile distribution were obtained by processing the images of dextran solution fluorescence. Next, for the detection volume $V_{det} = 1,2.10^5 \mu m^3$, that corresponds to $\sim 10^9$ dextran molecules at $10^{-3} mg/ml$ concentration, integral fluorescence intensity was calculated as a sum over the corresponding points of the image obtained for fluorescent dextran solution.

When measuring fluorescence I_{RBC} from RBCs, the trap is always kept in the centre of the excitation beam close to the focal plane, i.e. in this case excitation intensity is set to the maximum value. In case of dextran solution, signal is detected from points with different excitation intensity and detection efficiency. Hence, to compare between the signals for RBCs and solution, the integral intensity measured for the solution was normalized to the X-Y and Z distributions of intensity. Finally, by comparing the normalized intensity value for a dextran solution with known concentration and RBCs, the number of adsorbed molecules was estimated. This procedure yielded 2.10^4 dextran molecules adsorbed per a single RBC in the initial

time point, reaching $\sim 10^5$ molecules after incubation (Fig. 3.2).

To estimate the sensitivity of our measurement system, the calibration curve (Fig. 3.5) was fitted linearly, and its intercept with the Y-axis was obtained. This value corresponded to the signal from ca 100 molecules, hence, this value was taken as a STD error (σ), and the detection limit was estimated as 3σ ($\approx$ 300 molecules). When assessing the number of adsorbed molecules, it is assumed that they are distributed uniformly over the RBC surface. Hence, fluorescence would be scattered/absorbed by the cell that would affect the recorded intensity. Namely, both excitation and emission wavelengths for FITC fit into the absorption spectrum of hemoglobin, and one could expect the dependence of the detected signal on the cell geometry. Also light scattering would result in a difference of fluorescence signals from pure dextran solution and dextran adsorbed on RBC, thus making complicated the comparison of fluorophore concentration. This would result in a systematically lower signal detected from the same number of free dextran molecules in solution compared to adsorbed molecules. In the worst case (total absorption of excitation and emission signals by the cell leading to "shading" of molecules on the opposite side of the cell) this difference would be almost two fold.

3.2 Adsorption mechanisms

Adsorption of macromolecules onto the membrane of RBC is a strong indicator of bridging of RBCs. Nevertheless, to be closer to physiological conditions we wanted to reproduce this experiment by replacing dextran with fibrinogen. Since this protein is known to be one of the main agent contributing to RBCs aggregation, we decided to investigate whether adsorption occurs or not. For concentrations of 1 mg/ml and higher, we observe differences in the fluorescent images after analysing the signal (Fig. 3.8). For fibrinogen, a stronger signal comes out of the outer part of the membrane, exhibiting the typical biconcave shape of a RBC. In the case of dextran, the signal is homogeneously distributed over the whole cell. We can speculate that dextran found its way through the membrane. Nevertheless, no trivial explanation can be found as the size of dextran (70 kDa) is considerable compared to RBCs pumps or even ions channel. We also discarded the possibility for the fluorescent dextran to release its fluorescent component since both are covalently bonded and its is extremely unlikely to see this happening.

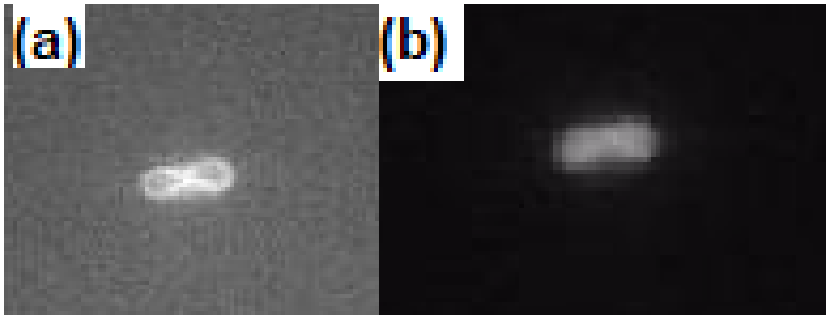

FIGURE 3.8: Adsorption of fluorescent fibrinogen at a concentration of $1mg/ml$ (a) and adsorption of FITC-dextran 70 kDa at a concentration of 20 mg/ml (b)

Using a magnifying lens (x4.5), we examinated the surface of a RBC more carefully. A RBC was trapped with the undiffracted laser beam in the same way adsorption experiments were carried out. Illuminating the RBC under fluorescence revealed the presence of more dots with a more intense signal. We speculate that fibrinogen could bind on the membrane of the RBC onto specific spots contrary to dextran which could cover the membrane more homogeneously in a non-specific way (Fig. 3.9).

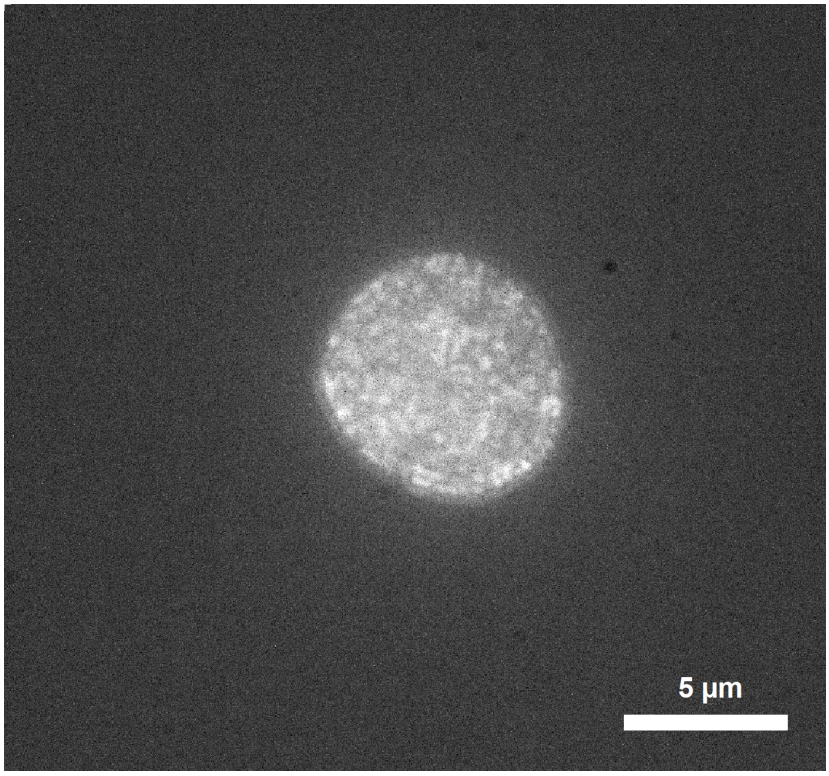

FIGURE 3.9: RBC laying at the bottom of the microfluidic channel continuously washed by PBS after being incubated in a solution of fibrinogen at 2 mg/ml. Signal has been found to be more intense on specific spots that may be synonym of specific binding of fibrinogen

3.3 Summary

Our experimental setup allowed us to rapidly change the surrounding medium of a RBC. Adsorption of macromolecules onto a single RBC has been shown and quantified. This finding is of importance for assessing the RBCs aggregation mechanisms, as for both depletion layer and bridge induced interactions, the adsorption is an important factor that has to be accounted for. In general, the developed approach based on combining optical tweezers with a microfluidic platform has prospective for different applications and allows for detecting the adsorption with a high contrast at single cell level. Unlike other methods, it is possible to measure adsorption of macromolecules free of such potential artefacts as trapped fluid between cells. Our experiments performed in presence of fluorescent fibrinogen suggest that there exists different modes of adsorption and was already tackled by Lominadze et al.

[68]. Experiments to investigate on this matter have been performed with confocal microscopy but were not insightful. We speculate that dextran may penetrate into the membrane after incubating for a couple of hours. Nevertheless, the possible pathways of Dextran through the membrane remain unknown. This approach could be used also for selecting specific cells (e.g. by age) and conditions with rapid change of the suspending media without centrifuging, thus extending the possibilities of investigation of intermolecular interactions and macromolecules adsorption.

Résumé

Notre dispositif expérimental nous a permis de rapidement changer le milieu environnant d'un globule rouge. L'adsorption de macromolécules sur un seul globule rouge a été démontrée et quantifiée. Cette technique est importante pour évaluer les mécanismes d'agrégation entre globules rouges, car pour les interactions induites par la déplétion et le pontage, l'adsorption est un facteur déterminant qui doit être pris en compte. Plus généralement, la technique développée basée sur la combinaison de pinces optiques avec une plateforme microfluidique est prometteuse pour différentes applications et permet de détecter l'adsorption avec un contraste élevé au niveau d'une seule cellule. Contrairement aux autres méthodes, il est possible de mesurer l'adsorption de macromolécules exemptes de potentiels artefacts tels que celui du fluide piégé entre les cellules. Nos expériences réalisées en présence de fibrinogène fluorescent suggèrent qu'il existe différents modes d'adsorption et ont déjà été abordées par Lominadze et al. [68]. Les expériences visant à étudier cette question ont été réalisées en microscopie confocale mais n'ont pas été très perspicaces. Nous supposons que le dextran peut pénétrer dans la membrane après une incubation de quelques heures. Néanmoins, les voies possibles de pénétration du dextran à travers la membrane restent inconnues. Cette approche pourrait également être utilisée pour sélectionner des cellules spécifiques (par exemple en fonction de l'âge) et des conditions avec changement rapide du milieu de suspension sans centrifugation, ce qui étendrait les possibilités d'étude des interactions intermoléculaires et de l'adsorption des macromolécules.

Zusammenfassung

Unser Versuchsaufbau ermöglichte es uns, das umgebende Medium eines RB schnell zu verändern. Die Adsorption von Makromolekülen an eine einzelne RB wurde

gezeigt und quantifiziert. Diese Erkenntnis ist für die Beurteilung der Aggregationsmechanismen der Erythrozyten von Bedeutung, da sowohl für die Depletionsschicht- als auch für die brückeninduzierten Interaktionen die Adsorption ein wichtiger Faktor ist, der berücksichtigt werden muss. Im Allgemeinen ist der entwickelte Ansatz, der auf der Kombination einer optischen Pinzette mit einer mikrofluidischen Plattform basiert, für verschiedene Anwendungen vielversprechend und erlaubt es, die Adsorption mit einem hohen Kontrast auf Einzelzellebene zu detektieren. Im Gegensatz zu anderen Methoden ist es möglich, die Adsorption von Makromolekülen zu messen, die frei von solchen potentiellen Artefakten sind, wie z.B. zwischen den Zellen eingeschlossene Flüssigkeit. Unsere Experimente, die in Gegenwart von fluoreszierendem Fibrinogen durchgeführt wurden, deuten darauf hin, dass es verschiedene Modi der Adsorption gibt, und wurden bereits von Lominadze et al. [68] in Angriff genommen. Experimente zur Untersuchung dieser Frage wurden mit konfokaler Mikroskopie durchgeführt, waren aber nicht aufschlussreich. Wir spekulieren, dass Dextran nach einer Inkubation von einigen Stunden in die Membran eindringen könnte. Dennoch bleiben die möglichen Wege von Dextran durch die Membran unbekannt. Dieser Ansatz könnte auch für die Auswahl spezifischer Zellen (z.B. nach Alter) und Bedingungen mit schnellem Wechsel des Suspensionsmediums ohne Zentrifugation verwendet werden, wodurch die Möglichkeiten der Untersuchung intermolekularer Interaktionen und der Adsorption von Makromolekülen erweitert würden.

Chapter 4

Investigating the 2 models for aggregation: Bridging and depletion

The red blood cells aggregation is a process involving cells adhesion and separation taking place continuously in blood circulation in vivo [11, 1] and in presence of proteins. There exists two theoretical models (bridging and depletion) detailed in 1.5 to describe this phenomenon. However, these models are often presented as being mutually exclusive [29, 58, 113] and the RBCs aggregation mechanisms remains still unclear. Experimental work [12, 22, 23] has already been carried out but most of them focus on the disaggregation of RBC. Our experiments are designed to study RBCs disaggregation and aggregation at a single cell level. (Dis)aggregation forces have been measured, in two model solutions presented as being a pure depletant (Fd-virus) and a molecule that is also a crossbridger (Dextran). Cell-cell interaction surface area was profiled during the whole (dis)aggregation processes with a precise control of their interaction time and force applied on RBCs. Our experiments suggest that the disaggregation and aggregation mechanisms may be of different nature due to the observed discrepancy, mostly in terms of forces.

4.1 Material and methods

Fd virus (wild type) particles are filamentous bacteriophages that are of interest since they have already been used by [114] as a long range depletant (see 1.4.1). The preparation of this virus was carried by the group of Pavlik Lettinga and his two PhD students Olivera Korculanin and Mehrnaz Babaki. They present the advantage to be highly monodisperse. They have a rod-like shape with a length of L = 880 nm and a diameter of d = 6.6 nm. They are therefore situated in the colloidal domain. For comparison, we used a second model solution with dextran (70 kDa) widely used to demonstrate both models (bridging and depletion) and that serves as a plasma expander in the medical field. Our choice aims to show that if dextran

is a depletant then its properties should be comparable to the ones of Fd virus.

RBCs were drawn from the finger tip and washed following the standard procedure detailed in 2.1.1 and resuspended in model solutions. All measurements were performed within an hour otherwise the medium was renewed (RBCs may be altered for longer incubation time). The temperature in the laboratory did not increase more than 2 °C during the measurements and no heating effect due to the presence of the laser beam influenced our measurements. The sample holders were fully filled and sealed to avoid any evaporation leading to an increase of the measured forces. Laser traps were far away from the undiffracted beam and the laser power was low enough (hundreds of milliwatts) to avoid damaging the cells. The measurement procedure itself was very short to furthermore avoid any possible heating or altering of RBCs.

4.2 Computer assisted analysis of experimental data

To measure aggregation/disaggregation forces between two RBCs, it is necessary to have control over a large variety of parameters (contact area, interaction time, forces, ...). Whereas most of the single cell techniques (AFM, micropipettes) consist of measuring interaction energy at a given time-point, optical tweezers allow to perform "dynamic" measurements and thus, the interaction energy can be assessed over time. To do so, all experiments carried out, whether for aggregation or disaggregation, were recorded and later on, analyzed. A manual analysis would be time consuming and results may differ from one operator to another. Therefore, an algorithm has been developed to help us analyzing experimental data. It allows to retrieve with ease three parameters that will be better detailed in this chapter:

- Side edges of the cells
- Trap position
- Timestamps for each frame

4.2.1 Segmentation and edge tracking

After adjusting the optics to have a good image quality and contrast, the whole process has been recorded with 30 frames per second. Time was defined with a millisecond precision and a time stamp was attributed to each frame taken. After

switching to the frequency domain of the image with a Fourier transform, a high-pass filter have been applied. The goal is to better define the contours of both cells. The membrane of a RBC appears white on a dark background (medium) and thus, a high-pass filter is adapted since there is a high contrast difference between the two. Even though edges seem clear enough, it may not be always the case. By pulling the cells, both may slightly get out of focus, making the edge-tracking more difficult. This is mainly due to the fact that trapping but also imaging is done through the same objective i.e. there may be a shift between the focal plane of the image and the trap's "waist". The next step is to track edges. Left and right edges are trivial to get as they correspond to the extremal left/right points of the image (points 1 and 4 in Fig. 4.1). However, edges in between (points 2 and 3 in Fig. 4.1) need to be taken care of with more precautions.

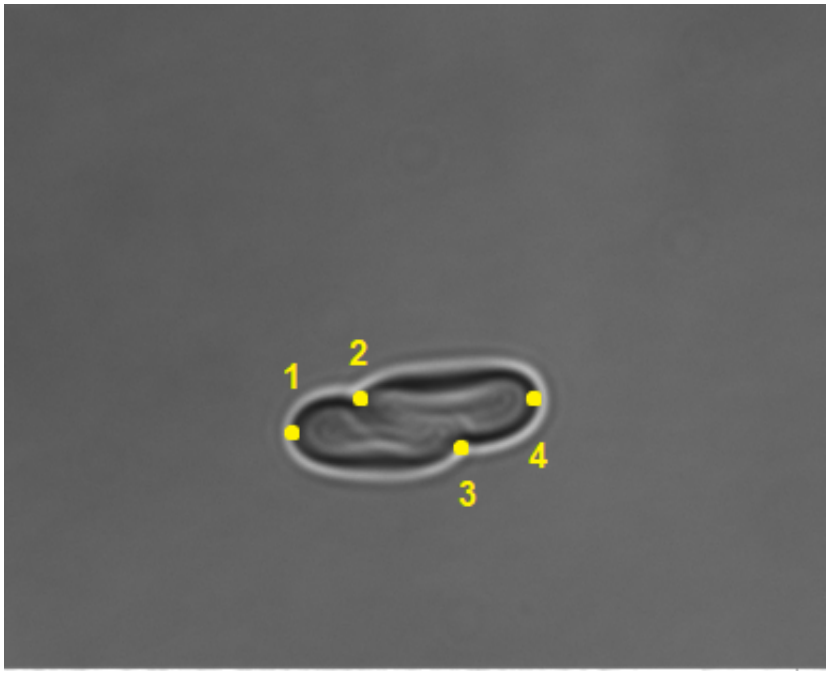

FIGURE 4.1: Two RBCs about to be disaggregated. The four points in yellow represent the points that are tracked during the whole separation process

One of the workaround, is to sum all the pixels along the columns to get the intensity profile of the image. Doing so we end up with 4.2. This reveals 4 peaks corresponding to each extremity of the RBC (Fig. 4.2). Our tracking algorithm is reliable for most of the cases and throughout the whole recordings but cell edges get blurry when a cell escapes the trap. However, this is not an issue for this study.

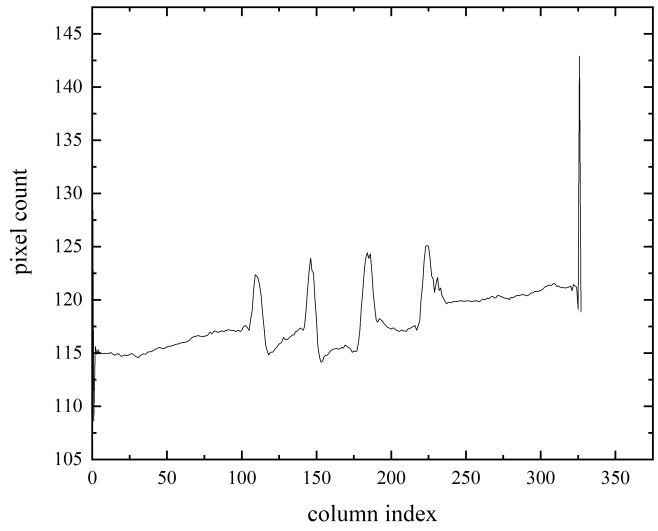

FIGURE 4.2: Number of pixel for each column of a segmented image of two aggregated RBCs. The four peaks directly give the x-position of each RBC's edge

Being able to track these 4 specific points is crucial to look in depth at the dynamics of RBCs (dis)aggregation. For example, tracking the edge of the cells gives access to the diameter of the cell over time and reveals e.g. if elongation takes place during the whole procedure. Trap position combined with the edges of the cell can be directly correlated to the effective force applied to the RBC

4.2.2 Force and interaction energy

When it comes to measuring forces, there are two possible approaches. The first one is to measure the force involved between a pair of cells for a given time and deduce the (dis)aggregation force ($F_{trap} = F_A$ and $F_{trap} = F_D$), directly from the power of the laser, following the Stokes calibration detailed in section 2.3.5.
The second one, is to dynamically measure the force applied onto the RBC over time. For each trap two forces come into play: the optical force from the trap F_{trap} holding the cells and the force from the cell F_{cell} due to the spontaneous aggregation acting in the opposite direction. In both cases, to better grasp the forces involved and due to the biological nature of the samples, 10 pairs of RBCs were taken for a given concentration. The optical force acting on the cell follows Hook's law with k_{cell} its spring constant. (More details to determine k_{cell} can also be found in section 2.3.5):

$$F_{cell}(t) = k_{cell}(x_{trap}(t) - x_{edge}(t)) \tag{4.1}$$

also written as:

$$F_{cell}(t) = k_{cell}\Delta_x(t) \tag{4.2}$$

for simplicity.

The tracking of cell's edges and trap position during the disaggregation of two RBCs can be seen on Fig. 4.3

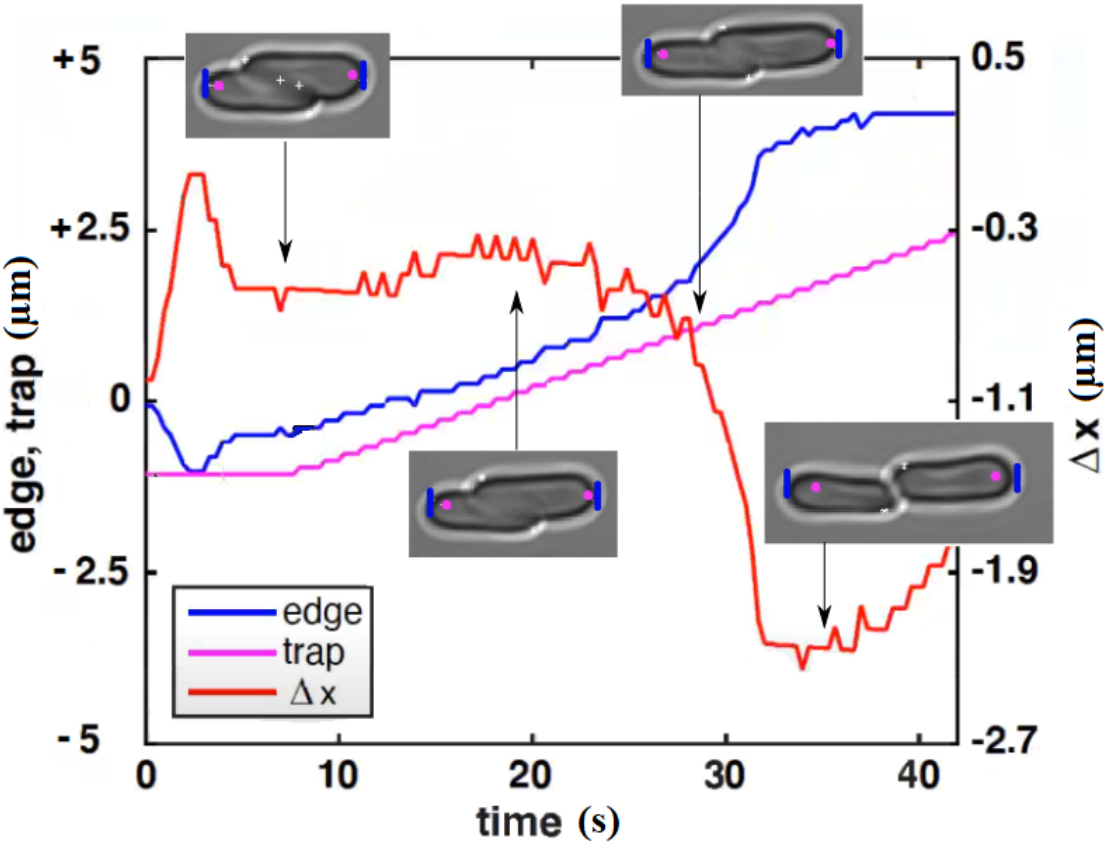

FIGURE 4.3: Disaggregation of two RBCs in presence of dextran. In purple the position of the trap generated by the SLM and in blue the position of the edge of the cell detected by the tracking algorithm. The red line Δx represents the distance between the two. The top RBC is being pulled with constant steps and laser power

4.3 (Dis)aggregation forces in dextran

Measurements were carried out as presented in section 2.3.6. The linear overlap between the two RBCs was set to $4.5\mu m$ and the resulting dextran-induced RBCs interaction forces using Stokes calibration (see section 2.3.5) are shown in Fig. 4.4.

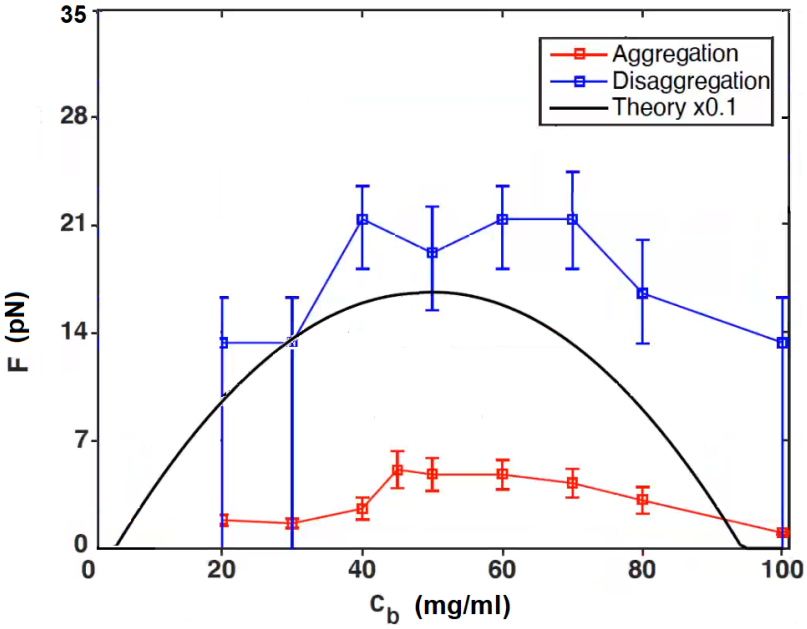

FIGURE 4.4: Bell shape for disaggregation (blue) and aggregation (red) of a pair of RBCs with an initial linear overlap distance of 4.5 microns. The theoretical line (black) was calculated using Eq. 1.34 (N>10)

The aggregation force F_A increases up to the peak at 50 mg/ml, reaching 5 ± 1 pN and decreases after until it reaches a point without any interaction around $100mg/ml$. One should notice the abundance of stomatocytes at higher concentrations ($> 80mg/ml$).

Regarding the disaggregation force F_D in dextran, a different behaviour was observed compared to the aggregation. First, one should acknowledge that obtaining the disaggregation force is not an easy task. It requires to scan different forces ($13.3 \pm 1.3, 16.5 \pm 1.6, 18.9 \pm 1.9, 21.3 \pm 2.1 pN$ in the case of dextran (70 kDa)). In fact, force cannot be increased step-wisely because if the pulling force is not sufficient, RBCs will spontaneously aggregate and the interaction is such that it is impossible to separate them. Moreover, RBCs are biological objects with a certain level of variability and the disaggregation force may vary from a pair to the other. Nevertheless,

the disaggregation force F_D is considered to be the force which is sufficient to separate 70 % of the pairs and the interaction force reached a maximum at 50 mg/ml and at 70 mg/ml and decreased afterwards. One should put an emphasis on the valley at 50 mg/ml, where the interaction force notably decreases, and which was not really observed before using other single-cell techniques. Even though the peak representing the maximum of aggregation seem to match with the theoretical curve, it needs to be re-scaled in order to fit quantitatively the experimental results. The theoretical curve was derived from Eq. 1.34 and thus, the electrostatic repulsion has been neglected. It should rather be seen as a qualitative comparison since the electrostatic repulsion varies with the inverse of the distance separating the two RBCs.

At any concentration, the ratio F_D/F_A was roughly greater than 4. Such difference implies that the disaggregation and aggregation of RBCs may involve mechanisms of different nature. The depletion model does not provide information about the origin of this difference between the two forces F_A and F_D and thus may be incomplete to fully describe the aggregation of RBCs.

Comparison with the depletion theory indeed yields significant difference. Although, in recent works, the adjustment of glycocalyx parameter (penetration) led to the similar bell shapes (concentration dependence) [115]. Nevertheless, our results with optical tweezers still show an about 4 fold difference in magnitude between F_A and F_D. Such a gap between forces has not been quantitatively shown until now since most of the single cell methods (AFM, MAT) focused on the disaggregation of RBCs. OT measurements reveal more details about the nature of forces involved in (dis)aggregation mechanisms.

4.4 (Dis)aggregation forces in Fd virus

Fd virus induced RBCs interaction forces are shown in Fig. 4.5. In this case, the dependence of F_A and F_D followed each other and the ratio F_D/F_A was close to unity. Both F_A and F_D forces had monotonic and linear enhancement from 2 to 7 mg/ml. It is worth to note that, for Fd virus, finding stationary condition during measurement was very difficult. A slight perturbation of F_{Trap} was enough to break the equilibrium in either direction of cells aggregation or disaggregation. This shows that $F_A \approx F_D$. Therefore, only one setpoint for F_{Trap} was used, which was 1 pN higher than F_A. For this reason, the F_D values might be slightly overestimated. The linear dependence of the force vs concentration together with the (dis)aggregating forces

F_D and F_A being in the same order of magnitude are typical of a pure depletant and thus, expected.

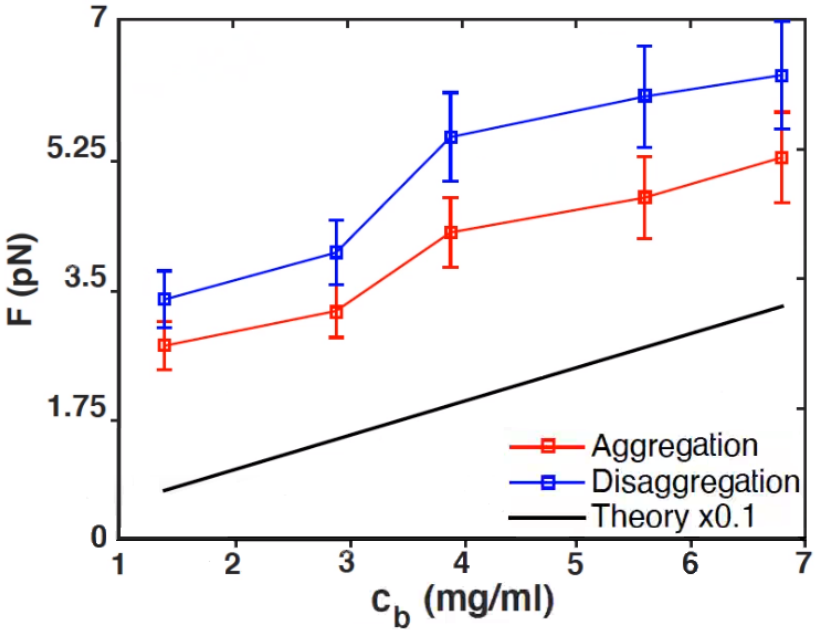

FIGURE 4.5: (Dis)aggregation force F_D varies linearly as a function of the concentration of Fd virus. Compared to dextran (70 kDa) both aggregation and disaggregation forces are in the same order of magnitude as expected for a pure depletant. The theoretical line (black) was calculated using Eq. 1.45 (N>10)

To confirm that Fd virus behaves as a pure depletant around RBCs, single molecule fluorescence microscopy was implemented. Figure 4.6 shows behavior of fluorescently labeled Fd virus in a buffer solution containing non-labeled Fd virus (1 : 700 ratio at total concentration of 4 mg/ml). Fd virus are repelled from the surface of RBCs and none of them has be found in the contact area i.e. in between two RBCs. One can note that the significant inter-cellular distance. It is due to the large size of depletant itself ($L = 880$ nm).

Using optical tweezers, we could not assess (dis)aggregation forces (F_A and F_D) at higher concentration ($C_b > 8mg/ml$) of Fd virus due to the viscosity of the medium that was too high to move cells freely. This is in principle possible but one would need considerable time to get enough statistics. However, it is very likely that the force versus concentration dependence remains the same.

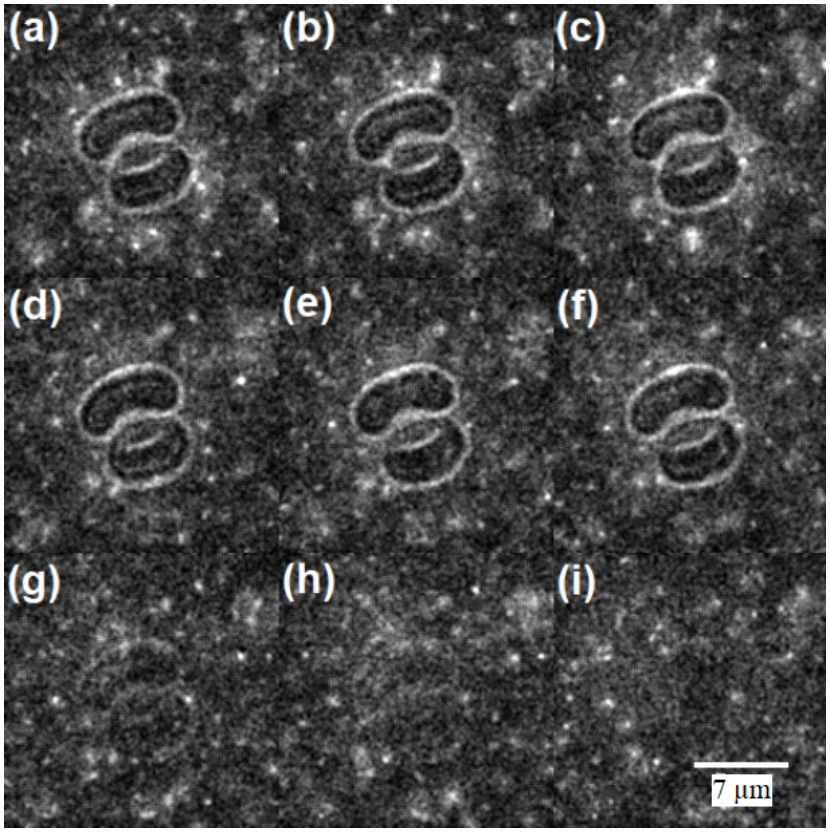

FIGURE 4.6: Pair of two cells observed by means of single molecule fluorescence microscopy at a concentration of 4 mg/ml of Fd virus. Both fluorescence LED ($\lambda = 470\ nm$) and halogen lamp turned on to visualize the rods as well as the non stained RBCs (a)-(f), the intensity of the halogen lamp was turned off throughout (g)-(i). Courtesy of Olivera Korculanin

4.5 Discussion

The bell-shaped dependence of the RBCs aggregation on concentration of dextran has been reported earlier [97, 15, 16]. However, the peak concentrations varied over a wide range (c.a. $20 - 40\ mg/ml$) depending on the measurement method used. One speculation could be that one of the reasons for this would be the differences between F_A and F_D, which was not well-accounted before.

Light scattering (i.e. measuring intensity of the light scattered on sample) [16] and microscopic aggregation index (i.e. counting the size of aggregates) [15] techniques report an interaction peak around $30 - 50\ mg/ml$, with the interaction vanishing at $> 80\ mg/ml$. We also found that RBCs interactions are extremely low at $> 80\ mg/ml$ and completely vanish near 100 mg/ml. It also should be taken into account that for

high concentration of dextran, macromolecules may affect the shape of RBCs. This could justify the presence of stomatocytes, as already stated. Even if we can't emit hypothesis regarding this morphological change, it can be reported that no aggregation between two stomatocytes using OT has been observed. Nevertheless, some quantitative similarities in our data could be found with the literature [12].
If we compare experimental methods, AFM is probably the closest to OT as it allows to measure forces at a single cell level. Besides and similarly to the micropipet aspiration technique, there is still a mechanical contact between the object and the measuring device. We should also remind that in our measurements, the contact surface area is well controlled, whereas for AFM the whole upper surface area of the RBC comes into play and the relative orientation of cells is imposed by the system. Besides, the mechanism involved in the measurements of disaggregation forces F_D is different. With AFM, a cell is stuck on the substrate while the other one is lifted in a "face-to-face" manner. With OT, RBCs are held in suspension and one slides onto the other without any external mechanical contact. Despite these peculiarities, one could expect that both methods should agree on the maximum in the bell-shape dependence of interaction energy vs concentration but this is has not always been the case [21].
In terms of interaction forces for F_D virus, it behaves as a pure depletant for a concentration range between 2 and 8 mg/ml. One should mention that RBCs always kept their biconcave shape in presence of Fd with the concentration range we chose (between 2 and 8 mg/ml). Even though its nature differs from dextran, it shows what can be expected from a system where pure depletion takes place. (Dis)aggregation forces (F_A and F_D) follow a linear trend and there is no need for a "penetration of glycocalyx" parameter to explain this behavior as in [58]. In fact, if the contact surface area between two RBCs is purely depleted the forces necessary to (dis)aggregate RBCs should not differ too much (considering that the interaction between RBCs membrane brushes can be neglected).

4.6 Traces analysis in model solutions : dextran and Fd virus

Most of the experiments until now did not consider the contact time between cells and forces between RBCs were measured in a "face to face" manner compared to "sliding" as it is the case for OT. Even if they give a first outlook on RBCs disaggregation, they may dissimulate important features of this particular mechanism. Our experiments are dynamic and aim to show differences for the disaggregation

process in a pure depletant and in a cross-bridger solution. All pairs of cells were analyzed using the tracking algorithm. For both dextran (70 kDa) and Fd virus, data follow the same trend and can be overlaid almost perfectly. This indicates that the age of RBCs and their possible change in rigidity, deformability and other physical parameters had no influence on the measurements.

Using the same algorithm as in 4.2, traces representing the applied force on the cell as a function of the center to center distance d_{c-c} have been generated. The raw data consist of: cell's edge position, the trap position and the timestamp for each frame. Therefore, d_{c-c} for a given time stamp can be retrieved with ease. Forces engendered by the optical trap F_{OT} have been calculated using the thermal noise calibration (see section 2.3.5) to determined the Hooke constant and the related equation.

$$F_{OT} = -K_{OT}\Delta x \tag{4.3}$$

Δx is the distance between one optical trap and the edge of one cell as it is already displayed on Fig. 4.3. The effective force applied on each RBC can also be calculated using the bead-cell calibration (section 2.3.5). It would give an even more accurate representation of the force applied on the cell but it is still in progress. For dextran, traces for disaggregation (Fig. 4.7) were analyzed with and without interaction time to observe its possible influence on an eventual formation of bridges. As it can be interpreted on Fig. 4.7, the pulling velocity has its importance in understanding the mechanism of RBCs disaggregation in dextran. If one cell is pulled away from the other too fast or abruptly, the system has a linear response (Fig. 4.7 (b,d)) and may not be a good example to account all the force contributions during the disaggregation. A lower pulling velocity (Fig. 4.7 (a,c)) gives us a different response, slightly more complex to intepret and indicates that the pulling velocity we selected is reasonable to study the disaggregation of RBCs.

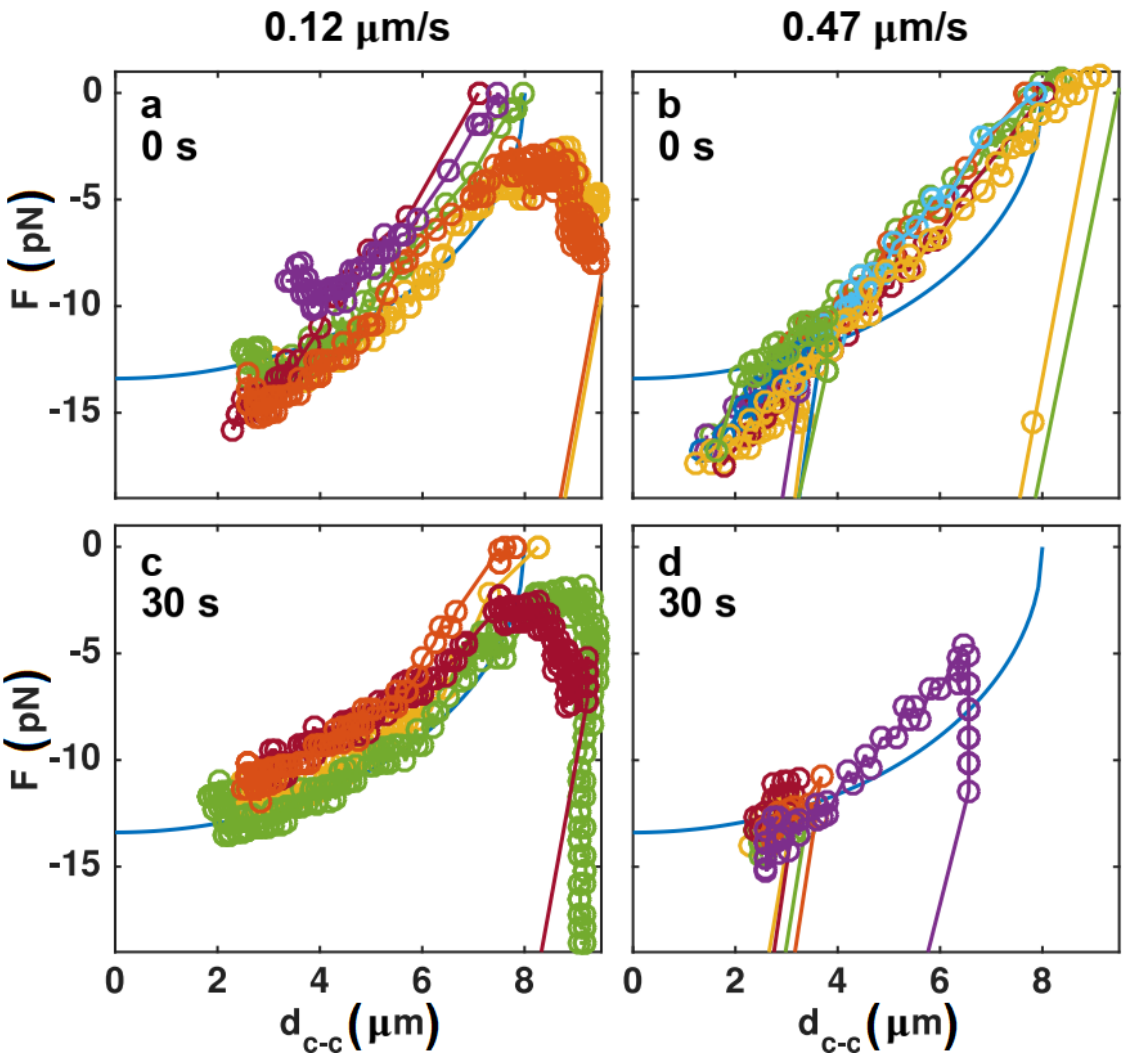

FIGURE 4.7: Pulling force applied on the RBC as a function of the distance (center to center) d_{c-c} between the two RBCs. The pulling forces are gathered for $c = 50\ mg/ml$ dextran (70 kDa) with a velocity of $v = 0.12\ \mu m/s$ (a,c) and $v = 0.47\,\mu m/s$ pulling rates (b,d), for zero (a,b) and 30 seconds interaction time (c,d), showing details of the disaggregation dynamics. Each color corresponds to a different disaggregation experiment. The solid lines are theoretical curves calculated using Eq. 1.34

For low separation velocities ($v_s = 0.12\mu m/s$) in dextran, the force applied onto the RBCs does not instantly decrease after starting to pull, as it is the case for Fd-virus (Fig. 4.8) . In fact, it can be speculated that there are three stages based on our graphs. Fig. 4.9 may represent this description more accurately.

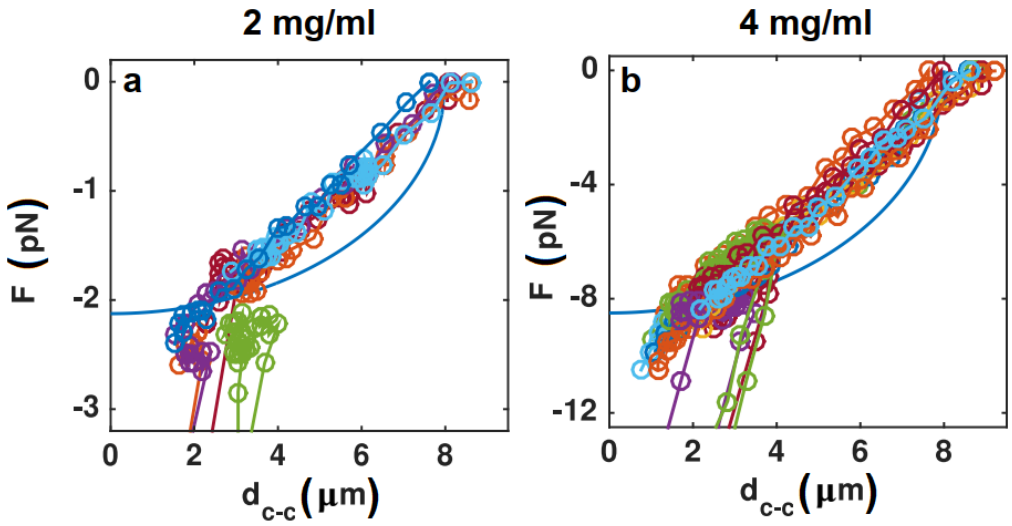

FIGURE 4.8: The force traces for Fd virus at (a) $c = 2\ mg/ml$ and (b) $c = 4\ mg/ml$ showing details of the disaggregation dynamics with a velocity of $v = 0.12\,\mu m/s$. The solid line in each graph is the theoretical prediction according to the depletion model for ideal rods (see Eq. 1.45).

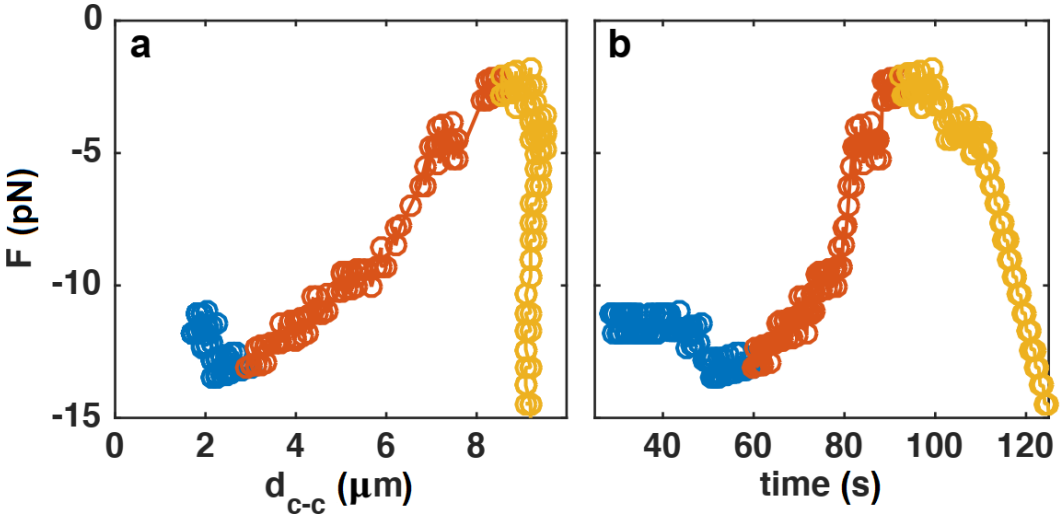

FIGURE 4.9: The three stages in a pulling traces for one dextran dataset at 0.12 $\mu m/s$ pulling rate, plotting the trapping force vs d_{c-c} (a) and time (b). Stages I, II and II are respectively in blue, red and yellow

For a low separation velocity $v_s = 0.12\mu m/s$, the dextran force traces do not immediately decrease, as is the case for Fd virus, but instead, the curves display three

stages with increasing time, as can be more clearly seen in Fig. 4.9. In *stage I*, immediately after starting to pull, the force applied on the cell increases while d_{c-c} remains almost constant. Towards the end of *stage I* (in blue), the systems yields: d_{c-c} starts to increase, while the applied force decreases. This is *stage II* (in red) where the cells flow, until $d_{c-c} \approx 2R$, so when the cells transition to side-to-side contact. The F - d_{c-c} curves for interaction timespan $t_{int} =$ 0 and 30 seconds are, however, different. For $t_{int} = 0\ s$ the curve is more steep than for $t_{int} = 30\ s$. In *stage III* (in yellow), when the cells have not separated, the force slowly starts to increase again, and the cells separate or tether (Fig. 4.12), where d_{c-c} increases slightly, but the force increases significantly. Most of the cells that tether finally reaggregate as the pulling trap keeps moving.

At a higher separation velocity $v_s = 0.47 \mu m/s$ (Fig. 4.7 (b,d)) and in the case of Fd virus (Fig. 4.8 (a) and (b)) , F_{cell} instantly jumps roughly to a certain force. This force is $-2\ pN$ and $-8\ pN$, respectively for a concentration of 2 mg/ml and 4mg/ml for Fd-virus and about $-14\ pN$ for dextran at 50mg/ml. After this sudden jump, F_{cell} decreases with increasing d_{c-c}, i.e. the cells follow the optical trap and the system starts to flow instantly, such that *stage I* is skipped and the *stage II* is instantly entered. Alternatively, the RBCs escape the trap which is more often the case for $t_{int} = 30\ s$ than for $t_{int} = 0\ s$. The phase transition into *stage III*, is skipped for almost all cells, and the cells either reaggregate immediately or separate.

4.7 Influence of interaction time on disaggregation

4.7.1 Influence of interaction time on disaggregation with dextran

The time of interaction between RBCs in presence of dextran can give a hint regarding the underlying mechanism of RBCs' aggregation. In fact, a time dependence may be directly related to the formation of bridges. We can expect that a longer interaction timespan favours the formation of bridges. An absence of time dependence may be synonym of a pure depletion scenario, where time is not expected to play a major role. Fig. 4.10 shows the effect of time but also pulling velocity on the separation probability of RBCs. Data in Fd-virus solution and physiological media (serum, plasma) are still being processed and may reveal more information about the effect of time on the disaggregation of RBCs.

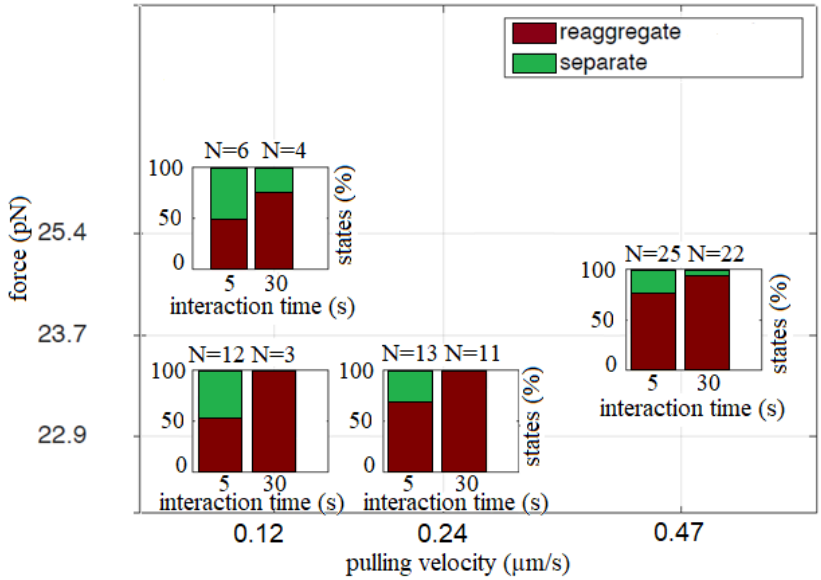

FIGURE 4.10: Separation probability between two RBC at a chosen force and in presence of Dextran at a fixed concentration of 50 mg/ml with a pulling speed of 0.12 $\mu m/s$, 0.24 $\mu m/s$ and 0.47 $\mu m/s$. The initial overlapping distance was set to be 4.5 μm

Traps were generated with the usual configuration. Forces have been selected in a way that they were slightly higher than the average separation forces. The possible effect of the pulling velocity was also investigated. Waiting time spans are for most of the experiments $t_{int} = 0$ s (no waiting time) and $t_{int} = 30$ s. One should keep in mind that there always is a time span of 2 seconds when RBCs are brought together in contact.

For a force of 22.9 pN, it can be seen that a longer waiting time leads to a lower probability of disaggregation. This supports the idea that more bridges may get formed after longer waiting time. For the same pulling velocity, taking a force which is even higher such as 25.4 pN seems to facilitate the dissociation of cells after a waiting time of 30 s. When the pulling velocity is increased by a factor of 2 and the force remains constant (22.9 pN), this separation probability gets even lower. It is also valid if this pulling velocity gets even higher with 2 $\mu m/s$. This can be explained by the fact that the pulling is too abrupt and not enough time is given to the system to re-equilibrate.

4.8 Possible mechanisms

One of the possible scenarios is about mobile cross-bridges. Proteins present in plasma may form cross-bridges in-between the glycocalyx of two RBCs and these

bridges may move as RBCs disaggregate. Fig. 4.11 illustrates this idea. Fig. 4.11 expresses in which manner the interaction energy density could build up during the disaggregation with optical tweezers. As the contact area between the two RBCs diminish, the number of bridges remains (quasi) constant demanding a higher force to separate cells.

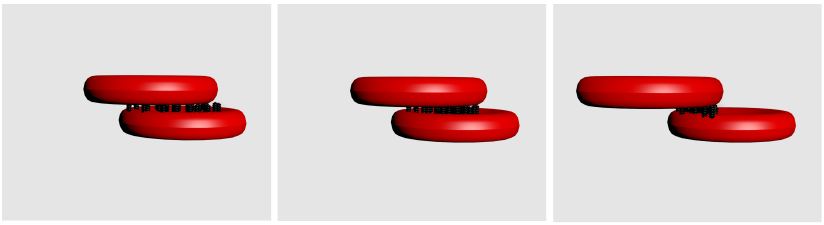

FIGURE 4.11: 3D scheme representing a model with migrating cross-bridges. Bridges stay in the contact area as one RBC is pulled away from the other. In this scenario, the interaction energy density builds up as the surface decreases

An experimental hint could be the presence of "tethers" for high concentration ($C_b < 50$ mg/ml) of dextran (70 kDa). This term may be slightly inaccurate since it refers to the formation of a bond between a cell and substrate in cell biology. Nevertheless, a tether, in this context, refers to two RBCs that are bonded by a point contact between them (see Fig. 4.12). Most of the time this point contact is so strong that our OT could not break it. A plausible explanation is that bridging proteins may drift on the membrane and, while one cell is sliding onto the other during the disaggregation process.

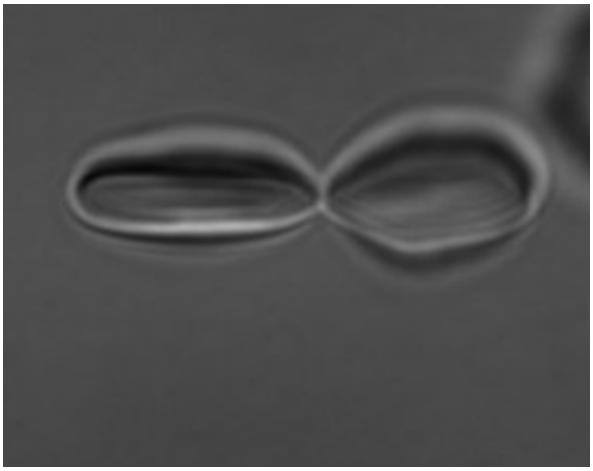

FIGURE 4.12: Microphotography of two RBCs during the disaggregation progress in Dextran $50 mg/ml$ and referred as a tether

The linear dependence between the force and the linear overlap distance could be synonym of migrating crossbridges (Fig. 4.13). In this model, the number of bridges is supposed to be proportional to the contact area between cells (considering a homogeneous distribution of bridges).

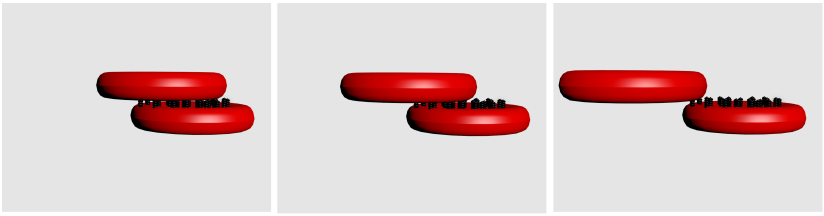

FIGURE 4.13: 3D scheme representing a model with non-mobile cross-bridges. The number of bridges diminishes as the surface area between 2 RBCs decreases during the disaggregation

Qualitatively, curves in plasma, serum or even in dextran show a similar trend. For a trap pulling a RBC with a constant force, the disaggregation seems to accelerate towards the end of the process when the contact area between the two RBC diminishes. This could be due to the fact that more bridges break as the trap keeps pulling. The interaction energy density in this scenario would decrease over time as the contact area between RBC gets smaller. Nevertheless, it is a rather simplistic view and both mechanisms could take place. One can think of an interplay between migrating crossbridges and a formation-breaking rate during the disaggregation.

4.9 Summary

In this chapter, the (dis)aggregation forces between two RBCs are assessed in order to better understand the mechanism of (dis)aggregation. We show that dextran (70 kDa) may not be a good candidate to back up the depletion model. Similarly to plasma, it is reported that the disaggregation force F_D is more than 4 fold higher compared to the aggregation force F_A. In the case of a pure depletant, forces are in the same order of magnitude $F_A \approx F_D$ and disaggregation data follow a similar trend. Our experiments suggest that for this given disaggregation methodology, dextran does not behave like depletant only as it follows a different trend compared to Fd virus, which is a pure depletant. Whereas dextran curves could be split in 3 stages to describe the force applied on one cell during the disaggregation process, Fd virus depicts only two phases and thus, skipping the yielding stage I.
Further analysis of disaggregation in autologous plasma are still being processed

and may reveal the true role of proteins in plasma and which model may be applied to describe RBCs' aggregation in physiological situations. Our measurements suggest that longer interaction time may enhance the interaction energy between RBC in presence of dextran, as bridges may have more time to form. This study suggests that the two interaction mechanisms often presented as mutually exclusive may both contribute in the mechanism of RBCs' aggregation.

Résumé

Dans ce chapitre, les forces de (dés)agrégation entre deux GR sont évaluées afin de mieux comprendre le mécanisme de (dés)agrégation. Nous montrons que le dextran (70 kDa) n'est pas un bon candidat pour soutenir le modèle de déplétion. Comme pour le plasma, il est rapporté que la force de désagrégation F_D est plus de 4 fois supérieure à la force d'agrégation F_A. Dans le cas d'un déplétant pur, les forces sont du même ordre de grandeur $F_A \approx F_D$ et les données de désagrégation suivent une tendance similaire. Nos expériences suggèrent que pour cette méthodologie de désagrégation donnée, le dextrane ne se comporte pas comme un déplétant car il suit une tendance différente de celle du virus Fd, qui est un déplétif pur. Alors que les courbes du dextrane pourraient être divisées en 3 étapes décrivant la force appliquée sur une cellule pendant le processus de désagrégation, le virus Fd, lui, ne représente que deux phases et donc, saute l'étape I d'élasticité. D'autres analyses de désagrégation dans le plasma autologue sont encore en cours et pourraient révéler la vraie fonction des protéines contenues dans plasma et le modèle qui pourrait être appliqué pour décrire l'agrégation des globules rouges. Nos mesures laissent penser qu'un temps d'interaction plus long pourrait augmenter l'énergie d'interaction entre les globules rouges en présence de dextrane, car les ponts pourraient avoir plus de temps pour se former. Cette étude suggère que les deux mécanismes d'interaction souvent présentés comme étant mutuellement exclusifs peuvent tous deux contribuer au mécanisme d'agrégation des globules rouges.

Zusammenfassung

In diesem Kapitel werden die (Dis)Aggregationskräfte zwischen zwei RB untersucht, um den Mechanismus der (Dis)Aggregation besser zu verstehen. Wir zeigen, dass Dextran (70 kDa) möglicherweise kein gutes Aggregationsmittel ist, um das Depletionsmodell zu untermauern. Ähnlich wie bei Plasma wird berichtet, dass die Disaggregationskraft F_D mehr als viermal so hoch ist wie die Aggregationskraft

F_A. Im Falle eines reinen Depletants liegen die Kräfte in der gleichen Größenordnung $F_A \approx F_D$ und die Disaggregationsdaten folgen einem ähnlichen Trend. Unsere Experimente legen nahe, dass sich Dextran bei dieser gegebenen Disaggregationsmethode nicht wie ein Depletant verhält, da es einem anderen Trend folgt als das fd-Virus, das ein reines Depletant ist. Während Dextran-Kurven in 3 Stufen aufgeteilt werden könnten, um die Kraft zu beschreiben, die während des Disaggregationsprozesses auf eine Zelle ausgeübt wird, stellt das fd-Virus nur zwei Phasen dar und überspringt somit die Ertragsstufe I. Weitere Analysen der Disaggregation in autologem Plasma sind noch in Bearbeitung und könnten die wahre Rolle der Proteine im Plasma aufdecken und zeigen, welches Modell zur Beschreibung der RB-Aggregation angewendet werden kann. Unsere Messungen lassen vermuten, dass eine längere Wechselwirkungszeit die Wechselwirkungsenergie zwischen den Erythrozyten in Gegenwart von Dextran erhöhen könnte, da Brücken möglicherweise mehr Zeit zur Bildung haben. Diese Studie legt nahe, dass die beiden Wechselwirkungsmechanismen, die oft als sich gegenseitig ausschließend dargestellt werden, beide zum Mechanismus der RB-Aggregation beitragen könnten.

Chapter 5

Effect of spectrin network elasticity on the shapes of RBC doublets

The research presented here, has been published [116] as a result of our collaboration with Masoud Hoore from the Forschungszentrum Jülich. More details about the theoretical model used in his simulations can be found in Hoore et al. [116]. RBC doublets and more complex aggregates (up to 7 cells) are here studied in 3 dimensions. Simulations had already been performed [12] in a 2 dimensional space in which shear elasticity does not exist and therefore, it is questionable whether the whole phase diagram has been explored or not in these previous 2D simulations. Using high resolution triangulated membranes in 3 dimensions, the phase space of RBC doublets and rouleaux shapes with a focus on the shear elasticity is established and qualitatively complemented by experiments.

5.1 Introduction

Knowing the inherent mechanism of RBCs aggregation is of major interest but should not prevent us from studying the structural aspects of RBCs aggregates. At the origin of the rouleau formation, two RBCs form a doublet which is the point of nucleation for larger aggregates. Doublets are also the simplest structure resulting from the balance between aggregation forces and RBCs mechanical properties and as such are a relevant system to model and understand the mechanical stability of aggregates. They are also likely the most common type of aggregates at higher shear rates and we can suspect that their morphology, which governs the total area of contact between aggregated cells, is intimately related to their stability in dynamic situations. For simplification, early studies considered the contact area between RBCs to be flat [27, 25, 117]. Thanks to the progress in computing performance, numerical simulations showed that two vesicles with a given bending rigidity and an identical

volume have a contact area that is rather sigmoidal when the interaction energy is sufficiently high. Moreover, the role of the spectrin network in RBC and its shear elasticity was omitted and we found interesting to implement it in our model together with the bending rigidity. Numerical findings are compared to our experimental micro-images under bright field microscopy.

5.2 Adhesion model

The membrane model is not described here as it does not affect the understanding of this research and is based on classic considerations of membrane mechanics (see [116] for more details). To represent aggregation between two RBCs, attractive interactions between two membranes are introduced similar to other models [118, 119, 12, 120] of interacting membranes. Note that such interactions cannot be directly associated with any underlying mechanism for RBC aggregation (e.g. depletion or bridging). Therefore, this model constitutes an effective representation of the aggregation between RBCs, which is characterized by the strength of attractive interaction and contact area as it can be observed in plasma or in model solutions (e.g. in dextran). The attractive interaction between adjacent vertices of membranes in contact is modelled by the Lennard-Jones (LJ) potential.

$$U_{LJ}(r) = 4\epsilon[(\frac{\sigma}{r})^{12} - (\frac{\sigma}{r})^{6}] \tag{5.1}$$

where ϵ and σ are the energy and characteristic length of the LJ interaction. The LJ potential is cut off at $r_{cut} = 2.5\sigma$.The contact interaction of two RBCs can be represented by the adhesion free energy [118, 119]

$$E_{adh} = -\Gamma A_c \tag{5.2}$$

where Γ is the adhesion strength and A_c is the contact area. Providing that the adhesion is modeled by a pairwise interaction, such as the LJ potential in Eq. 5.1, between membrane vertices, the adhesion strength Γ can be related to the potential energy ϵ. If N_c vertices from one RBC interact with the vertices from another RBC, the total adhesion energy is $-N_c\tilde{\epsilon}$, where $\tilde{\epsilon}$ is the effective adhesion energy of one RBC vertex with the other RBC vertices. $\tilde{\epsilon}$ can be calculated approximately by considering the closest vertices to a vertex from another membrane.

In a minimal energy state, a vertex sits on top of three vertices in a tetrahedral configuration with equal distance σ to all of them. The adhesion energy of this vertex with the other closest neighbors sums up to about -5.37ϵ. Consequently, the

total adhesive energy, when N_c vertices participate in the adhesion from each membrane, is equal to about $-5.4N_c\epsilon$. However, this high symmetry situation of course does not occur for all of the vertices, resulting in a somewhat smaller adhesion energy. As vertices of a membrane are homogeneously distributed on the membrane, $Nc/Ac = N/A$, in which N and A are the total number of vertices and total area of the RBC membrane. Thus, the adhesion strength is directly proportional to the vertex density N/A, i.e. $\Gamma = N_c\tilde{\epsilon}/A_c = N\tilde{\epsilon}/A$. This implies that the adhesion strength is proportional to the LJ parameter ϵ via $\tilde{\epsilon}$. The reduced adhesion energy, γ, is defined as the ratio of the total possible adhesion energy (i.e. when $A_c = A$) to the bending energy of a sphere:

$$\gamma = \frac{\Gamma A}{8\pi\kappa_c} = \frac{N\tilde{\epsilon}}{8\pi\kappa_c} \tag{5.3}$$

The ratio $\tilde{\epsilon}/\epsilon$ as a function of γ and reduced volume v ($v_1 = v_2 = v$) is presented in Fig. 5.1, which shows how the effective adhesion energy $\tilde{\epsilon}$ is related to the pairwise LJ energy ϵ.

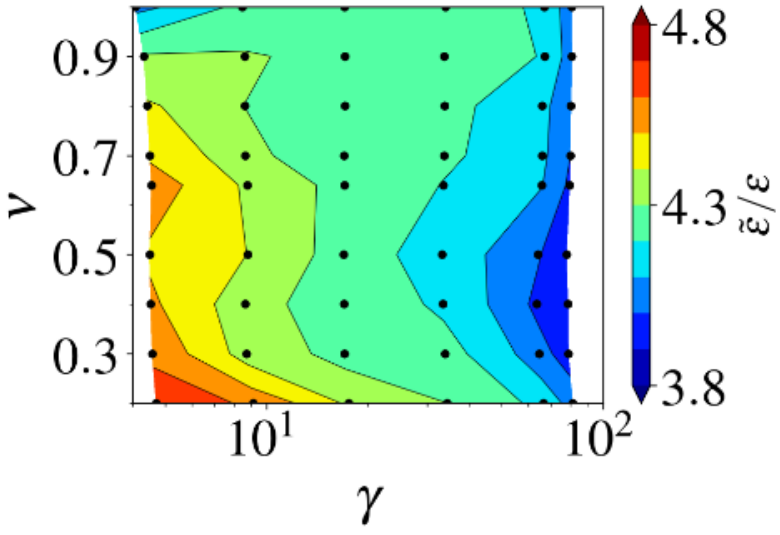

FIGURE 5.1: The ratio of the effective adhesion energy $\tilde{\epsilon}$ to the pairwise energy ϵ. This ratio depends weakly on the configuration of the two adhered RBCs. Simulations are conducted for the system until it reaches equilibrium. The reported data are averaged over 250 un-correlated points in simulations from the equilibrium states. On average, $\epsilon/\tilde{\epsilon} = 4.23 \pm 0.03$. (Simulations by Masoud Hoore)

For different ϵ values, the equilibrium distance between the two membranes may

change, leading to a different relation between ϵ and $\tilde{\epsilon}$. This is the main reason for an increase in $\tilde{\epsilon}/\epsilon$ with decreasing γ. A very weak dependence of $\tilde{\epsilon}/\epsilon$ on the reduced volume v can be due to the local curvature of contact. Additionally, for large enough v, membranes in a doublet configuration are under tension, which may contribute to the dependence of the ratio $\tilde{\epsilon}/\epsilon$ on v. Finally, the amplitude of thermal fluctuations of a RBC membrane is known to be spatially non-uniform along the surface [121, 122], and to depend on membrane shape, local curvature and tension [123]. Membrane thermal fluctuations are included in the model and would effectively introduce short-range repulsion between two membranes.

5.3 Experimental methods

Blood was obtained by finger pricking from healthy donors (see section 2.1.1). RBCs were washed twice with Phosphate Buffered Saline (PBS, 290 mOsm) following the standard procedure [124]. Then, RBCs were resuspended in several solutions to obtain several doublet configurations. In order to have various adhesion energies, we prepared dextran solutions with different molecular weights:

- 40 kDa at a concentration of 10 mg/ml with an adhesion energy close to 1 $\mu J/m^2$;
- 70 kDa at a concentration of 20 mg/ml with an adhesion energy close to 4 $\mu J/m^2$;
- 500 kDa at a concentration of 10 mg/ml with an adhesion energy close to 6 $\mu J/m^2$.

Fibrinogen was added with a concentration of 6 mg/ml to autologous plasma as it does not induce spontaneous aggregation on its own. A hypotonic solution of NaCl at 0.6% was also prepared to increase RBCs' volume. To induce aggregation, dextran 70 kDa was added with a concentration of 20 mg/ml into this solution. The hematocrit level was kept at 0.5% in every sample. Such a low concentration of RBCs allows us to manipulate cells freely with holographic optical tweezers. Then, cells were held by pinning two opposite ends with four optical traps. RBCs were brought together to form doublets and the traps were released, so that they can spontaneously aggregate. As dextran is known to induce spontaneous aggregation [21], we observed the formation of rouleaux over time. Finally, RBCs were let to sediment for 30 mins and micro-photographs were taken using a 60-fold objective. Morphologies of these aggregates were characterized similarly to those in the simulations.

5.4 Results on doublet shapes

The theoretical adhesion strength Γ is related to dextran and fibrinogen concentrations in experiments [125, 21]. RBCs doublet shapes are governed by the adhesion strength (Γ, or equivalently), the reduced volumes v_1 and v_2, and the elastic parameters such as bending rigidity κ_c and shear elasticity G. The adhesion strength of the RBCs membranes is about $1\,\mu J/m^2$ in plasma and about $10\,\mu J/m^2$ in dextran solutions [24], corresponding to $\gamma = 4$ in plasma and $\gamma = 40$ in dextran. The RBC volume is also subject to change in different solutions, and may also vary from one cell to the other in a given sample. Figure 5.2 shows doublet conformations, contact area, and bending energy for various $v_1 = v_2 = v$ and γ. The contact area A_c is normalized by the RBC area A. The bending energy E_b calculated directly from simulations and normalized by the bending energy $8\pi\kappa_c$ of a sphere,

$$\epsilon_b = \frac{E_b}{8\pi\kappa_c} \tag{5.4}$$

where ϵ_b denotes the reduced bending energy.

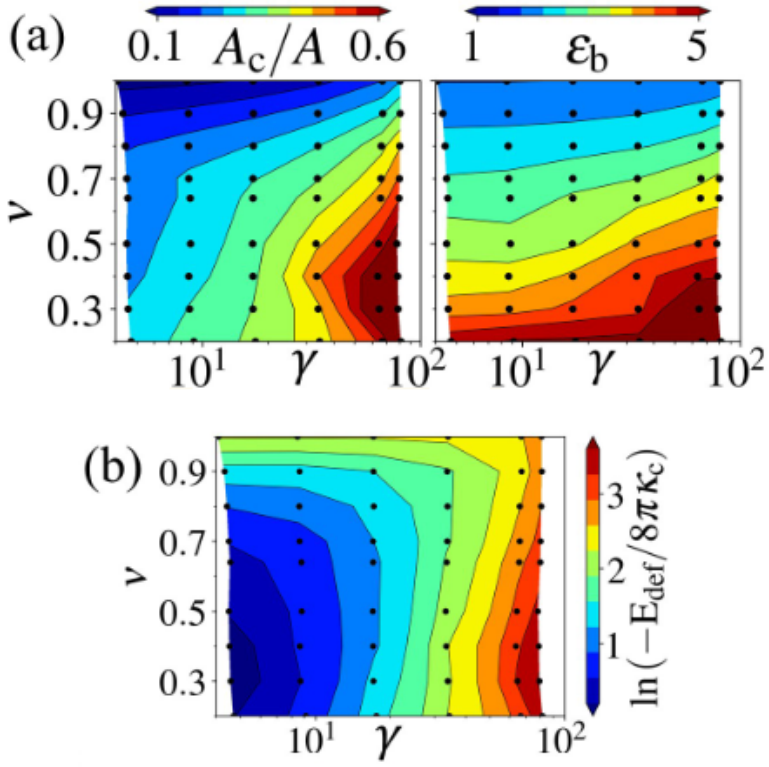

FIGURE 5.2: RBC doublet configurations as a function of $v_1 = v_2 = v$ and γ with aligned and offset first point of contact. (a) Contour plots for the contact area and the reduced bending energy for the aligned RBCs. (b) Contour plot for the difference between the free energy of the doublet and the free RBCs (deformation energy). The change in free energy is normalized by the bending energy of a vesicle with bending modulus κ_c, $8\pi\kappa_c$, and the colorbar has a logarithmic scale. The black dots (•) in contour plots represent the values for which simulations have been conducted. (Simulations by Masoud Hoore)

We observed that the shape of doublets heavily relies on the first point of contact between the two RBCs. The contact area is more sensitive to the reduced adhesion strength and bending energy is more sensitive to the reduced volume, see Fig. 5.2 (a). Overall, as the reduced volumes decrease and the adhesion strength increases, both contact area and membrane bending energy increase. The configurations both for the initially aligned and for offset doublets (Fig. 5.3 (a)) are depicted in Figs.5.3 (c) and (d).

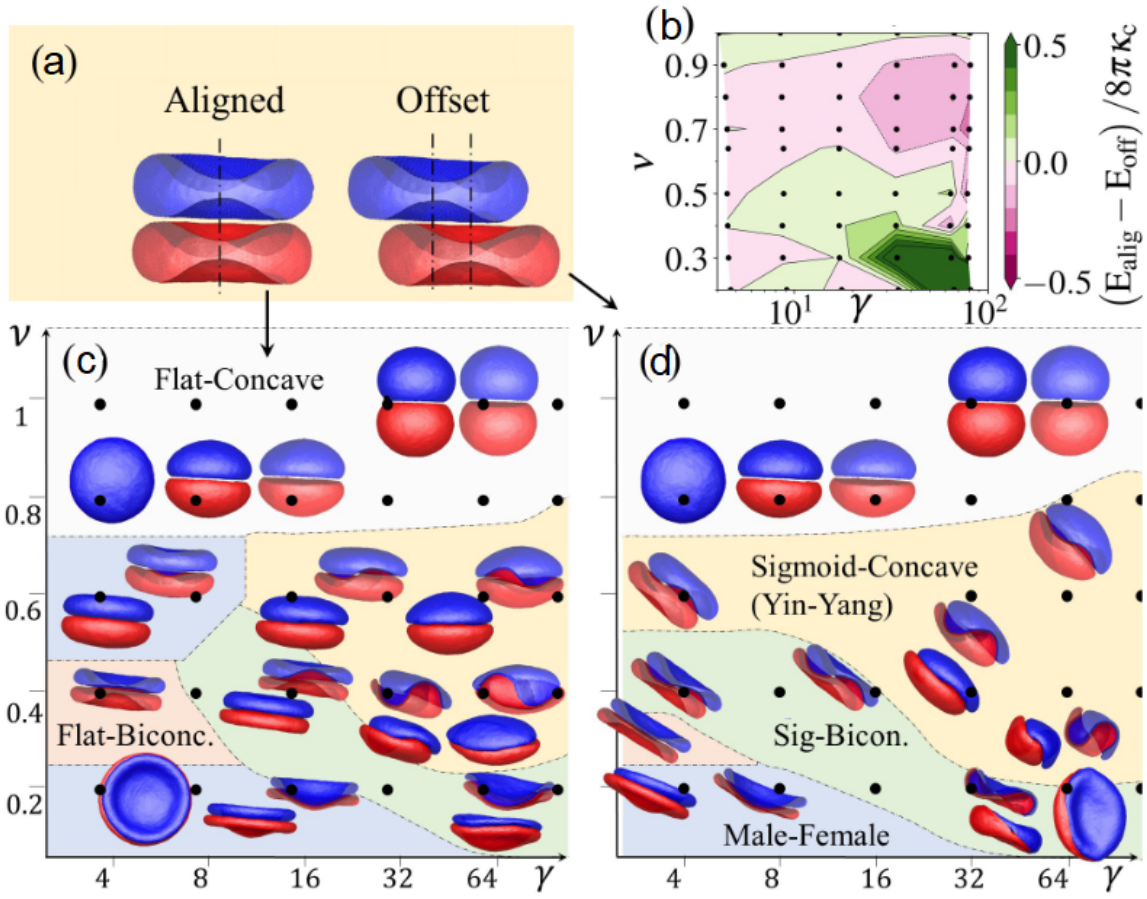

FIGURE 5.3: RBC doublet configurations as a function of $v_1 = v_2 = v$ and γ with aligned and offset first point of contact. (a) The configuration of a doublet depends on the way the RBCs make their first contact. RBCs can make the first contact while they are in aligned or offset configurations. (b) The difference between the free energy of the doublets in the aligned and offset cases. If $E_{alig} - E_{off}$ is positive, it means that the offset doublet has a smaller free energy, so that it is a more favorable configuration. The phase diagrams of the (c) aligned and (d) offset cases are different in the region, where $E_{alig} - E_{off}$ is positive. Various phases are distinguished by their cross-sectional views. The black dots (•) in the phase diagrams represent performed simulations. Note that the phase boundaries are drawn schematically to guide the eye. (Simulations by Masoud Hoore)

The phases of RBCs doublets for the initially aligned and offset configurations match at high adhesion strengths or high reduced volumes. However, a mismatch of doublet phases is observed for low adhesion strengths and low reduced volumes, see Fig. 5.3 (b), (c), and (d). This indicates the existence of several local minima in

the free-energy landscape, making the first point of contact important for RBC doublets. Multiple local minima in the free-energy should also exist for fluid vesicles, even though it has not been demonstrated so far. In comparison to vesicles, RBCs also possess an elastic spectrin network, which may have an anisotropic local prestress. This additional property likely contributes to a complex energetic landscape for RBC doublets with several metastable states or local minima. Various phases can be distinguished, as illustrated in Figs.5.3 (c) and (d). All observed shapes are categorized by their contact surface and their non-adhered free surfaces, as follows:

- **Flat-Biconcave (F-B) - pink zone:** This phase with a flat contact area and remaining concavities at the free surfaces is obtained for $v_1 = v_2 \approx 0.3 - 0.4$ and $\gamma \leq 8$ when the RBCs align with no offset. Figures 5.3 (c) and (d) show that the F-B phase shrinks to a very small region if the RBCs are initially in contact with an offset. Thus, the F-B phase is less probable to be seen under physiological conditions, where the offset contact is far more probable than the aligned contact.

- **Flat-Concave (F-C) - white zone:** If both RBCs are swollen, the M-F phase becomes unstable and both RBCs reconcile by making a flat contact surface and keeping their free surfaces near spherical. This phase appears at large reduced volumes.

- **Sigmoid-Concave (S-C) or better known as "Yin-Yang" - light red zone:** The RBCs make a sigmoid contact area, which is different from the native sigmoid (concave) shape of a RBC membrane. This condition occurs at high adhesion strengths, since the bending free energy of the RBCs increases substantially, but is compensated by the decrease in the adhesion energy. Since the cross-sectional view of the Sigmoid-Concave shape looks similar to the Yin-Yang symbol, we also call it Yin-Yang phase.

- **Male-Female (M-F) - blue zone:** Both RBCs attain a cup shape and plug into each other similar to the male and female terminals of a socket. The M-F phase provides the highest contact surface at the cost of bending energy, so that the total energy is minimized.

- **Sigmoid-Biconcave (S-B) - green zone:** This phase is located between the Yin-Yang and M-F phases. The RBCs are attached to each other in such a way that the concave part of one RBC fills the convex part of the other. In other words, the contact surface is sigmoid, while the free surface remains biconcave.

Although the F-B phase is the stable doublet configuration for the aligned doublets, the bending energy at this state is not at a global minimum. It can be seen from the free energy difference between the aligned and offset configurations in Fig. 5.3 (b). Under physiological conditions ($v \approx 0.64$), the M-F phase can be observed when the RBCs make the first contact in an aligned configuration, which is unlikely to be observed experimentally. Figure 5.5 illustrates various doublet shapes of two RBCs with different reduced volumes for a fixed reduced adhesion energy $\gamma = 8$. Another phase, the sheath phase, appears here.

Sheath phase: If the reduced volume of one RBC is large, and of the other is small, the former would swell to an elliptical shape and the latter would bend to a cup shape. Therefore, the best configuration for their adhesion occurs when the inner cup of the latter RBC matches the swollen curvature of the former RBC. This configuration corresponds to the minimal free energy condition for almost all adhesion strengths.

Since most RBCs have a reduced volume in the range 0.4 to 0.8, such phase does not occur under physiological conditions. In the case of unequal reduced volumes (see Fig. 5.4 and Fig. 5.5), the contact area is roughly proportional to the inverse of the average of the reduced volumes ($A_c/A \propto (v_1 + v_2)^{-1}$) and varies from about 0 to 0.7. The reduced bending energy $\epsilon_{b,1}$ of the first RBC decreases with increasing v_1, but is not very sensitive to a variation in the reduced volume v_2 of the second RBC. In order to study the effect of the spectrin network's shear elasticity on the doublet phases, the membrane shear modulus G is varied. High shear modulus G is relevant for diseased RBCs, such as in malaria.

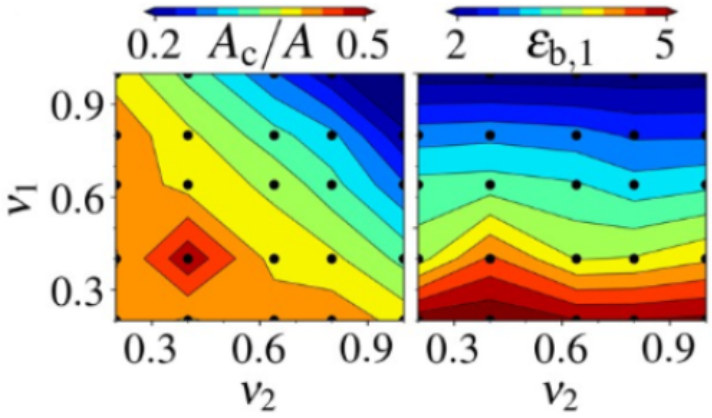

FIGURE 5.4: RBC doublet configurations as a function of v_1 and v_2 at a constant adhesion strength $\gamma = 8$. Contour plots show the contact area and the reduced bending energy of the first RBC as a function of v_1 and v_2. The black dots (•) represent the values for which simulations have been performed. (Simulations by Masoud Hoore)

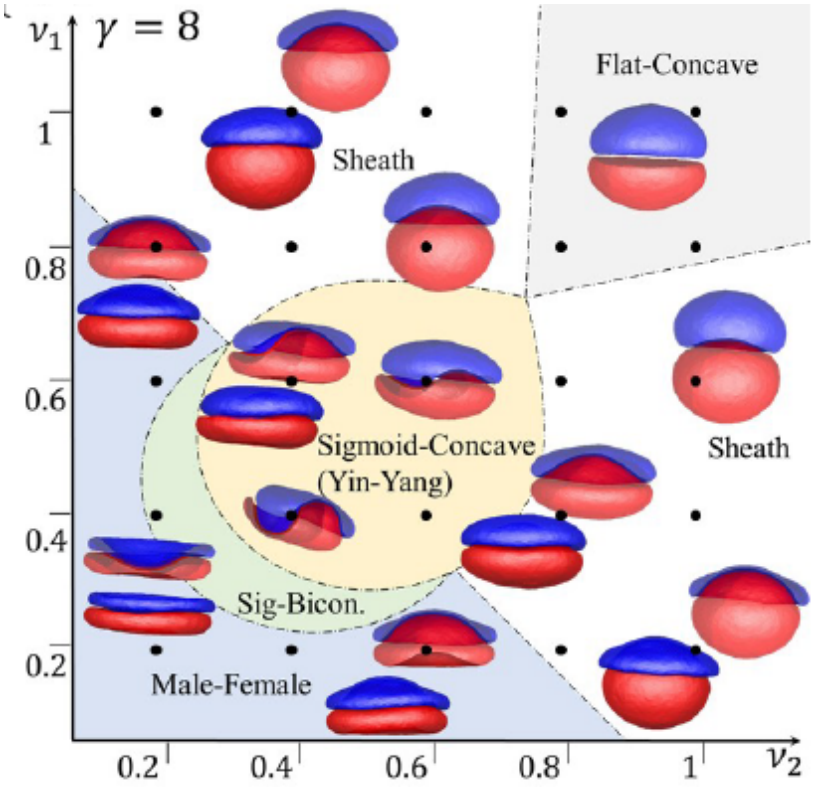

FIGURE 5.5: RBC doublet configurations as a function of v_1 andv_2 at a constant adhesion strength $\gamma = 8$. The side and section views of some configurations are shown in the phase diagram, omitting some shapes for more clarity. The different phases are separated by different colors. The S-B phase occurs in a narrow region between Yin-Yang and M-F phases. The membrane is assumed to be stress-free in its biconcave shape with $v = 0.64$. The phase boundaries are drawn schematically to guide the eye. (Simulations by Masoud Hoore)

Figure 5.6 (a) shows the phase diagram together with the contact area and reduced bending energy as a function of shear modulus and adhesion strength for a constant reduced volume of healthy RBCs $v \approx 0.64$. Fig. 5.7 displays the phase diagram of several RBCs doublets as a function of γ and μ. The shear modulus of healthy RBCs lies in the range $2 - 12\,\mu N/m$ [126, 127, 128, 120, 129, 130], which corresponds to the reduced shear modulus $\mu = GA/8\pi\kappa_c$ of 35-215, provided that the bending rigidity is $70\,k_BT$.

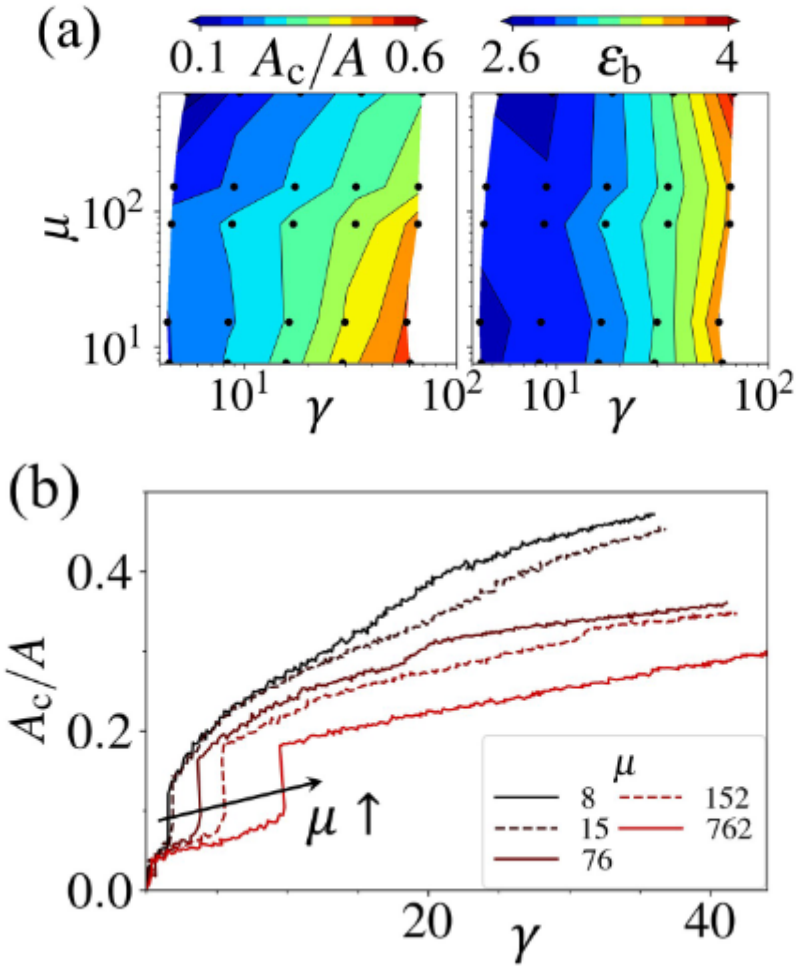

FIGURE 5.6: RBC doublet configurations as a function of spectrin network's reduced shear modulus $\mu = GA/8\pi\kappa_c$ and reduced adhesion strength γ at a constant reduced volume $v = 0.64$. (a) Contour plots show the contact area and the reduced bending energy. The black dots (•) represent the values for which simulations have been performed. (b) Dependence of the contact area on adhesion strength for different μ values. Discontinuity in the contact area is observed when one or both RBCs loose their original biconcave shape. (Simulations by Masoud Hoore)

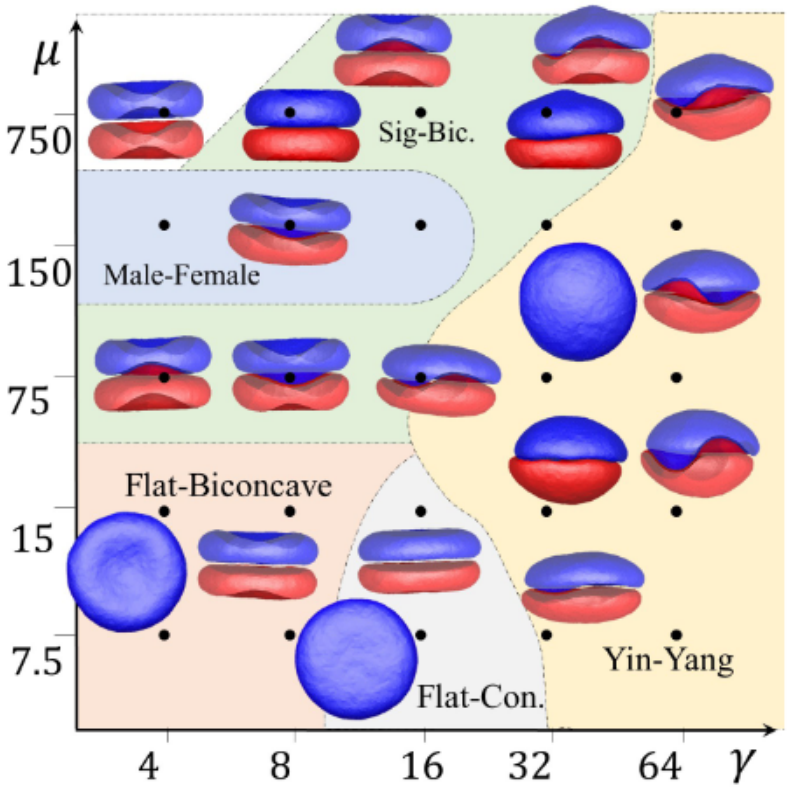

FIGURE 5.7: RBC doublet configurations as a function of spectrin network's reduced shear modulus $\mu = GA/8\pi\kappa_c$ and reduced adhesion strength γ at a constant reduced volume $v = 0.64$. Phase diagram of RBC doublets as a function of γ and μ, where different phases are separated by various colors. The phase boundaries are drawn schematically to guide the eye. The side and section views of some configurations are shown, omitting some shapes for more clarity. The low shear moduli approximate vesicle doublets. The membrane is assumed to be stress-free in its biconcave shape with $v = 0.64$ (Simulations by Masoud Hoore)

The phases obtained for very low shear moduli agree well with the numerical energy-minimization study for vesicles [118], where the contact area is flat for low adhesion strengths and it buckles as the adhesion strength increases. The F-B phase appears in a broader range of adhesion strengths when the shear modulus is much lower than that for a healthy RBC. Also, the F-C phase, which has never been detected for normal RBC reduced volumes of $v \approx 0.64$, appears at very low shear moduli. On the other hand, at shear moduli of healthy RBCs, the M-F and S-B phases are found at low adhesion strengths. If the shear modulus is very high, the RBCs do

not tend to form contact area from their center.

The doublet phases are determined by the balance of deformation energies and adhesion energy. The shear elasticity of the membrane attributed to the spectrin network has a strong effect on the doublet phases, as shown in Fig. 5.6 (a,b) and Fig. 5.7. For vesicle doublets, the effect of shear elasticity is absent since vesicles are made of fluid membrane. Accordingly, the lower region of the phase diagram ($\mu \to 0$) in Fig. 5.6 (a,b) and Fig. 5.7 corresponds to the previous works on doublets with the three phases F-C, F-B, and Sigmoid-Concave (Yin-Yang) [118, 119, 12, 120], characterized by the contact surface only. A distinct difference between our results and those from previous studies on vesicles is that the F-B phase appears only if the shear elasticity of the RBC spectrin network is small enough, as shown in Fig. 5.7. Therefore, such phase cannot be observed for RBC doublets, because they have significant shear elasticity.

Figure 5.6 (b) shows that by increasing the adhesion strength, the contact area exhibits two discontinuous jumps for a fixed μ. The first jump in A_c at very low $\gamma \leq 1$ occurs when the adhesion interaction overcomes membrane thermal fluctuations and cell diffusion. The second discontinuity in A_c manifests a transition when one or both RBCs loose their original biconcave shape by forming suddenly a larger contact area in a doublet. For example, it happens when F-B, S-B, and M-F shapes are first attained for $1 < \gamma < 10$, such that a larger contact area is rapidly formed. Interestingly, further transitions with increasing γ (e.g. to the Yin-Yang phase) are continuous, since the contact area is continuously gained with an increase in adhesion strength. Thus, buckling out of a membrane dimple and rapid formation of a larger area of contact can be considered as signatures of discontinuous transition. An increase in shear elasticity generally delays this discontinuous transition in terms of γ and reduces the contact area, as can be seen in Fig. 5.6 (b). These results are qualitatively consistent with a discontinuity in A_c found for vesicle doublets [118]. More generally, these differences in contact area should be taken into account, in experiments, for properly assessing the interaction energies.

5.4.1 Influence of the stress free shape

Since shear elasticity of membranes has a significant effect on the doublet configurations, the stress-free shape of RBC might also play an important role in determining the shape of the RBC membrane and their doublet phases. Whether the spectrin

network of a RBC is stress-free in the biconcave or spherical shape or something in-between is still under debate [46, 131, 132, 133]. So far in this work, the RBCs were stress-free at their biconcave shape.
In order to study the effect of the stress-free state of RBCs on doublet phases, the stress-free biconcave shape is compared with a case where the network is stress-free at a deflated sphere shape with eccentricity 0.94. The change in the configuration of the doublets is appreciable, as shown in Fig. 5.8 (b).

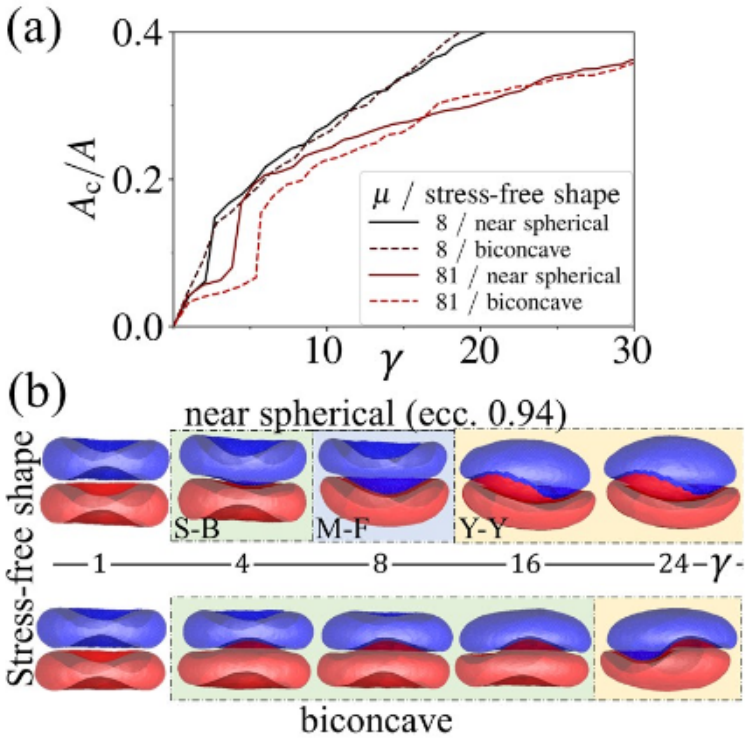

FIGURE 5.8: Effect of stress-free shape of RBCs on doublet phases for $v_1 = v_2 = 0.64$. (a) Contact area as a function of γ for biconcave and near spherical (with eccentricity 0.94) stress-free shapes. (b) The shapes of RBC doublets for $\mu = 81$, showing appreciable differences for the two stress-free shapes. The boundaries between different shapes are drawn schematically to guide the eye. (Simulations by Masoud Hoore)

The most important difference between the two cases is the change of the S-B phase to the M-F phase at small adhesion strengths. If the stress-free shape of RBCs is close to a sphere, the change to the Yin-Yang phase occurs at slightly lower adhesion strengths in comparison to the biconcave stress-free shape, as shown in Fig. 5.8 (b). In practice, this small change cannot be detected experimentally, not only because of the lack of the imaging precision, but also because of the natural variance

in the mechanical properties of RBC membranes and their reduced volumes [134]. As discussed above, the transition from original biconcave shape of both RBCs to a doublet shape with a large contact area (e.g. F-B, S-B, M-F shapes) is discontinuous in A_c for the biconcave stress-free shape, see Fig. 5.6 (b) and Fig. 5.8 (a). Fig. 5.8 (a) also demonstrates that this transition is discontinuous in A_c for the stress-free shape of 0.94.

Strong changes in RBC shapes (e.g. for a Yin-Yang doublet) likely lead to appreciable local in-plane deformations of the cell membranes. At the contact area, it is intuitive to expect that RBC membranes are compressed due to adhesive interactions, while the free surfaces are presumably subject to an area expansion. These modes of deformation are mainly controlled by the area-compression modulus of a membrane. The area-compression modulus in our model is equal to $2G + k_1 + k_a$, where G is the shear modulus and the other terms correspond to local and global area-conservation constraints. Here, $k_1 \approx G$, while $ka \gg G$ such that the local area constraint leads to a rather slight enhancement of the area-compression modulus. Therefore, under strong enough deformations local area of a membrane should experience appreciable deformation.

In order to elucidate local strains, local area changes, and the role of the local area constraint, we present in Fig. 5.9 a comparison of local membrane deformations for a Yin-Yang doublet ($\gamma \approx 85$ and $\mu = 80$) using a RBC model with and without the local area constraint. Fig. 5.9 (c) confirms that the membranes are compressed at the contact area and expanded at the free surfaces.This is also seen in the bimodal distributions of bond and local-area strains in Figs. 5.9 (a-b).

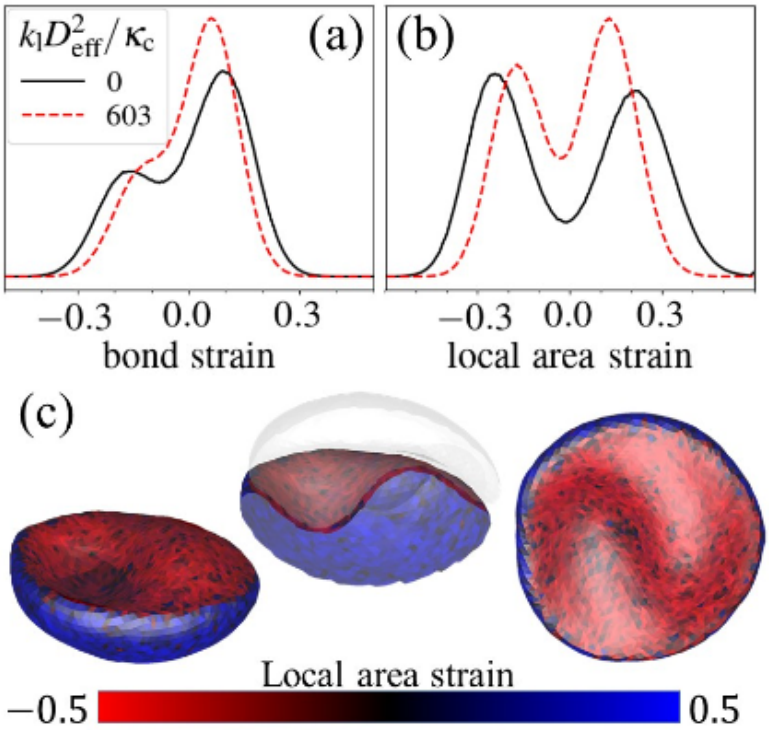

FIGURE 5.9: Effect of the local area constraint in the membrane model on a Yin-Yang doublet for $\gamma \approx 85$, $\mu = 80$, and $v_1 = v_2 = 0.64$. (a) Bond strain distributions from simulations with and without local area constraint. The bond strain is defined as $l/l_0 - 1$, where l is the length of a deformed bond and l_0 is its corresponding equilibrium length. (b) Distributions of local triangular area strains. The area strain is defined as $A/A_0 - 1$, where A is the area of a deformed triangle in the spring network and A_0 is its imposed area at biconcave equilibrium shape. (c) Distribution of local area strains on RBCs within a Yin-Yang doublet. The RBC membranes show a compressive deformation (or negative area strains) at the contact area and are stretched primarily at the free surfaces characterized by positive area strains. (Simulations by Masoud Hoore)

Here, the bimodality in the local area arises from the differences between adhered and free parts of the membrane. The bimodality in the bond lengths is related to the positive Poisson ratio of our elastic network model, which implies that stretching in one direction is accompanied by a compression in the orthogonal direction. The local strains remain approximately within the range of [-0.3,0.3] and their absolute values are slightly smaller for the case with the local area constraint in comparison to that without this constraint. However, in both cases Yin-Yang doublets are observed and their shapes are visually indistinguishable. Thus, for the employed

strength of the local area constraint, it plays at most a secondary role in determining doublet shapes for the range of adhesion strengths studied here.

5.4.2 Comparison with experiments

Doublet shapes

The experimental images of the different phases are compared to the simulation results in Fig. 5.10. The F-B phase is not observed in experiments and not predicted by simulations for the physiological reduced volumes of RBCs. Both in simulations and experiments, the M-F doublets form when the adhesion strength is intermediate and the reduced volume is small. The Yin-Yang phase appears when the adhesion strength is high. The S-B phase is seen as a transition state between these two phases. The F-B phase has not been observed in experiments. The F-C phase occurs when both RBCs are swollen and the Sheath phase happens when there is a significant difference in the reduced volumes of the two RBCs. To see the F-C phase in experiments, the osmolality of the solution has to increase about two-fold. For increasing reduced volume of RBCs in experiments, they were immersed in hypotonic solution of NaCl. At low shear rates, RBCs aggregate in stacks known as rouleaux.

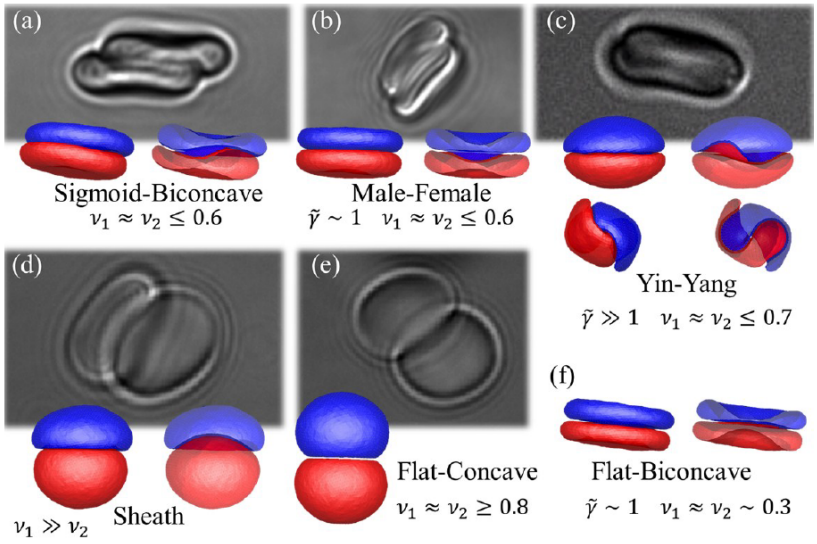

FIGURE 5.10: Comparison of experimental and simulated RBC doublet shapes determined by the adhesion strength, bending modulus, and the reduced volume of RBCs. For simulations, the side and section views are presented for each case. The phases (a) sigmoid–biconcave, (b) male–female, (c) sigmoid–concave (Yin–Yang), (d) sheath, (e) flat–concave, and (f) flat–biconcave are shown. (a) was observed in dextran (70kDa) - 20mg/ml, (b) in Dextran (40kDa) - 10 mg/ml, (c) in plasma + fibrinogen at 6mg/ml, (d) and (e) both in a hypotonic solution of dextran (70kDa) at 20mg/ml and (500kDa) at 10mg/ml

Rouleaux formation

The rouleaux increase substantially the viscosity of blood at low shear rates [135, 136, 137]. The nucleation of rouleaux starts from RBC doublets. While some doublet structures allow for large rouleaux formation, others prevent the formation of large rouleaux. Among all the doublet phases, the M-F and S-B phases let the RBCs to form large rouleaux with a straight (linear) structure. However, the Yin-Yang phase prevents long straight structures to appear. Thus, the size of rouleaux in a solution of RBCs depends on their adhesion strength which is determined by the concentration of different adhesive factors in the solution (e.g.dextran, fibrinogen). Figure 5.11 shows several experimental and simulated results of different rouleau structures. The shapes of rouleaux for high adhesive strengths are very different, depending on the reduced volumes of the RBCs and the number of RBCs in the rouleau. In contrast, the M-F and S-B phases should allow the size of straight rouleau structures to increase with no limit. Note that at high enough adhesive strengths, more complex

RBC aggregate structures, other than straight rouleaux, may appear[138].

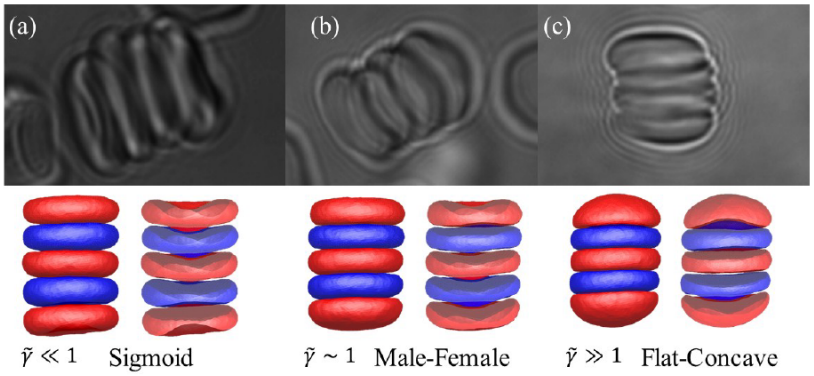

FIGURE 5.11: Various rouleau shapes in experiments and simulations with different nucleation doublets: (a) sigmoid (b) Male-Female and (c) Flat-concave. (a) was observed in dextran (70kDa) at 20 mg/ml, (b) in dextran 40 kDa at 10 mg/ml and (c) in dextran (500kDa) at 10 mg/ml

The limit for the rouleau nucleation can be explained by the free energy of the whole system. Doublet formation changes the free energy of the system by $2E_{def} - \Gamma A_c$. E_{def} is the deformation energy of a RBC, mostly due to bending rigidity and shear elasticity. In principle, it is always positive since any deviation from the equilibrium biconcave shape of a RBC must have a higher energy. Therefore, the adhesion energy ΓA_c must be larger than $2E_{def}$ for doublet formation to be favorable. Addition of one more RBC to the doublet to make a triplet aggregate of RBCs increases the total free energy by $\Delta E_+ = E_{def} - \Gamma A_c + E^0_{def}$, where E^0_{def} is the additional deformation energy of the original aggregate, E_{def} is the deformation energy of the newly added RBC to the original aggregate and $-\Gamma A_c$ is the adhesion energy due to it. Assuming that the other RBCs in the aggregate do not deform substantially leads to $E^0_{def} \approx 0$; otherwise, the deformation and adhesion energy of all RBCs must be considered in the rearranged configuration. This rearranged configuration has definitely a higher energy for the RBCs already in the aggregate, since they get away from their equilibrium configuration. For S-B and M-F phases, addition of a RBC to the aggregate adds a constant negative ΔE_+ to the free energy so that the growth of the rouleau is energetically favorable. ΔE_+ is nearly constant since the contact area and curvature of the newly added RBC is similar to the other RBCs in the aggregate.On the contrary, ΔE_+ grows as a new RBC is added to a Yin-Yang doublet, because the contact area for the new RBC is less than the contact area of a doublet, and the new RBC deforms much more in order to fit to the concave shape of

a rouleau. As a result, ΔE_+ becomes positive at some point preventing more RBCs to adhere to the aggregate. This limiting point occurs for larger cluster sizes as the adhesion strength Γ increases.

5.5 Conclusions

The work presented here aimed to complement 3D simulations performed by M. Hoore (FZ-Jülich). A whole phase diagram has been established for 3 dimensional doublets by varying parameters such as: reduced volume, bending rigidity and shear elasticity. The simulation results demonstrate various doublet phases that could be found experimentally by varying the osmolality and concentration of the aggregating agent. The RBCs doublet phases are mainly defined by the interplay of bending energy and adhesion energy, and are closely related to the reduced volume of RBCs. However, the shear elasticity of the RBC membranes, due to the spectrin network beneath their lipid bilayers is a key player and affects their doublet phases. This work shows that rouleau nucleation depends on how RBCs make doublets first. Both experiments and simulations report that the Male-Female and Sigmoid-Biconcave doublet are the most favorable for the nucleation into larger rouleaux. These results suggest that variations in RBCs mechanical properties (e.g. due to specific pathologies) may significantly alter their ability to aggregate into large structures or at least change the morphology of these structures and the associated blood rheology.

Résumé

Le travail présenté ici vise à compléter les simulations 3D réalisées par M. Hoore (FZ-Jülich). Un diagramme de phase complet a été établi pour des doublets tridimensionnels en faisant varier des paramètres tels que : volume réduit, rigidité à la flexion et élasticité au cisaillement. Les résultats de la simulation montrent différentes phases de doublets qui ont pu être trouvées expérimentalement en faisant varier l'osmolalité et la concentration de l'agent d'agrégation. Les phases de doublets sont principalement définies par l'interaction de l'énergie de flexion et de l'énergie d'adhésion, et sont étroitement liées au volume réduit des globules rouges. Cependant, l'élasticité de cisaillement des membranes des GRs, due au réseau de spectrines sous leurs bicouches lipidiques, est un acteur clé et affecte leurs phases en doublet. Ce travail montre que la nucléation des rouleaux dépend de la façon dont les GRs forment initialement les doublets. Les expériences et les simulations

indiquent que les doublets "mâle-femelle" et le doublet "sigmoïde-biconcave" sont les plus favorables à la nucléation pour former de plus grands rouleaux. Ces résultats suggèrent que les variations des propriétés mécaniques des globules rouges (dues par exemple à des pathologies spécifiques) peuvent modifier de manière significative leur capacité à s'agréger en plus grandes structures ou du moins, changer de la morphologie de ces structures et la rhéologie sanguine associée.

Zusammenfassung

Die hier vorgestellten Arbeiten zielten darauf ab, die von M. Hoore (FZ-Jülich) durchgeführten 3D-Simulationen zu ergänzen. Es wurde ein vollständiges Phasendiagramm für 3-dimensionale Dubletten erstellt, indem Parameter wie: reduziertes Volumen, Biegesteifigkeit und Scherelastizität variiert wurden. Die Simulationsergebnisse zeigen verschiedene Dublettenphasen, die experimentell durch Variation der Osmolalität und der Konzentration des aggregierenden Agens gefunden werden konnten. Die RB-Dublettenphasen werden hauptsächlich durch das Zusammenspiel von Biege- und Adhäsionsenergie definiert und stehen in enger Beziehung zum reduzierten Volumen der RB. Die Scherelastizität der RB-Membranen aufgrund des Spektrinnetzwerks unter ihren Lipiddoppelschichten ist jedoch ein Schlüsselfaktor und beeinflusst ihre Dublettenphasen. Diese Arbeit zeigt, dass die Rouleau-Keimbildung davon abhängt, wie die Erythrozyten zuerst Dubletten bilden. Sowohl aus Experimenten als auch aus Simulationen geht hervor, dass das männlich-weibliche und das sigmoid-bikonkave Dublett am günstigsten für die Nukleation zu größeren Rouleaux ist. Diese Ergebnisse deuten darauf hin, dass Variationen in den mechanischen Eigenschaften der Erythrozyten (z.B. aufgrund spezifischer Pathologien) ihre Fähigkeit, zu großen Strukturen zu aggregieren, signifikant vermindern können oder zumindest die Morphologie dieser Strukturen und die damit verbundene Blutrheologie verändern können.

Chapter 6

Vortical flows induced by red blood cells

Whereas previous parts of this thesis are dedicated to the study of RBC aggregation in stasis, this chapter is dedicated to the observation of RBC in flow. This study has already been submitted [139] and aims to characterize the flow around a single RBC but also around two neighboring RBC. We focused on two prominent shapes: slippers and croissants. The flow field around a hydrodynamic cluster of two croissant shapes has also been investigated. Computer simulations have indicated the presence of vortex-like structures between neighboring RBCs [36, 140] but experiments about this peculiar event were incomplete and very rare [44]. Here, we present a direct experimental observation of (i) the flow around isolated RBCs and (ii) the vortical flow between clustering RBCs in a rectangular microchannel complemented by 3D simulations carried out by A.Guckenberger, J. Roemer and S.Gekle (from the university of Bayreuth). We find that the rotation frequency of the vortices is to a good approximation inversely proportional to the distance between the cells.

6.1 Introduction

Besides its physiological relevance, blood flow in microcapillaries is a prime example of a biological fluid-structure interaction problem between the elastic red blood cells on the one hand and the hydrodynamic flow of plasma on the other [141, 142, 143]. Over recent years, quite some attention has been paid to the dynamics of RBCs in cylindrical or rectangular channels known to be the most common configuration in model microfluidic flows. Depending on external parameters such as flow speed, channel size and plasma viscosity two main shapes have emerged from these experimental [144, 44, 145, 146, 42, 43] as well as numerical [147, 148, 149, 150, 41, 151, 152, 43, 153, 154] works. The first, called slipper, is an elongated, non-asymmetric shape

in which the RBC tends to flow at a steady position slightly away from the channel center. The second one, almost axi-symmetric in cylindrical capillaries and with two planes of symmetry in rectangular channels, is termed "parachute" in cylindrical tubes or "croissant" in rectangular cross-sections and flows in the channel center. In addition, some works observed clusters of two or more RBCs formed and held together by hydrodynamic interactions [155, 156, 157, 158, 125, 45, 159, 140].
While there is good agreement between numerical simulations and experiments regarding the actual shape of RBCs, less attention has been paid to resolve the flow field of the surrounding plasma experimentally. While in the absence of RBCs, this would be a simple parabolic Poiseuille profile, the presence of RBCs strongly disturbs the flow. [160]
Understanding the actual flow pattern is however essential, e.g., for the distribution of nanometric drug delivery agents or dissolved substances in microcapillary blood flow [161, 162, 163, 140, 164, 165, 166, 167] as well as to understand the nature of interactions between cells. While there is quite some literature on the flow field in microchannels around rigid or only slightly deformable objects such as microspheres or droplets [168, 169, 170, 171], experimental data are rare for the complex flows arising due to the above described croissant and slipper motions of red blood cells. In RBCs clusters, computer simulations have indicated the presence of vortex-like structures between neighboring RBCs [155, 156, 158, 140].
Here, we present a direct experimental observation of (i) the flow around isolated RBCs and (ii) the vortical flow between clustering RBCs in a rectangular microchannel using particle tracking. We find that the rotation frequency of the vortices scales inversely proportional to the RBC distance. Our particle tracking measurements are in good agreement with corresponding boundary-integral simulations.

6.2 Methods

6.2.1 Experiments

To mimic blood capillaries, we use rectangular straight channels of 12 µm width, 10 µm depth and about 40 mm in length as microfluidic chips. The camera is positioned such that the long (12 µm) side is viewed in the images. Channels are made from Polydimethylsiloxane (PDMS) [172]. To avoid RBCs adhering onto the walls, the channels are flushed with a buffer solution containing BSA at 1%. The flow of the suspension is observed in a microscope with an oil-immersion objective (Nikon CFI Plan Fluor 60x, NA = 1.25). The field of observation is at 1 cm behind the pressure

inlet. We use a high speed camera (HiSpec Fastec 2G) to record image sequences at frame rates of 9000 fps. We investigate the flow at cell speeds at the physiologically relevant parameter range and beyond from 1 mm/s up to 10 mm/s. The various flow and cell speeds are achieved with a pressure controller (ELVEFLOW OB1+) at pressure drops ranging from 100 mbar to 1000 mbar, respectively [43].

To visualize the flow field around the moving RBC, we add nanoparticles with surface coating of polyethylene glycol (PEG) and 250 nm in diameter (Micromod) in an aqueous solution containing 0.1% of Bovine Serum Albumine (BSA). Blood is drawn from healthy donors after giving an informed consent in compliance with the ethical requirements of the Saarland University, Saarbrücken, Germany (Ärztekammer des Saarlandes, approval number 24/12). We use a suspension of washed RBCs in Phosphate Buffered Saline (PBS) at 0.5% hematocrit with nanoparticles as tracers. Samples are regularly mixed to prevent the sedimentation of RBCs.

The shape and speed of individual cells depend on the applied pressure drop and remains stationary within the time of observation in our experiments. We observe two main steady cell shapes in our rectangular channel geometries, croissants at rather low flow speeds and slippers at higher flow speeds, see Fig. 6.1. We determine the speed of the RBCs from the recorded image sequence over a distance of 100 µm. The trajectories of the tracers are determined with a self-made MATLAB © program in the co-moving frame of the individual RBC. Figures 6.1 (a) and 6.1 (b) show exemplary trajectories as overlayed images of snapshots of a flowing RBC for two different velocities. The motion of tracers between two RBC are studied in a similar manner. During the observation time span, the distance d_{RBC} between two consecutive RBCs never changes more than 10% in our experiments, i.e. both cells have comparable velocities.

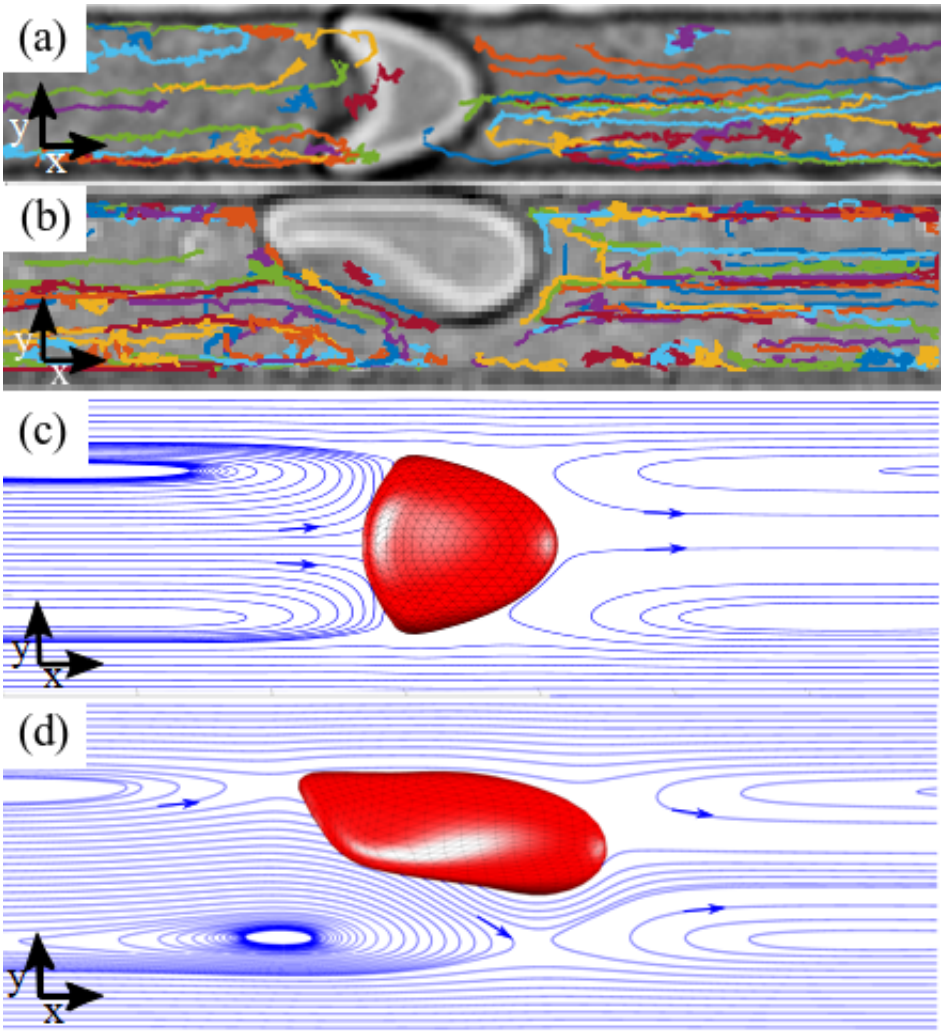

FIGURE 6.1: Snaphots of RBCs in (a) croissant and (b) slipper shape, together with an overlay of experimental recorded trajectories of tracers. (c) and (d) represent the stream lines and cell shapes from the numerical simulations. The speed in (a) and (c) is $v_{RBC} = 2.83$ mm/s and in (b) and (d) $v_{RBC} = 6.50$ mm/s. Particles trajectories and streamlines are shown in the co-moving frame of the RBCs. The fluid flows from left to right. Simulations by A. Guckenberger and J. Roemer

6.2.2 3D Simulations

Simulations were performed by the group of Stephan Gekle and his two doctoral students Achim Guckenberger and Johannes Roemer using 3D boundary integral (BI) simulations to solve the Stokes equations for the fluid inside and outside the red blood cell [173, 174, 43]. This is justified by the small Reynolds number of around 0.1.

A specific advantage of BI simulations is that the full instantaneous flow field at anytime can be computed knowing only the parabolic background flow and the forces on the cylinder wall and the RBC membrane [173, 174]. A time integration is not necessary to compute the flow field. In our model, the membrane forces are computed following the models by Skalak and Helfrich for shear, area and bending elasticity, respectively [175, 176, 142]. The no-slip boundary condition as well as continuity of stresses is imposed at the membrane. Periodic boundary conditions along the channel are used with a computation window length of 42 µm. This length is sufficient to recover a nearly undisturbed Poiseuille flow far away from the cell.

For the velocity field computation, a snapshot of the simulation is selected and the shape of the RBC at this time is frozen. Then, the velocity field is computed on a regular grid in the central plane and transformed to the frame of reference of the moving RBC using its center-of-mass velocity. As the slipper exhibits periodic oscillation through a series of slightly varying shapes, an arbitrary shape out of these is selected for computing the stream lines following the procedure described above. In an ideal situation, the mirror symmetry of the system around the central plane would forbid the existence of out-of-plane currents. Due to rounding and discretization errors, nevertheless small spurious out-of-plane currents may arise which however we set to zero here.
The simulations are performed in the same channel geometry as the experiments. Figures 6.1 (c) and 6.1 (d) show the converged 3D RBC shapes and corresponding stream lines in the channel middle plane for a croissant and a slipper, respectively.
To compute the stream lines between two cells in a cluster, we select a converged croissant shape from the simulation with a single RBC at the corresponding speed. This shape is then copied and both cells are placed into the channel. After a short time span of typically 70 ms, the stream lines are computed starting at a vertical line between the two cells. The above procedure had to be chosen because in the experiments many different distances between two cells for a given flow speed can be observed which means that the clusters are not yet at their converged distance. The reference frame is the center-of-mass velocity of the left RBC.

Stream lines contain only directional information but no absolute velocities which are needed to compute the rotation period of particles trapped in flow vortices. To obtain this information, we place virtual tracer particles (again starting from a line of seed points) and integrate their trajectory in time given the flow field extracted from BIM simulations (which is assumed to be stationary). This procedure allows us

to obtain not only the particle trajectories, but also temporal information such as rotation periods. In addition, Fig. 6.5 shows particle trajectories integrated backward in time in order to demonstrate the possibility of particle escape from the central vortices in non-perfectly symmetric situations.

6.3 Results

6.3.1 Flow field in the vicinity of a single RBC

Fig. 6.1 shows the experimental and numerical results of our flow field measurements around the two characteristic cell shapes. Far away from the cell, the velocity profile in the rectangular channel is almost parabolic [177]. The speed of the RBCs is approximately the mean velocity of the free liquid flow in the channel because the volume flux is conserved. The cell speed defines for the co-moving frame and is always lower than the fluid velocity in the middle of the channel far away from the cell. At low flow speeds, the observed cell shape is in the symmetric croissant shape Fig. 6.1 (a) and 6.1 (c) [43] and tracers in the middle of the channel in front of the cell move away from the cell, while behind the cell they move towards it as shown in Fig. 6.2 (a).

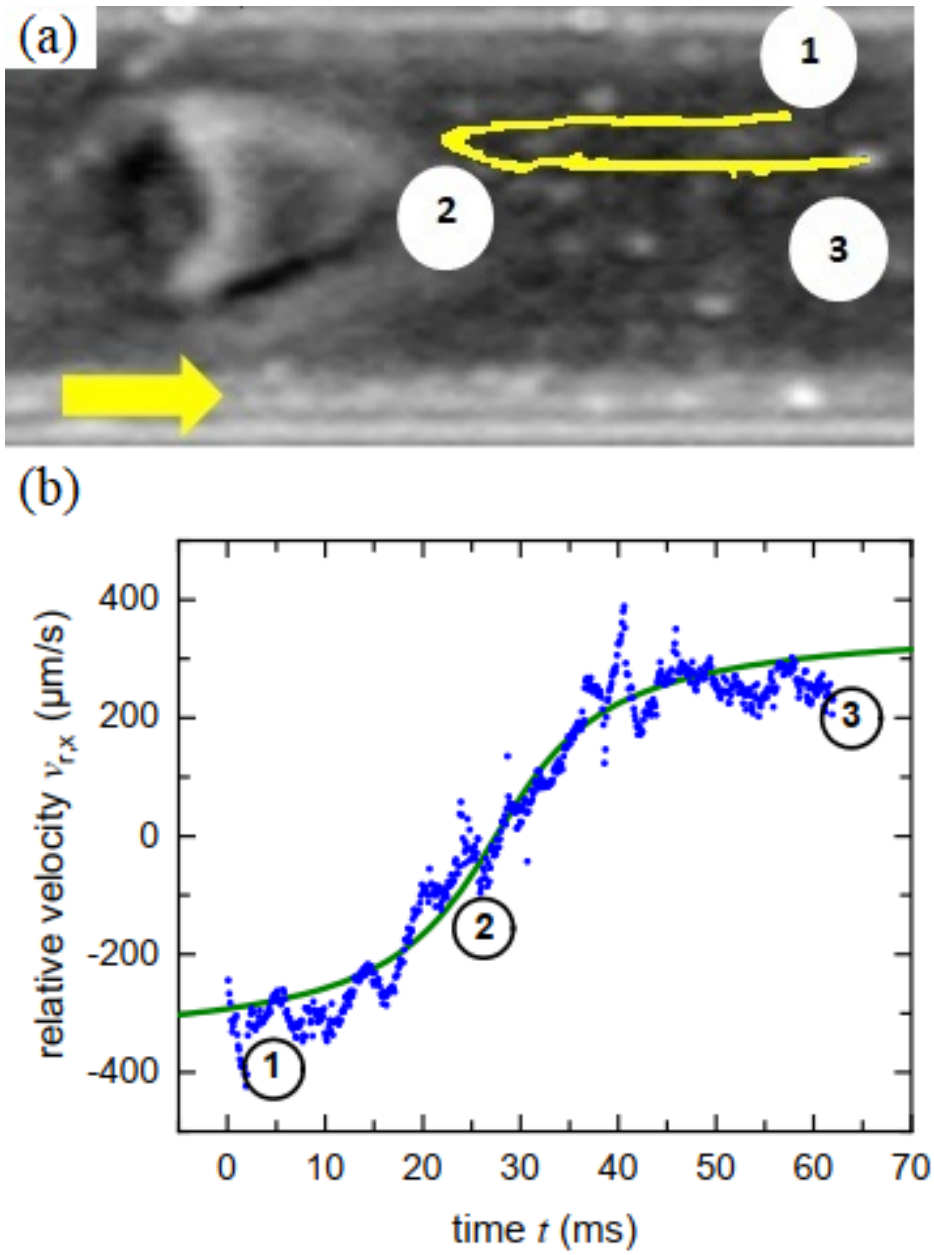

FIGURE 6.2: Motion of tracers in the co-moving frame of a RBC in croissant shape flowing with a speed $v_{RBC} = 4.3 \pm 0.1$ mm/s. (a) Snapshot of the RBC with an overlay of a tracer trajectory from the image sequence. (b) The velocity $v_{r,x}$ in flow direction of the tracer when it approaches and moves away from the cell. The fit curve is an empirical sigmoid function. The flow direction of the cell is indicated by a yellow arrow in and the path of motion is indicated by numbers.

In the co-moving frame the flow velocity is zero at the cell surface and there is a stagnation point on the cell surface on the centre line. Closer to the walls, this flows

direction is reversed. The combination of those motions lead to a strongly elongated half ellipse for the trajectory of a single tracer. From the experimental particle tracking velocimetry (PTV) of the tracers we can also deduce the relative velocity in the co-moving frame $\vec{v}_r$. The component in flow direction $v_{r,x}$ is shown as function of time Fig. 6.2 (b). The velocity can be fitted with a heuristic sigmoidal function. Obviously, tracers decelerate when approaching the cell and accelerate to the faster fluid motion in the middle of the channel when they move away again from the cell. We should mention that with our microscopic setup in the experiment we image the full sample height and therefore the observed position of tracers is always their projection in the x-y plane. Therefore we also observe trajectories that approach and depart from the cell in the y = 0 plane (Fig. 6.1 (a)). This is especially the case when the tracer's motion is in the orthogonal plane with respect to the plane of projection.

At higher flow speeds, the cells attain a slipper shape [43]. In this asymmetric configuration, a vortical flow can be observed behind the cell (see Fig. 6.1 (b)) even though the flow remains laminar. The slipper shape and the existence of the vortices are confirmed by our numerical simulations (Fig. 6.1 (d)). However, a fully closed vortex flow in the middle plane of the channel as predicted from the numerical simulations, could not be seen in the experimental situation where small irregularities are enough to displace tracer particles out of the vortex zone in the channel. In both cases, for croissants as well as for slippers, the presence of RBCs reduce the spatial variations in fluid velocities over the channel width to an almost plug like flow and therefore the spreading of suspended tracers in flow direction over the channel is also reduced. This becomes even more pronounced for clusters of two RBCs as we will see in the following.

6.3.2 Flow field in the vicinity of a cluster of two RBCs

At low hematocrit levels, the mean distance between consecutive RBCs in the channel is typically very large compared to the cell size and the channel width. If two cells come close to each other, however, they can form a stable cluster due to their hydrodynamic interaction [156, 157, 158, 125, 45, 140]. A significant amount of the liquid between the cells seems to be "encapsulated" and does not mix anymore with the liquid outside of the cluster. Similar to the tracer trajectories of single cells, we observe hairpin loops and vortices for tracers moving in the plane of observation and straight lines for tracers moving orthogonal to it (Fig. 6.3 (a)), as consequence of our optical projection. Our numerical simulations confirm that the stream lines corresponds to toroidal vortex, just as smoke rings, with the axis of symmetry along

the channel x-direction, see Fig. 6.3 (b). In the co-moving frame, the channel borders move with the speed of the RBC cluster in -x-direction. This relative border motion drives the rotation of the liquid between the cells, similar to the case of a lid driven cavity flow [178]. Accordingly, the liquid in the inner part of the channel moves in the +x-direction with a speed that is somewhat higher than the speed of the cells in the laboratory frame.

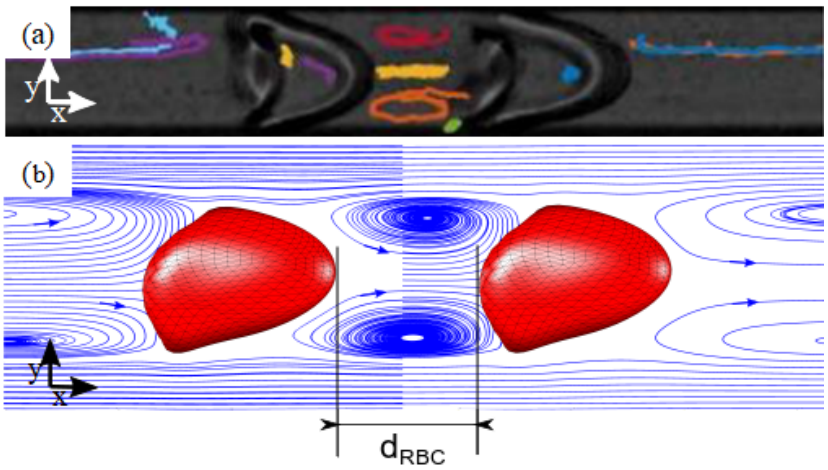

FIGURE 6.3: (a) Snapshot of a cluster of two RBCs in croissant shape with a distance of d_{RBC} = 5.2 µm together with an overlay of tracer trajectories. The liquid between the cells seems to be encapsulated in a vortex and to rotate as a torus with the axis of symmetry in x-direction. (b) Numerical simulation of a cluster. The streamlines indicate how tracers will be transported from the middle along a helical trajectories (see Fig. 6.6). Simulations by A. Guckenberger and J. Roemer.

At steady state, the distance d_{RBC} between two RBCs in a cluster is constant and depends on the flow velocity. However, in the experiments many distortions can disturb the equilibrium distance positions and different distances can be observed for the same flow condition. To mimic this situation in the simulations, we place two cells with the approximated shape at desired distance in the channel and determine the flow field after a short time span of typically 70 ms. Here, we analyze only the flow field of clusters of two croissant shaped cells. To characterize the torus movement of the tracers more quantitatively we consider the period T for one cycle. This means that the vortex forms a deformed torus in 3D and that the flow becomes faster with increasing distance from the central axis of revolution. Fig. 6.4 shows the period T as a function of the distance between the two cells, d_{RBC}. The period increases almost linearly with the distance, both for the simulated and for the experimental results. In other words, in first approximation, the tracers move along the

circumference $\mathcal{C}$ of ellipses. Assuming a constant tracer speed v_t along a particular ellipse circumference the period $T(d_{RBC})$ is given by the ratio of $\mathcal{C}$ and v_t. Within concentric ellipses and with decreasing sizes, the velocity vt decreases as well. The extension of the largest ellipse is given by an almost constant semi-minor axis a in order of a quarter of the channel width and a major axis d_{RBC} of the interior distance between two cells. Using a truncated series expansion for the circumference $\mathcal{C}$ of the largest ellipse, the estimated period $T(d_{RBC})$ is given by:

$$T(d_{\mathrm{RBC}}) = \frac{\mathcal{C}}{v_{\mathrm{t}}} = \frac{\pi}{v_{\mathrm{t}}}\left(a + \frac{d_{\mathrm{RBC}}}{2}\right)\left(1 + \frac{\theta^2}{4}\right). \tag{6.1}$$

with $\theta = (a - d_{\mathrm{RBC}}/2)/(a + d_{\mathrm{RBC}}/2)$

This relationship is confirmed by both experiments and simulations. In fact, both show that tracer velocities vt in the comoving frame happen to be lower than the velocity of a cell vRBC in the laboratory frame. However, there are some quantitative differences which we attribute to the fact that the cells at various distances are not in their equilibrium situation. We use this dependency to extract the fluid and tracer speed v_t at the surface of the toroidal vortex, vt. We show in Fig. 6.4 the extracted periods as function of the distance between two RBC flowing at different speeds. As expected, an offset can be observed due to the fact that the semi-minor axis a is considered constant. We found in simulations that proper vortices were rarely formed for $d_{RBC} > 40\mu m$. In this case, a tracer escapes the vortex before doing a full revolution. For distances shorter than $5\mu m$, no vortex could be observed in experiments. This is in agreement with simulations [156] who define the "vortex existence" boundary to be $1.4R_0$ with R_0 being the effective radius of a RBC.

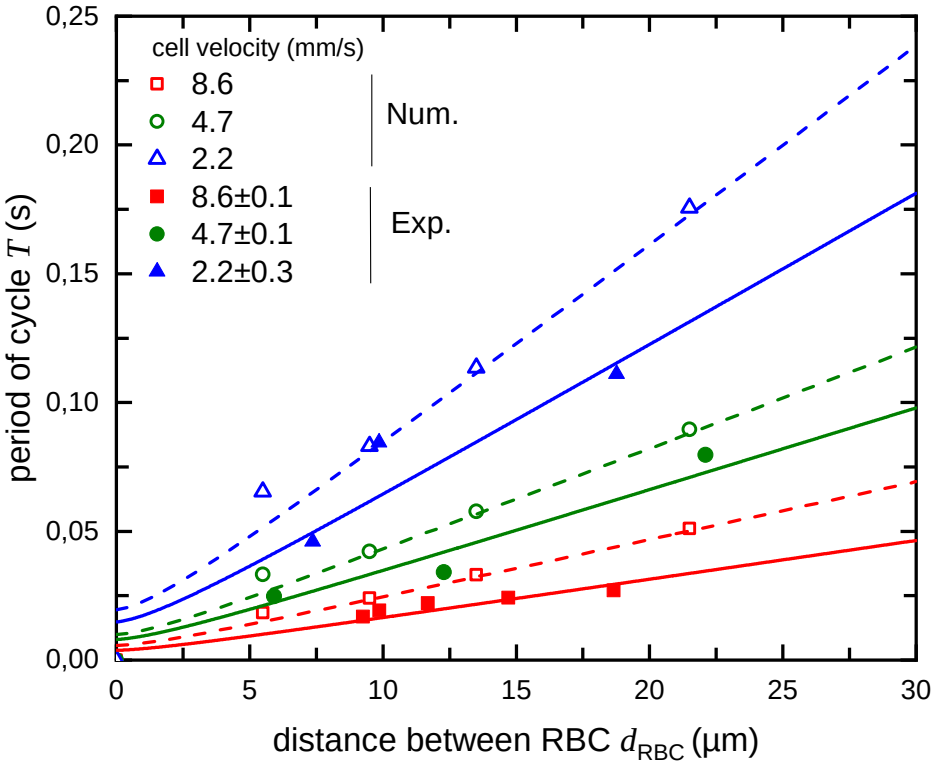

FIGURE 6.4: Period of cycles for a toroidal tracer motion between two RBCs as a function of the distance between the cells. Experimental data are represented by solid symbols and lines and numerical results by open symbols and dashed lines respectively. The fit represents a motion on an axial stretched torus with ellipses of revolution. It is based on equation 6.1 with π/v_t as a fitting parameter and the minor axis is fixed to be $a = 3\,\mu m$.

6.3.3 Particle escaping pathways around RBC

Given the vortex-like structures between two clustering RBCs, one may expect that these vortices should be able to actually capture small particles and trap them between the cells similar to earlier observations for microparticles [140]. In figure 6.5 we illustrate such events, i.e., the pathways by which particles can enter into the vortices from the main flow.

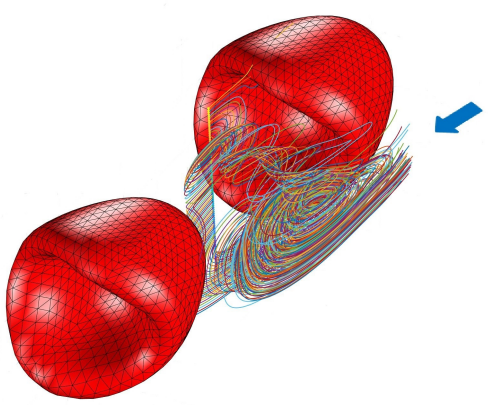

FIGURE 6.5: 3D view showing the provenance (blue arrow) of the tracers and their trajectories for a cell velocity of 2.2 mm/s. Simulations by A. Guckenberger and J. Roemer

For this, a line of tracer particles has been seeded into the central region between the two RBCs and their trajectories integrated backward in time. Thus, the colored lines illustrate the entry of tracer particles into the vortices.

As can be seen in the stream lines (Fig. 6.3), the vortices between two flowing RBCs typically are not fully closed. One can therefore expect that tracer particles should, depending on their starting position, also be able to escape from these vortices back into the main flow. Indeed, we do observe such trajectories as illustrated in Fig. 6.6. Note that, in particular for the experiments the period T is not affected by the projective view. For a fixed distance between the cells d_{RBC}, we find that the period T remains constant, independent of the amplitude in x-direction. This result is supported by numerical simulations (see Fig. 6.6). Here, a particle first performs a spiralling motion between the two RBCs but eventually escapes from the region between the two RBCs. Due to the short observation time, we were unfortunately not able to observe such trajectories directly in the experiment.

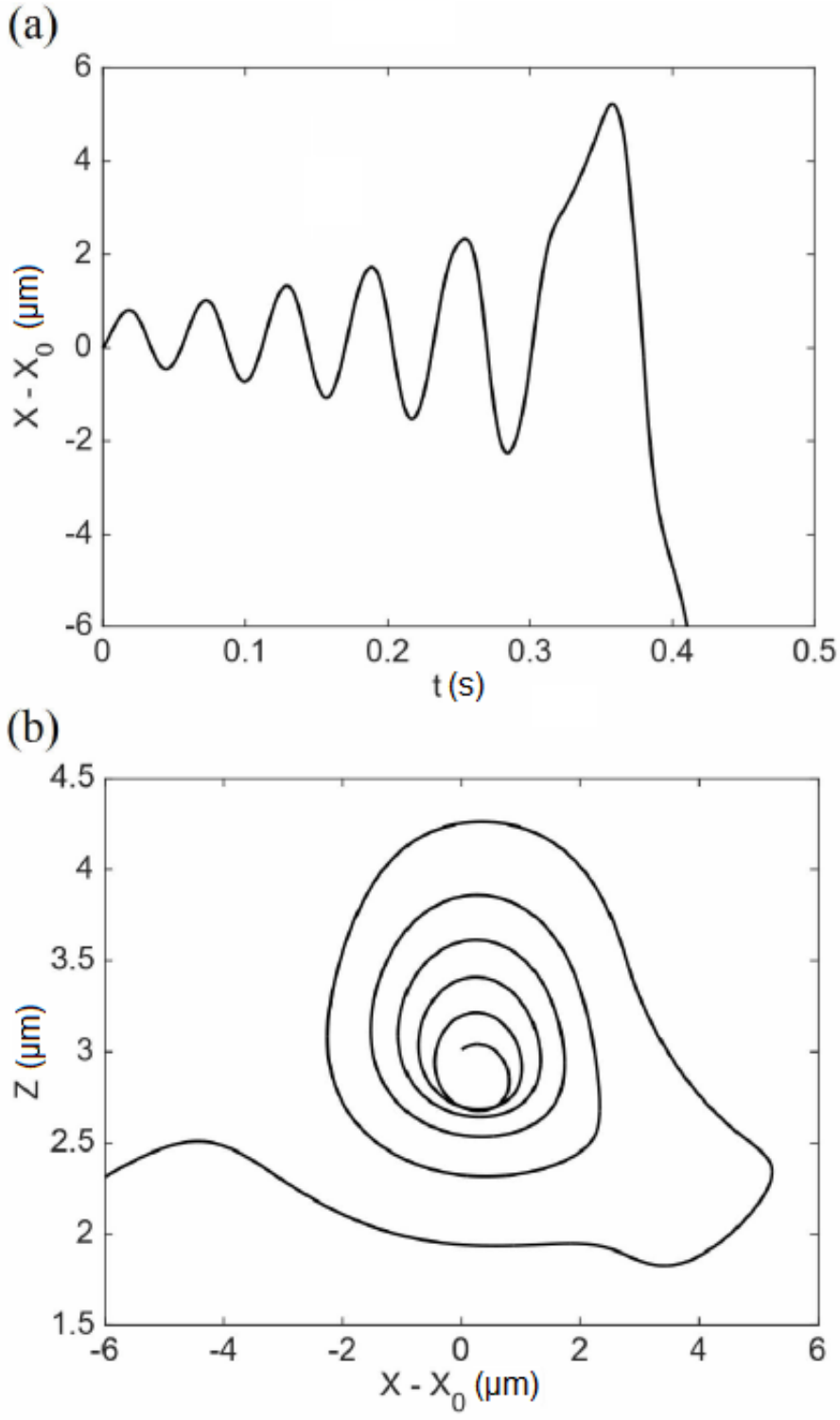

FIGURE 6.6: Numerically calculated trajectories of a tracer escaping from flow vortices between two RBCs with velocity 2.2 mm/s where X_0 is the center between the two RBCs. (a) Temporal forward-backward motion along the direction of the flow. (b) Toroidal trajectory in the x-y plane, starting from the middle and going outwards. Simulations by A. Guckenberger and J. Roemer

6.4 Summary

Using PTV experiments we measured the flow field around red blood cells flowing in small microchannels. For isolated RBCs, we found a significant difference in the flow field depending on whether the red blood cell is in the croissant or in the slipper state. At the rear of a slipper a small but characteristic vortex-like structure is observed. If two cells flow in close vicinity to each other in the croissant shape, another vortex-like structure appears between the cells as predicted by earlier numerical simulations [155, 156, 158, 140]. We showed that the rotation period in these vortices follows a quasi-linear law as a function of the distance between the red blood cells. Our experimental results are in good agreement with numerical boundary-integral simulations. The simulations, in addition, could illustrate qualitatively the trapping and escape of tracer particles from the vortex structures between the cells.

Résumé

Grâce à des expériences de PTV (Particle tracking velocimetry), nous avons mesuré le champ d'écoulement autour des globules rouges circulant dans de petits microcanaux. Pour les globules rouges isolés, nous avons trouvé une différence significative dans le champ d'écoulement selon que le globule rouge est à l'état de croissant ou de pantoufle (slipper). À l'arrière d'un slipper, on observe une petite structure caractéristique ressemblant à un vortex. Si deux cellules s'écoulent à proximité l'une de l'autre en forme de croissant, une autre structure vortex apparaît entre les cellules, comme le prédisaient des simulations numériques antérieures [155, 156, 158, 140]. Nous avons montré que la période de rotation dans ces tourbillons suit une loi quasi-linéaire en fonction de la distance entre les globules rouges. Nos résultats expérimentaux sont en bon accord avec les simulations numériques intégrales. Les simulations, en outre, ont pu illustrer qualitativement le piégeage et l'échappement des particules traceuses en dehors des structures en forme de vortex.

Zusammenfassung

Mit PTV (Particle Tracking Velocimetry) Experimenten haben wir das Strömungsfeld um rote Blutkörperchen gemessen, die in kleinen Mikrokanälen fließen. Bei

isolierten Erythrozyten fanden wir einen signifikanten Unterschied im Strömungsfeld, je nachdem, ob sich die roten Blutkörperchen im Croissant- oder im Slipperzustand befinden. Auf der Rückseite eines Slippers ist eine kleine, aber charakteristische, wirbelartige Struktur zu beobachten. Wenn zwei Zellen in unmittelbarer Nähe zueinander in der Croissantform fliessen, erscheint eine weitere wirbelartige Struktur zwischen den Zellen, wie durch frühere numerische Simulationen vorhergesagt [155, 156, 158, 140]. Wir zeigten, dass die Rotationsperiode in diesen Wirbeln einem quasilinearen Gesetz als Funktion des Abstands zwischen den roten Blutkörperchen folgt. Unsere experimentellen Ergebnisse sind in guter Übereinstimmung mit numerischen Boundary-Integral-Simulationen. Die Simulationen konnten darüber hinaus das Einfangen und Entweichen von Tracerpartikeln aus den Wirbelstrukturen zwischen den Zellen qualitativ illustrieren.

Chapter 7

Aggregation under flow

The development of microfluidic platform has given more insight about the blood properties in capillaries. However, most of the work relies on pure hydrodynamic interactions and adhesive forces are often discarded to simplify models and thus, aggregation of RBCs has been neglected. Claveria et al. [45] already carried out both experimental and numerical work to study the effect of aggregates in capillaries. Nevertheless, the effect of aggregation and the presence of bifurcation are often studied separately. In this chapter, we propose a microfluidic design that mimic asymmetric bifurcations in the microvascular network. The distribution of single cells/rouleaux in an asymmetric bifurcation has been studied for different flow rates and a transitioning threshold has been found for different concentration of dextran and fibrinogen at a physiologically relevant concentration. The nature of rouleaux' rupture after a microbifurcation has also been characterized for several flow rates. Low adhesive forces and high flow velocities can be coupled and lead to more rouleaux ruptures in the capillaries.

7.1 Stability of RBC clusters at bifurcations

The distribution of RBCs in microcapillaries but also their heterogeneous partitioning after bifurcations has been widely studied [179, 180, 181, 182, 183] and is now better understood. In physiological situations, blood flows through complex networks of capillaries that are connected by bifurcations. One can wonder what role these bifurcations play on the statistics of aggregate sizes in the microcirculation, as well as the hematocrit distribution in networks. A general feature of the flows of suspensions in capillary bifurcations is that when bifurcations are asymmetric, (e.g. different flow rates in the daughter branches), a higher concentration of particles (cells) is found in the daughter branch where the flow rate is highest, a phenomenon usually referred to as Zweifach-Fung effect [184]. At the scale of a microvascular network, this leads to strong heterogeneities of the haematocrit distribution, as already

notes in the pioneering work of Poiseuille[185]. Several parameters come into play to explain such discrepancy. Pries et al. [179] reported that the upstream distribution of cells has a role concerning the distribution in daughter branches. Moreover, the diameter of these branches (mother and daughter vessels) may favor or not the passage of RBCs and thus, affecting the partitioning. For instance, for a branching consisting of two daughter capillaries with different sizes, cell tend to chose the smaller vessels. Barber et al. [186] showed that rigidity of RBCs is also important in the partitioning. Rigid circular particles lead to obstruction of branches where as, soft particles undergo migration and flatten at the apex of bifurcations. These obstructions are can be found in pathological cases such as sickle cell anaemia since sickled RBCs are more rigid [187, 188]. Another interesting observation concerns the asymmetry of branches. The effect on partitioning is hardly noticeable . Since for small capillaries and due to low Reynolds (Re«1) numbers, inertial effects can be neglected and thus, blood flow is governed by Stokes equations. Moreover, Chien et al. [189] have already mentioned that even though cells tend to follow streamlines, this is less verifiable for capillaries. This also contributes to the heterogeneity in the distribution of RBCs in the micro-vascular system.

7.1.1 Design of the chip

The goal was to design a microfluidic chip that would mimic the blood capillaries and in particular bifurcations. The main difference, in comparison to blood capillaries, is that our channels have a rectangular aspect. Taking this into account, a design that aims to follow Murray's law:

where R is the radius of the mother vessel and $r_{1,2,...,n}$the radii of the daughter vessels.

$$R^3 = r_1^3 + r_2^3 + r_3^3 + ... + r_n^3 \tag{7.1}$$

This law is particularly valid for microvascular networks [190]. However, this has to be considered as a first approximation since this law applies for cylindrical channels. All the branches had to be brought back towards the central mother branch. The starting branch or mother branch is $10\,\mu m$ in height and $512\mu m$ in width. The daughter branches have the same height but their width is subdivided by two after each bifurcation reaching about $8\,\mu m$ at the end (Fig. 7.1). This leads to a constant cross-section before and after each bifurcation, therefore a constant average velocity along the network. The shear rate (essentially governed by the thickness of the channels) is also nearly constant except at the last level of bifurcations where

the side walls (and not only the top and bottom walls) lead to additional shear. The main additional hydrodynamic stress due to bifurcations is therefore the extensional stress due to fluid separation on each side of the stagnation point. Aggregates passing by the bifurcations were observed using a 20 fold objective and recorded with a frame rate up to 200 Hz. Rouleaux were manually characterized.

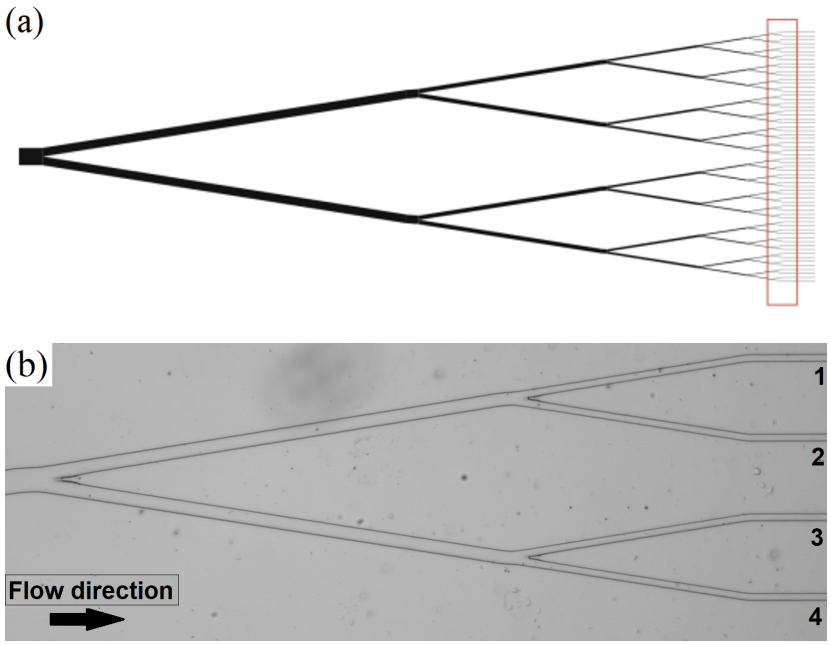

FIGURE 7.1: (a) Design of the microfluidic chip for the study of aggregates behaviour at bifurcations and (b) micro-image of the region of interest observed from the microfluidic chip. Channels from the top to the bottom are numbered from 1 to 4. Channels 1 and 4 are referred as external branches, 2 and 3 as internal branches.

7.1.2 Rouleaux distribution

RBCs rouleaux formation was induced using dextran at two different concentrations: 20 and 50 mg/ml and fibrinogen at a physiological concentration of 2.5 mg/ml. Blood from healthy donors was collected in the French blood bank and washed twice following the standard procedure (see 2.1.2). RBCs after being washed, were added to these solutions with a hematocrit of 1.5 %. While it is lower than physiological levels it allows to follow aggregates throughout the system and study the effect of hydrodynamic stress due to bifurcation on the stability and dissociation of isolated aggregates. Besides, it has been reported that hematocrit is lower in capillaries [191] compared to veins or arteries. Capillaries have varying size and shape

and thus, hematocrit may also vary a lot. The goal was to tweak the adhesive forces between RBCs to evaluate their contribution in maintaining aggregates as they cross bifurcations. In this study, we mostly focus on the channels depicted on Fig. 7.1 in the red rectangle. Nevertheless, what is observed at this location is related to previous branches.

Rouleaux distribution depending on the aggregate velocity

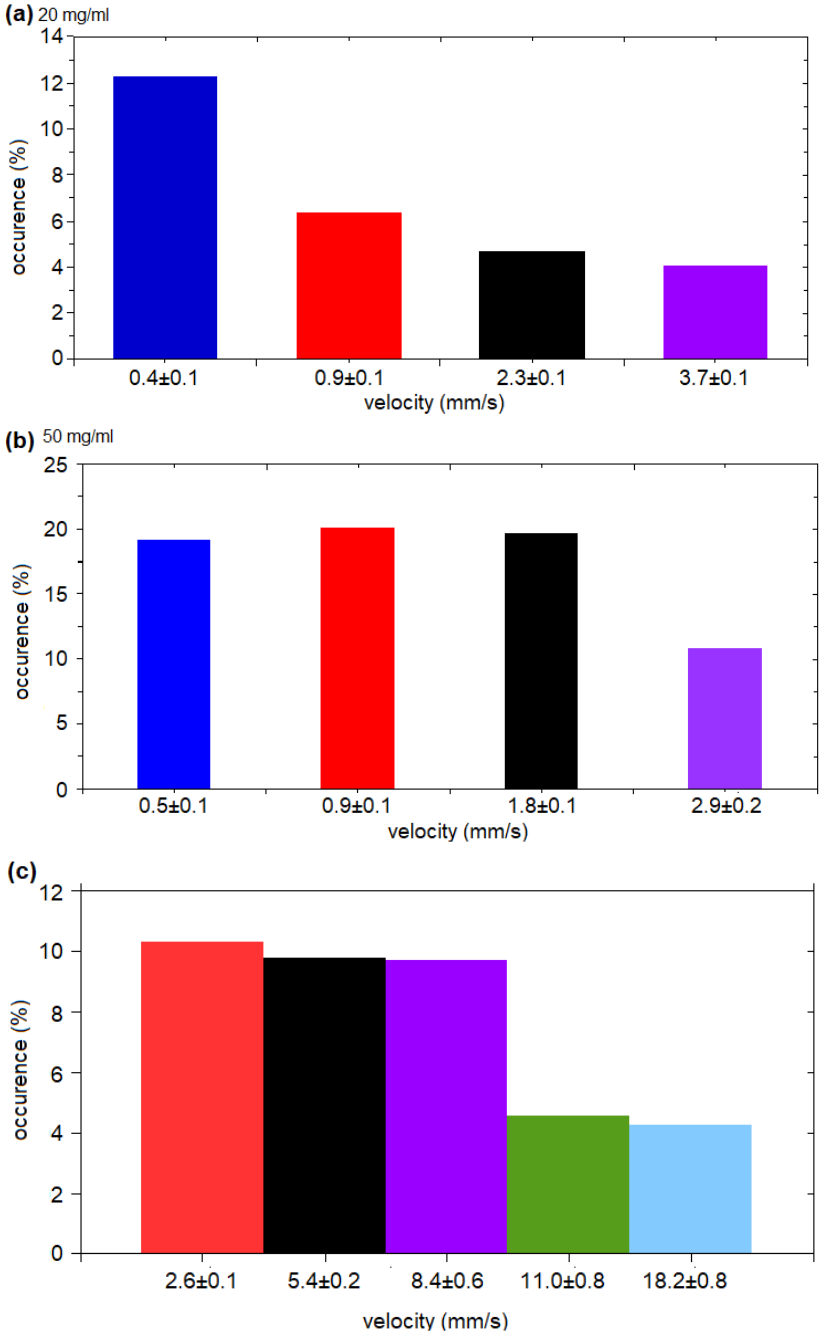

FIGURE 7.2: Percentage of aggregates (2 and more cells) passing by the bifurcation for several velocities ranging from $v_{RBC} = 0.4$ to $v_{RBC} = 20$ mm/s for dextran (70 kDa) with a concentration of (a) 20 mg/ml (b) 50 mg/ml and (c) fibrinogen at 2.5 mg/ml

The distribution of rouleaux sizes was investigated for several flow rates ranging from $v_{RBC} = 0.4$ mm/s to $v_{RBC} = 3.7$ mm/s in the case of dextran and up to $v_{RBC} = 18.2 \pm 0.8$ mm/s for fibrinogen. A certain threshold has been found for which the

population of rouleaux drops significantly. For 20 mg/ml, we can see on Fig. 7.2 a population of about 12 % of rouleaux which is the maximum. This is favored by the rather low flow rates causing weak interaction forces, whether they are due to extensional or shear stress. At $v_{RBC} = 0.9 \pm 0.1$ mm/s, this population is divided by two and stagnates at about 4 % for higher flow velocities.
At 50 mg/ml, the population of aggregates is greater on average du to higher adhesive forces. Most of the aggregates survive for up to $v_{RBC} = 1.8 \pm 0.1$ mm/s. We observed about 20 % of rouleaux at these pressure drops. At $v_{RBC} = 2.9 \pm 0.2$ mm/s, we see the population of rouleaux decreasing by a factor 2. One should mention that aggregates of 3 and more RBCs represent about 10 % of the total aggregates for dextran at 50 mg/ml and are almost absent in the case of dextran at 20 mg/ml (not shown on the graph).
For fibrinogen with a concentration of 2.5 mg/ml, we chose higher flow velocities since the transition threshold appears at higher flow velocities. This is due to the extreme stability of aggregates and the strong adhesive forces involved. About 10 % of aggregates can be found at velocities under $v_{RBC} = 8.4 \pm 0.6$ mm/s and a significant diminution by a factor 2 is observed after this particular velocity v_{RBC}.

Rouleaux distribution in daughter branches

We, then, took a deeper look into these aggregates. Fig. 7.3 shows the distribution of rouleaux (of more than 2 RBCs) in each channel (Fig. 7.1). Doublets were discarded since the represent an important fraction of the total number of aggregates and may hinder the contribution of the adhesive forces for larger rouleaux in a given solution. The number of rouleaux (N >2 RBCs) has been normalized in a given channel by the total number of cells passing by this same channel.

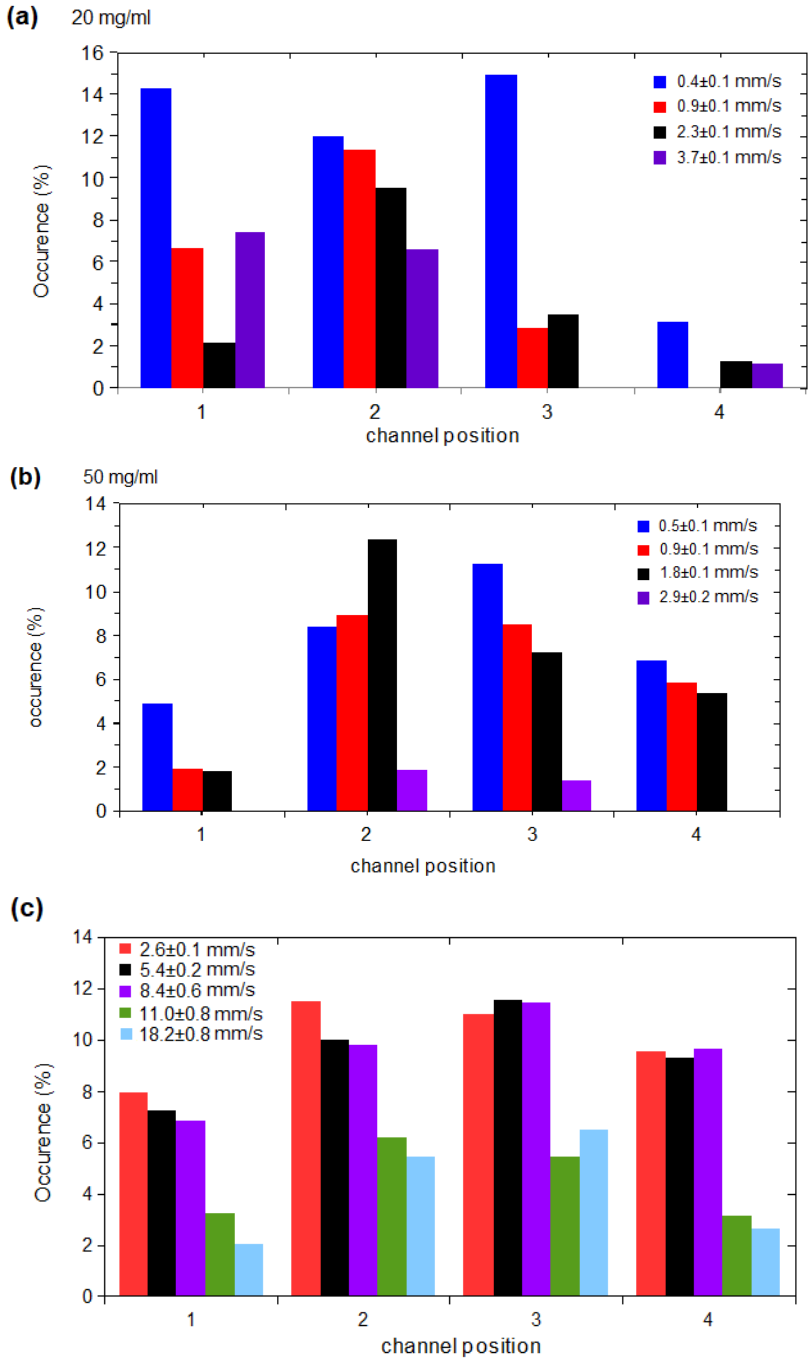

FIGURE 7.3: Distribution of rouleaux constituted of N >2 RBCs normalized, for each channel, by the number of cells passing by the same channel for a given flow velocity for dextran (70 kDa) with a concentration of (a) 20 mg/ml (b) 50 mg/ml and (c) fibrinogen at 2.5 mg/ml

The first observation is that rouleaux represent about 10 % of the object flowing in each channel. The asymmetry of the bifurcation is responsible of the distribution of RBCs aggregates in the branches. This has a particularly stronger effect on higher

concentration of dextran as Fig. 7.3 (b) shows. In fact, RBCs have a privileged path due to the angular asymmetry of the channels and favour the internal branches.

For fibrinogen, the number of aggregates passing by the bifurcation is similar to a low concentration of dextran (20 mg/ml) with an average of 10 % aggregates. A clear threshold can also be observed, here, between $v_{RBC} = 8.4 \pm 0.6$ and $v_{RBC} = 11.0 \pm 0.8$ mm/s. Here the number of aggregates drops about 5 %. Less aggregates survive at this level of the bifurcation. The same trend can be acknowledged, taking into account clusters of 3 and more RBCs, for each channel. Similarly to a higher concentration of dextran (50 mg/ml) and due to the asymmetry of the bifurcation, the inner path (channels 2 and 3) is favored and a slightly larger percentage of aggregates pass by these channels.

It appears that rouleaux reorient themselves in the direction of the flow. They align along the streamlines throughout the microfluidic branches. For this reason, the orientation doesn't play a major role in the breaking events. However, the position of a rouleau in the channel is an important parameter to take into consideration. In fact, rouleaux happening to be in the middle of the channel will have higher chances to break after hitting the apex. Nevertheless, the effect of the rouleau's orientation is not in the scope or our study. For mother vessels with a width close the RBC size, the chances of breaking due to the apex is even higher as margination effects are less pronounced.
One can agree that some other factors may play a role on the (dis)aggregation of RBCs in flow such as : the presence of the epithelium, the presence of stiffer objects (usually marginated) such as leukocytes or even platelets.

7.1.3 Breaking events

Both shear and extensional forces were taken into account. Aggregates can break for several reasons. Bifurcations are expected to play a major role in breaking rouleaux in flow since they represent an obstacle for the passing of RBC aggregates. However, rouleaux also break due to shear stress particularly in smaller channels where confinement is more pronounced. For this reason, two causes of breaking events are distinguished:

- Shear breaking: Rouleaux breaking due to hydrodynamic interactions and

shear stress induced by the narrow channels. These interactions can be between cells or between rouleaux and the wall (Fig. 7.4).

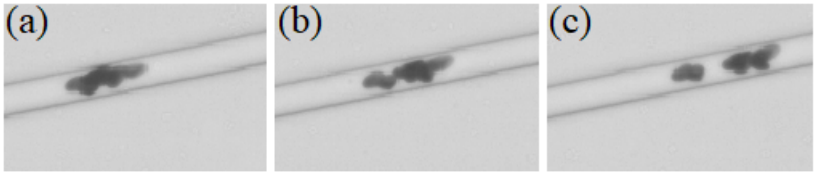

FIGURE 7.4: Micro-images of an aggregate breaking due to shear stress as it travels from (a) to (c) along the microcapillary

- Extensional breaking: Rouleaux which breaks because of the apex of the bifurcation. It can be either because the rouleau's size is too big so it has to rupture to cross the bifurcation or the rouleau is oriented in the middle of the mother channel and hits the apex oriented perpendicularly to the direction of flow (Fig. 7.5).

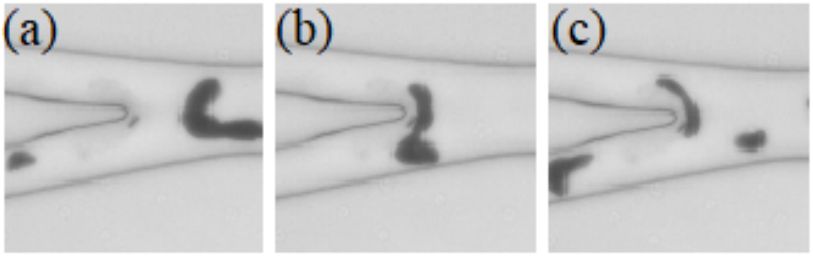

FIGURE 7.5: Micro-images taken at 3 consecutive frames from (a) to (c) of an aggregate breaking at the apex of the bifurcation due to the stagnation point

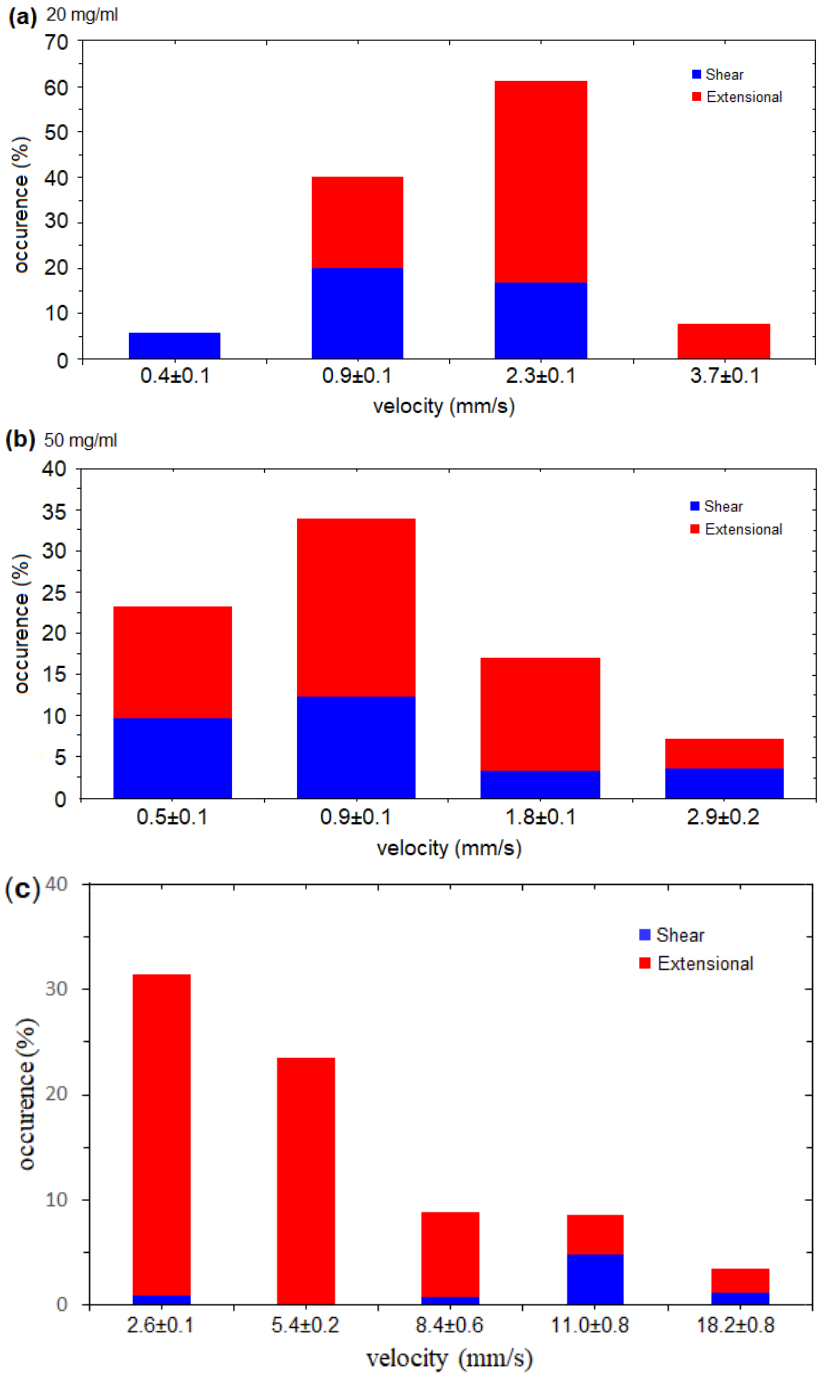

FIGURE 7.6: Repartition of breaking events showing both the shear and extensional shear contributions for a concentration of dextran (70 kDa) of (a) 20 mg/ml and (b) 50 mg/ml and (c) fibrinogen at 2.5 mg/ml

We observed that for high adhesive energies in dextran (50 mg/ml), the size distribution is between 2 and 7 RBCs as already stated by Claveria et al. [45], whereas for lower concentration of dextran (20 mg/ml), we mostly observe single cells and doublets. Unless stated otherwise, we consider as rouleaux, aggregates with a size

of 2 or more cells. The percentage of aggregates for a given flow velocity is normalized by the total population of aggregates flowing in the channels. Compared to the total number of RBCs (including single cells), these events represent a low fraction (less than 10 %). For low velocities, adhesive forces dominate. Higher interaction energies lead to bigger aggregates at the last bifurcations since rouleaux are less prone to break due to hydrodynamic interactions. Thus, the survivability of aggregates is greater for 50 mg/ml. Nevertheless, for this concentration of dextran, where aggregation is known to be the highest, rouleaux, which are too big for the daughter branch, will break at the apex to pass through the bifurcation.
For intermediate velocities, i.e. between $v_{RBC} = 0.9 \pm 0.1$ and 2.3 ± 0.1 mm/s, we observe a higher fraction of rouleaux breaking as the hydrodynamic forces become more important and the velocity at which rouleaux collide with the apex is also more significant. There exists a threshold at these flow velocities where the probability of breaking an aggregate is high. We also investigated flow velocities above these thresholds such as $v_{RBC} = 2.9 \pm 0.2$ mm/s, for instance. We observe much lower breaking events because the velocity and hydrodynamic interactions of rouleaux are much higher. Moreover, most of the rouleaux tend to break in antecedent bifurcations and thus, less rouleaux are present in the bifurcation of observation.
The major difference compared to dextran in terms of breaking events is that these events are more rare. This shows that aggregation induced by fibrinogen leads to more stable aggregates and most likely, adhesive interactions are stronger. This is why, these breaking events are mainly governed by adhesive interactions rather than hydrodynamic ones. For aggregates with a low velocity ($v_{RBC} = 0.4$ mm/s), these breaking events are about 6 %. At this point, hydrodynamic interaction are negligible. At lower aggregate velocities v_{RBC}, the shear stress in capillaries is not enough to induce the dissociation of rouleaux The main reason for the presence of these breaking events is due to the size of the rouleaux that have to break in order to get through the bifurcation. The other reason is due to the orientation of rouleaux which trajectory crosses the apex of the bifurcation.

7.2 Aggregation in shear flow

Blood is a complex fluid known to be non-Newtownian. In fact, the viscosity of blood is mainly determined by the RBC and its ability to aggregate. At higher shear rates, blood viscosity decreases due to rouleaux' rupture causing the so-called: shear-thinning of blood [192, 193, 194] and models have already been proposed [195,

196] to relate the aggregation level to effective viscosity. Rouleaux formation or aggregation also plays a major role in blood sedimentation. Aggregation of RBCs causes faster sedimentation rates as it is often the case in pathologies due to inflammation (higher concentration of fibrinogen). The sedimentation rate results from a balance between weight and viscous drag. For a given density, the weight is proportional to the volume of the object and the viscous drag is proportional to its diameter. RBCs, by forming rouleaux thanks to the proteins (fibrinogen, gamma globulins, C-reactive proteins, ...) [197] contained in plasma, make the volume/diameter ratio bigger and thus, sediment faster. One can affirm that there is an interplay between the aggregation, the viscous properties of blood and gravity. It is a well known fact that when doing macroscopic measurements of blood viscosity with rheometers, one has to be careful about possible artifacts due to RBCs sedimentation in the measuring device during the measurement period.
Thanks to parabolic flights, it is possible to (almost) get rid of gravity and experiments performed in microgravity allow to observe and measure aggregates in steady conditions at low shear rates.

7.2.1 Material and methods

In the experiment, a dilute suspension of RBCs with a controlled concentration of dextran (to promote aggregation) is introduced in a shear flow chamber made of two parallel glass discs separated by a gap of about 200 µm, just before or at the beginning of the microgravity phase. The sample is then sheared at low shear rate (typically 1-10 s^{-1}), which at the same time promotes collisions/contacts between cells and aggregate disaggregation due to shear stresses. A balance then takes place between aggregation and disaggregation which conditions aggregate size. Images are recorded via digital holographic microscopy to characterize the size and shape distribution of aggregates.

The results presented here were obtained during the 55th CNES parabolic flight campaign (VP139) onboard the Airbus 310 ZERO-G of Novespace (Mérignac, France, september-october 2018) and were conducted in collaboration with T. Podgorski, G. Coupier, P.Ballet from LIPhy. The flow chamber (Fig. 7.7) and the syringe pump (Fig. 7.8) was designed by P. Ballet.

Flow chamber

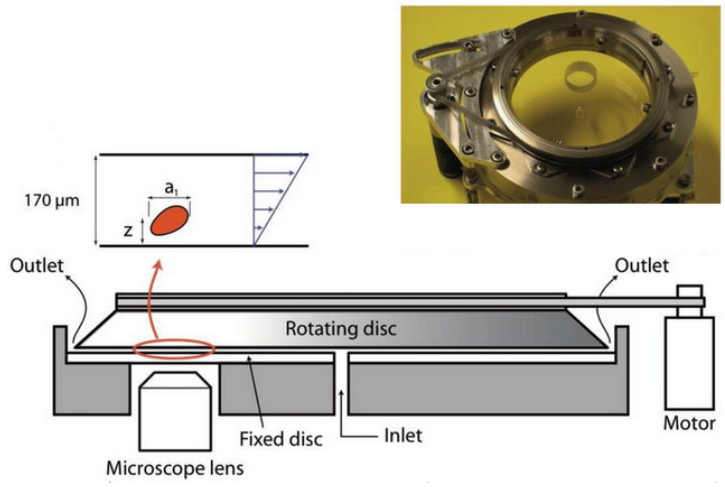

FIGURE 7.7: Photo and sketch of the shear flow chamber. On the picture, the black cylinder on the left is the motor, connected to the top rotating disc by a belt. On the sketch (cross section), the rotating disc is the conical piece (thickness 20 mm). This piece is guided by a ball bearing. The bottom disc is made up of two parts : a 2 mm glass plate, reinforced by a 10 mm thick glass plate (glued). The 10 mm plate has a hole around the observation point, to limit the glass thickness to 2mm at the observation point.

Pumping syringes

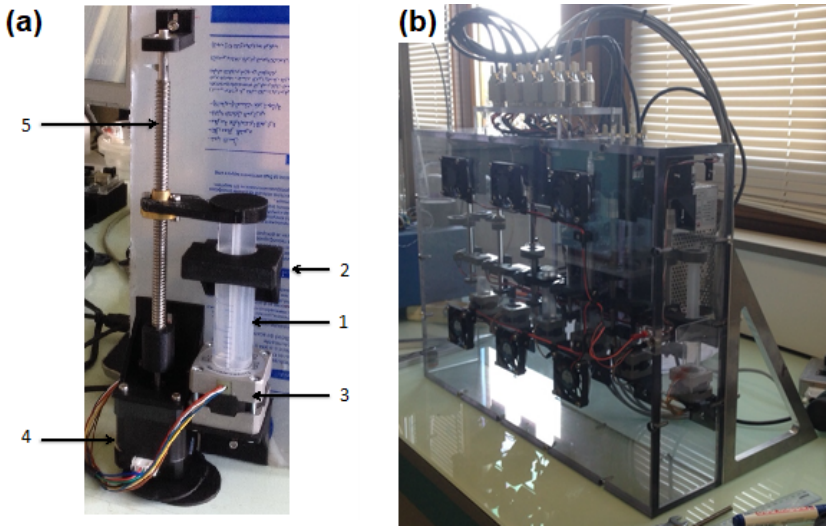

FIGURE 7.8: (a)one syringe pump unit. The 20ml syringe body (1) is maintained by a holding bracket (2) and the bottom is inserted into the stator of a stepper motor used as magnetic stirrer (3). The syringe piston is driven by a stepper motor (4) thanks to a driving screw (5) and (b) overall view of the syringe pump with mounting brackets.

C. Minetti from MRC Brussels (ULB) provided the optical instrument and image processing. The experiment consists in injecting a blood cell suspension in a shear flow chamber where it is sheared at constant rate and images of the flowing RBCs and aggregates are recorded with a digital holographic microscope. The central part of the experimental setup is a shear flow chamber (two glass discs, one of which is rotating), mounted on a digital holographic microscope. This instrument allows, after processing the recorded holographic information, to obtain information on the 3D position and shape of objects in the suspension that is sheared in the chamber during the experiment. (Fig. 7.7)

The observation is made with a digital holographic microscope (DHM) equipped with a digital CCD camera linked to a PC (Fig. 7.9). The observation volume is about 400x400x200 µm. The DHM is an interferometer with a laser beam (class 3B, wavelength 635 nm), widened by a lens (widened beam cross section is several mm2), diffused by a ground glass and split by a beam splitter. It goes through the flow chamber and interferes with a reference beam to produce a hologram on the CCD sensor of the camera. More details about this experimental setup has already been published [198, 199, 200].

Holographic microscope

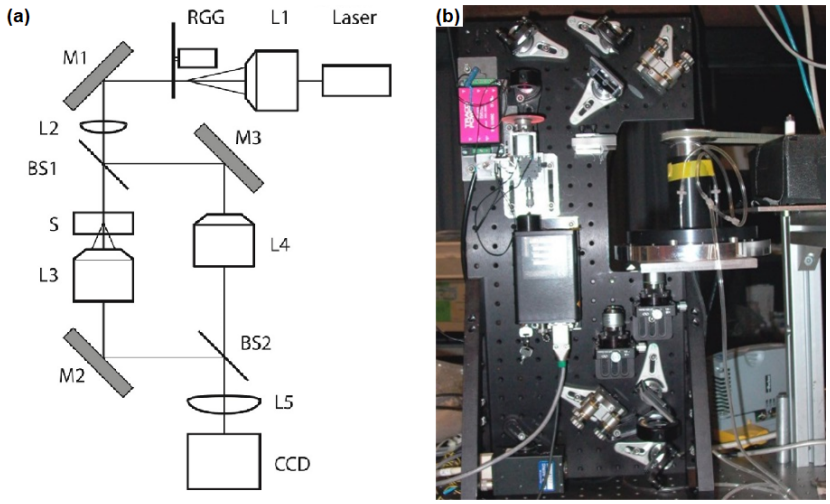

FIGURE 7.9: (a) Scheme of the DHM (L1, L2, L3, L4 : lenses ; M1, M2, PM : mirrors ; BS1, BS2 : beam splitters ; S: Sample [microchannel chip]) and (b) photo of the holographic microscope on a lab bench out of the rack (with a prototype of the shear flow chamber)

RBC suspensions were prepared by the classic method (see section 2.1.2) by washing blood from healthy donors (from EFS Rhône-Alpes) in a PBS solution and then re-suspending them in a PBS+Dextran (70 kDa) solution with a volume fraction between 0.5 and 1%. Dextran concentrations were 20 and 50 mg/ml.

7.2.2 First preliminary results

Processing of the holographic data allows, after segmentation, to retrieve for each detected object the integral of the phase difference between the object and the background. Knowing the refractive indexes of the suspending fluid (dextran solution) and the hemoglobin solution inside RBCs at average physiological concentration, the phase integral can be converted to the physical volume of the object. A typical histogram of volume distribution obtained over 50 consecutive images at the end of a parabola when steady state is reached is shown in Fig. 7.10

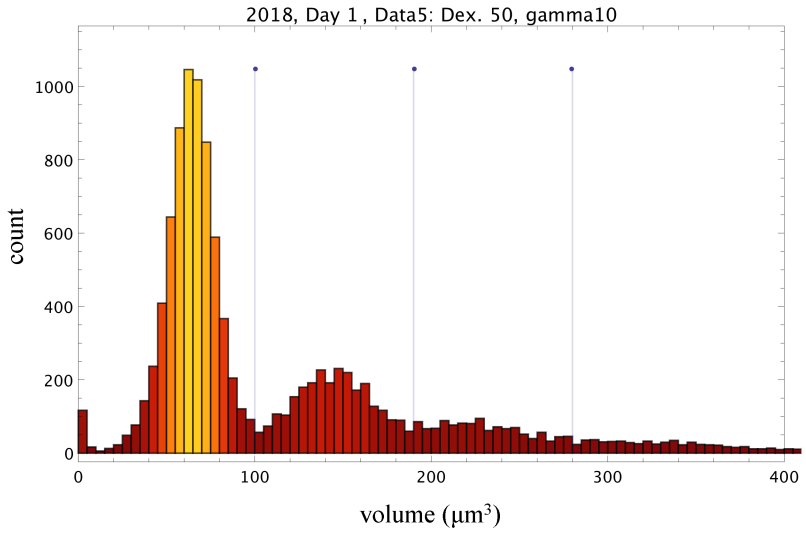

FIGURE 7.10: Typical raw data obtained for dextran (70kDa) at a concentration of 50 mg/ml and a shear rate of $\dot{\gamma} = 10s^{-1}$ showing the number of objects as a function of their volume. The first peak represents the number of single cells, the second : doublets and so on.

These histograms, which correspond to populations of the order of 10^4 objects, exhibit distinct peaks corresponding to volumes of single unaggregated RBCs (80-100 μm^3), 2 cells, 3 cells etc... The distribution of single cells and rouleaux has been retrieved for low shear rates ranging from $\dot{\gamma} = 0$ to $\dot{\gamma} = 35s^{-1}$. Aggregates have therefore been counted as doublets, triplets and aggregates equal or greater than 4 cells, allowing for each parameter set (dextran concentration, shear rate) to compute the fraction of each type of objects. According to the bell shape and OT force measurements (see Fig. 4.4), a concentration of dextran (70 kDa) at 20 mg/ml induce rather low adhesive forces between the cells and 50 mg/ml promote a higher aggregation of RBC. The general tendency for any concentration is that the fraction of single cells tends to increase at higher shear rates and therefore, the fraction of aggregates decreases as it can be seen on Fig. 7.11. Although we are at low hematocrit here, the results are consistent with the shear-thinning of blood [137, 192] associated to disaggregation as shear rate is increased. It is worth noting that even at the highest shear rate investigated here ($30s^{-1}$), the fraction of aggregates is still significant.

For a concentration of 20 mg/ml and up to $\dot{\gamma} < 10s^{-1}$, the fraction of single RBC remains steady at $f_1 = 0.7$. The doublets constitutes the second most abundant aggregates with $f_2 = 0.2$ and bigger aggregates represent about $f_{i>2} = 0.1$.

At 50 mg/ml, the fraction of single RBC represent about half of the flow chamber at $\dot{\gamma} = 5s^{-1}$ and increases linearly as a function of the shear rate and up to $\dot{\gamma} < 10s^{-1}$. At higher shear rates $\dot{\gamma} > 15s^{-1}$, a plateau is reached and single RBCs constitute about $f_1 = 0.8$ of the flow chamber. One should notice that doublets always represent the highest fraction of rouleaux at any shear rate and for any concentration of dextran and that bigger aggregates (3 or more) which represent a rather high fraction at low shear rates, rapidly disappear above $\dot{\gamma} = 10s^{-1}$ at these low hematocrits.

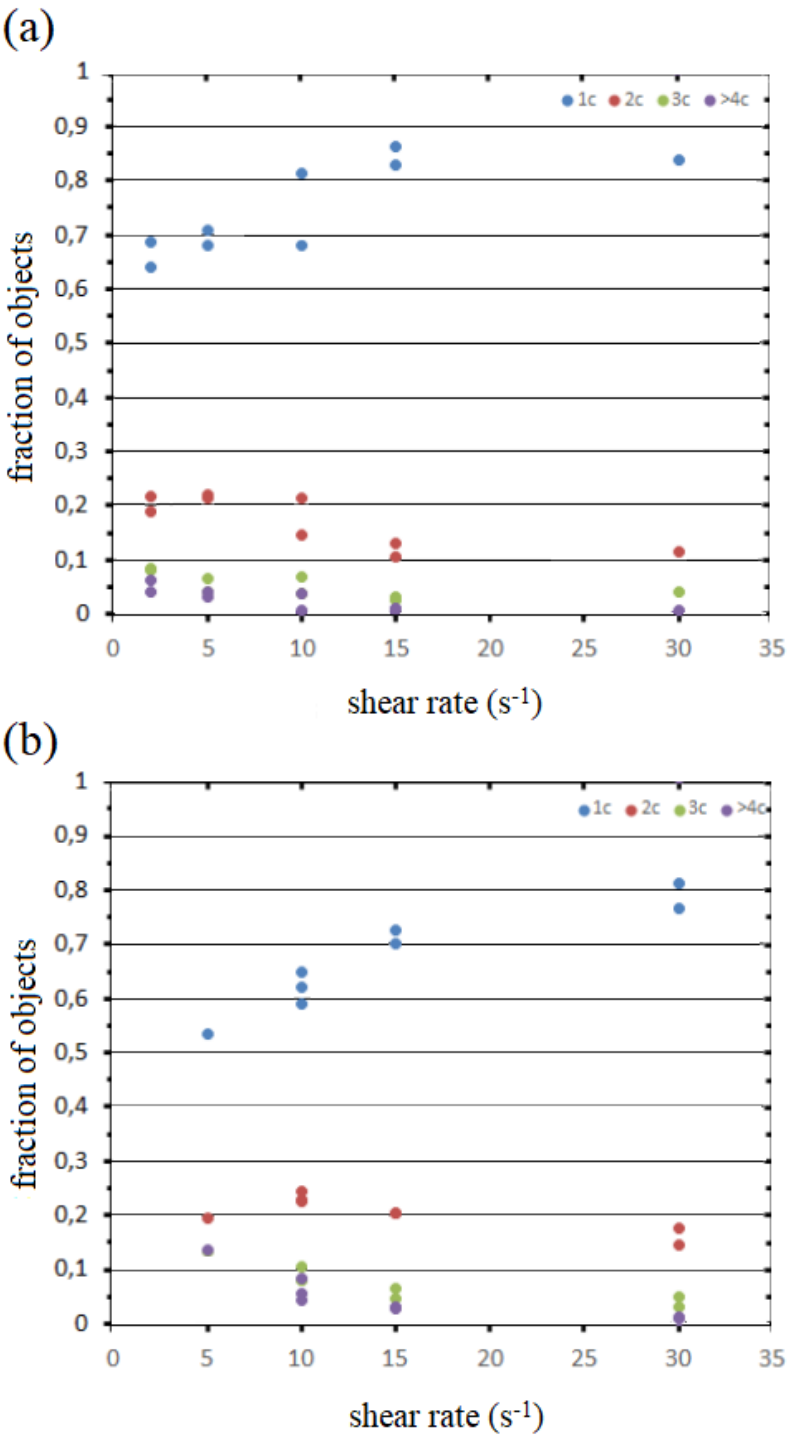

FIGURE 7.11: Fraction of RBC aggregates for two concentrations of Dextran: (a) 20 mg/ml and (b) 50 mg/ml at low shear rates. 1c (in blue): 1 cell, 2c (in red): 2 cells, 3c (in green): 3 cells and 4c (in purple): 4 cells and more

To better grasp the significance of the total rouleaux fraction present in the flow chamber, the aggregation index I is calculated as follows:

$$I = \frac{n_2 f_2 + n_3 f_3 + n_4 f_4}{n_1 f_1 + n_2 f_2 + n_3 f_3 + n_4 f_4} \tag{7.2}$$

where f_i is the fraction of single cells or rouleaux with i cells and n_i the number of i cells. Fig. 7.12 shows, in good agreement with our OT measurements (see Fig. 4.4), that the aggregation index I is lower for a concentration of 20 mg/ml than for 50 mg/ml.

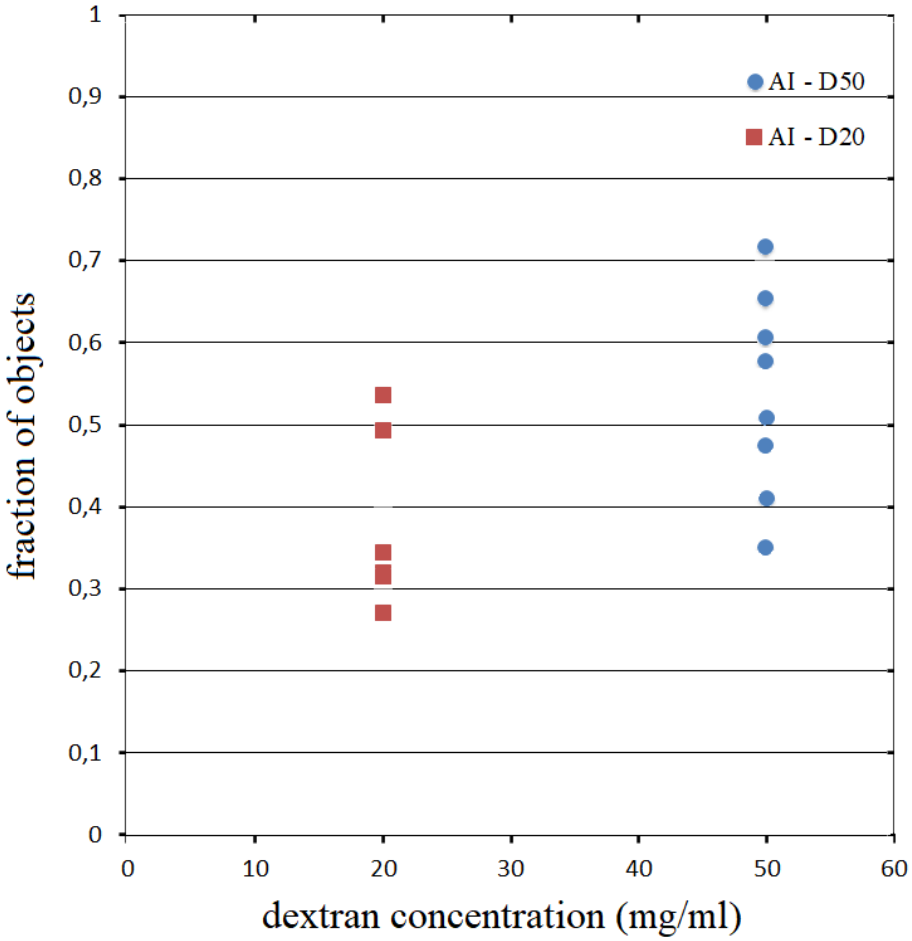

FIGURE 7.12: Aggregation index calculated for two concentrations of dextran: 20 mg/ml (red) and 50 mg/ml (blue), for all values of shear rates

The aggregation index I was also reported for several shear rates (Fig. 7.13). As the shear rate increases, the number of rouleaux breaking increases and the aggregation index I decreases almost linearly between $\dot{\gamma} = 0 s^{-1}$ and $\dot{\gamma} = 15 s^{-1}$. After

$\dot{\gamma} = 15s^{-1}$, $I = 0.3$ within experimental scattering and remains almost constant for a concentration in dextran of 20 mg/ml. For 50 mg/ml, I drops from $I = 0.5$ to $I \approx 0.4$ at $\dot{\gamma} = 30s^{-1}$

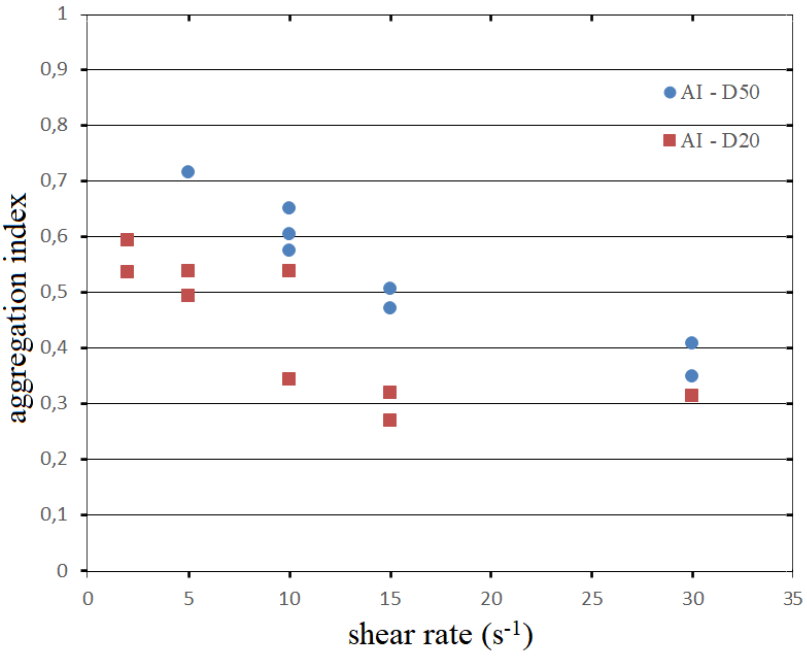

FIGURE 7.13: Aggregation index calculated as a function of the shear rate for two concentration of dextran: 20 mg/ml (red) and 50 mg/ml (blue)

7.3 Summary

In this chapter, experiments were dedicated to the study of fibrinogen and dextran induced rouleaux in bifurcating micro-capillaries and in a flow chamber. It was shown that there is a threshold for both aggregating agents where adhesive forces become too weak leading to more aggregates of smaller size (mostly doublets). In the microcapillary network, breaking events have a mechanical contribution mainly due to the size or the orientation of the aggregates. Breaking events due to hydrodynamic interactions are present for lower velocities (lower shear stress) and for lower adhesive interactions since rouleaux have a lower velocity they are less likely to break at the apex but these events remain quite rare. In this work, a very precise bifurcation with a size close to that of RBCs, which is a common situation in capillary networks, was observed and gave a early outlook on aggregates reaching a micro-bifurcation. However, it could be relevant to track aggregates from the mother vessel to smaller vessels to monitor breaking events but also the importance

of the aggregates' orientation into these events. Experiments performed in microgravity conditions provided a first set of quantitative results on the size distribution of aggregates in simple shear flow, that should be useful for models of blood rheology taking into account aggregation-disaggregation dynamics. This track should be pursued in the future to explore a wider range of parameters.

Résumé

Dans ce chapitre, des expériences ont été consacrées à l'étude des rouleaux induits par le fibrinogène et le dextran dans des micro-capillaires bifurquants et dans une chambre d'écoulement. Il a été montré qu'il existe un seuil pour les deux agents d'agrégation où les forces d'adhésion deviennent trop faibles, ce qui entraîne un plus grand nombre d'agrégats de taille plus petite (principalement des doublets). Dans le réseau de microcapillaires, les événements de rupture ont une contribution mécanique principalement due à la taille ou à l'orientation des agrégats. Les ruptures dues à des interactions hydrodynamiques sont présentes pour des vitesses plus faibles (contrainte de cisaillement plus faible) et pour des interactions adhésives plus faibles, car les rouleaux ont une vitesse plus faible et sont moins susceptibles de se rompre à l'apex mais ces événements restent assez rare. Dans cette étude, une bifurcation très précise avec une taille proche de celle des globules rouges, ce qui est une situation courante dans les réseaux capillaires, a été observée et a donné un premier aperçu des agrégats atteignant une micro-bifurcation. Cependant, il pourrait être pertinent de suivre les agrégats depuis les branches "mère" jusqu'aux branches plus petites pour surveiller les événements de rupture, mais aussi l'importance de l'orientation des agrégats dans ces événements. Les expériences réalisées dans des conditions de microgravité ont fourni une première série de résultats quantitatifs sur la distribution de taille des agrégats dans un flux de cisaillement simple, ce qui devraient être utiles pour les modèles de rhéologie sanguine prenant en compte la dynamique d'agrégation et désagrégation. Cette piste pourrait être poursuivie à l'avenir pour explorer un plus large éventail de paramètres.

Zusammenfassung

In diesem Kapitel wurden Experimente zur Untersuchung von Fibrinogen- und Dextran-induzierten Rouleaux in gegabelten Mikrokapillaren und in einer Strömungskammer durchgeführt. Es konnte gezeigt werden, dass es für beide Aggregationsmittel einen Schwellenwert gibt, bei dem die Adhäsionskräfte zu gering werden,

was zu mehr kleineren Aggregaten (hauptsächlich Dubletten) führt. Im Mikrokapillarnetz haben Ausfallereignisse einen mechanischen Beitrag, der hauptsächlich auf die Größe oder Ausrichtung der Aggregate zurückzuführen ist. Brüche aufgrund hydrodynamischer Interaktionen treten bei niedrigeren Geschwindigkeiten (geringere Scherbeanspruchung) und bei geringeren Adhäsionsinteraktionen auf, da die Rouleaux geringere Geschwindigkeiten haben und weniger wahrscheinlich am Apex brechen aber diese Ereignisse bleiben ziemlich selten. In dieser Untersuchung wurde eine sehr präzise Bifurkation mit einer Größe nahe der der roten Blutkörperchen beobachtet, wie sie in Kapillarnetzwerken häufig vorkommt, und gab einen ersten Eindruck davon, wie die Aggregate eine Mikrobifurkation erreichen. Es könnte jedoch relevant sein, Aggregate von "Mutter"-Kanälen bis zu kleineren Kanälen zu verfolgen, um Bruchereignisse zu überwachen, aber auch die Bedeutung der Ausrichtung der Aggregate bei diesen Ereignissen. Experimente, die unter Mikrogravitationsbedingungen durchgeführt wurden, haben einen ersten Satz quantitativer Ergebnisse zur Größenverteilung von Aggregaten in einer einzigen Scherströmung geliefert, die für blutrheologische Modelle unter Berücksichtigung der Aggregations- und Disaggregationsdynamik nützlich sein dürften. Dieser Weg könnte in Zukunft verfolgt werden, um ein breiteres Spektrum von Parametern zu erforschen.

Chapter 8

General conclusion and perspectives

The research carried out and presented in this thesis is interdisciplinary and combines hematology with different fields of physics. Based on the measurement of physical quantities to assess the physical properties inherent to RBCs, it aims to provide a better understanding of RBCs interaction. The main phenomenon studied here is the aggregation of RBCs seen under the scope of two different techniques: optical tweezers and microfluidics.

Experiments at a single cell level revealed that adsorption of macromolecules onto the RBC surface occurs while rapidly changing the surrounding medium. The technique presented in this thesis allows the quantification of the adsorbed macromolecules and could also be used for quantifying the adsorption of plasma proteins.

In addition, we investigated the (dis)aggregation of multiple pairs of RBCs in various media. Dextran was and is still used to elucidate the mechanisms of aggregation. Our work aimed to compare dextran with a pure depletant (Fd virus) and show whether it could be used to verify the depletion model. Our results suggest that dextran cannot be seen as a pure depletant. We also found a discrepancy in terms of measured forces. The aggregation force in presence of dextran is lower than the disaggregation force. In contrary, the disaggregation and aggregation forces measured in presence of a pure depletant (Fd virus) is of the same order of magnitude.

Thanks to 3 dimensional simulations conducted at the Forschungszentrum Jülich, a whole phase diagram of RBCs doublets has been established by taking into account the influence of the spectrin network. Experiments could reproduce a variety of these doublets shapes. Two doublet shapes, The Male-Female and Sigmoid-Biconcave, have been proven to facilitate the nucleation into larger aggregates.

Another set of experiments has been carried out under flow. The flow field around single RBCs has been studied. Hydrodynamically formed clusters of RBCs were studied and revealed possible applications for drug delivery. Vortices have been observed and characterized backed up by 3D simulations performed by the group of S. Gekle. We showed that the rotation period in these vortices follows a quasi-linear

law as a function of the distance between the red blood cells.
The formation of rouleaux in the microcirculation is mainly due to hydrodynamic forces but also more importantly adhesive forces. Moreover, the contribution of hydrodynamic and adhesive forces (induced by Dextran) on the disaggregation of aggregates under flow has been explored in-vitro, in a ramified network of bifurcations and in a flow chamber. It disclosed an existing velocity and shear rate for which adhesive forces vanish in capillaries in both dextran and fibrinogen. Rouleaux formed in presence of fibrinogen have shown to be more stable and can be expected to have stronger interaction energies.
Further experiments to better understand and unravel the aggregation mechanism are still planned. One of them consists of using specific bridger (DNA linkers). The (dis)aggregation of RBCs could be investigated and compared with dextran and Fd virus (pure depletant). The goal is to see to which extent it could be assimilated to plasma later on. Similar experiments in autologous plasma have already been performed in the same way as for dextran and Fd-virus. The analysis of their traces is still under process and a direct comparison to the two other protagonists (Fd and DNA linkers) may shed light on the underlying mechanisms of RBCs aggregation.
In a nutshell, many aspects of the physical properties of RBCs and their influence on the aggregation have been discussed in this thesis. Our work showed that aggregation may be more complex than it seems and the techniques detailed in this work are good tools to tackle the remaining opened questions.

Conclusion générale et perspectives

Les recherches menées et présentées dans cette thèse sont interdisciplinaires et combinent l'hématologie avec différents domaines de la physique. Basée sur la mesure de quantités physiques pour évaluer les propriétés physiques inhérentes aux GRs, elle vise à fournir une meilleure compréhension de l'interaction des GRs. Le principal phénomène étudié ici est l'agrégation des GRs vue par l'intermédiaire de deux techniques : les pinces optiques et la microfluidique.
Des expériences au niveau d'une seule cellule ont révélé que l'adsorption de macromolécules sur la surface du GR se produit et ce, tout en modifiant rapidement le milieu environnant. La technique présentée dans cette thèse permet la quantification des macromolécules adsorbées et pourrait également être utilisée pour quantifier l'adsorption des protéines plasmatiques.
De plus, nous avons étudié la (dés)agrégation de multiples paires de globules rouges

dans différents milieux. Le dextran était et est toujours utilisé pour élucider les mécanismes d'agrégation. Notre travail a visé à comparer le dextran avec un déplétant pur (virus Fd) et à montrer s'il pouvait être utilisé pour vérifier le modèle de déplétion. Nos résultats suggèrent que le dextran ne peut pas être considéré comme un déplétant pur. Nous avons également constaté un écart en termes de forces mesurées. La force d'agrégation en présence de dextrane est inférieure à la force de désagrégation. Au contraire, les forces de désagrégation et d'agrégation mesurées en présence d'un déplétant pur (virus Fd) sont du même ordre de grandeur.
Grâce à des simulations tridimensionnelles réalisées au Forschungszentrum Jülich, un diagramme de phase complet des doublets de GRs a été établi en tenant compte de l'influence du réseau de spectrine. Des expériences ont permis de reproduire une variété de formes de ces doublets. Il a été prouvé que deux formes de doublets, le mâle-femelle et le sigmoïde-biconcave, facilitent la nucléation en agrégats plus grands.
Une autre série d'expériences a été réalisée sous flux. Le champ d'écoulement autour de chaque GR a été étudié. Des groupes de globules rouges formés de manière hydrodynamique ont été étudiés et ont révélé des applications possibles pour l'administration de médicaments. Des vortex ont été observés et caractérisés à l'aide de simulations 3D réalisées par l'université de Bayreuth. Nous avons montré que la période de rotation dans ces tourbillons suit une loi quasi-linéaire en fonction de la distance entre les globules rouges.
La formation de rouleaux dans la microcirculation est principalement due à des forces hydrodynamiques mais aussi, et surtout, à des forces d'adhésion. De plus, la contribution des forces hydrodynamiques et adhésives (induites par le Dextran) sur la désagrégation des agrégats sous flux a été explorée in-vitro, dans un réseau ramifié de bifurcations et dans une chambre d'écoulement. Elle a révélé une vitesse et un taux de cisaillement existants pour lesquels les forces adhésives disparaissent dans les capillaires à la fois dans le dextrane et le fibrinogène. Les rouleaux formés en présence de fibrinogène se sont révélés plus stables et on peut s'attendre à des énergies d'interaction plus fortes.
D'autres expériences visant à mieux comprendre et à démêler le mécanisme d'agrégation sont encore prévues. L'une d'entre elles consiste à utiliser des ponts spécifiques (DNA linkers). La (dés)agrégation des GRs pourrait être étudiée et comparée avec le dextran et le virus Fd (déplétant pur). L'objectif est de voir dans quelle mesure il pourrait être assimilé au plasma par la suite. Des expériences similaires ont déjà été réalisées dans le plasma autologue de la même manière que pour le dextran et le virus Fd. L'analyse de leurs courbes est encore en cours et une comparaison

directe avec les deux autres protagonistes (Fd et les lieurs d'ADN) pourrait faire la lumière sur les mécanismes sous-jacents de l'agrégation des globules rouges. En résumé, de nombreux aspects des propriétés physiques des globules rouges et leur influence sur l'agrégation ont été abordés dans cette thèse. Notre travail a montré que l'agrégation peut être plus complexe qu'il n'y paraît et les techniques détaillées dans ce travail sont de bons outils pour aborder les questions encore ouvertes.

Allgemeine Zusammenfassung und Perspektiven

Die in dieser Arbeit durchgeführte und vorgestellte Forschung ist interdisziplinär und verbindet die Hämatologie mit verschiedenen Bereichen der Physik. Basierend auf der Messung physikalischer Größen zur Beurteilung der physikalischen Eigenschaften des RB soll ein besseres Verständnis der RB-Interaktion erreicht werden. Das Hauptphänomen, das hier untersucht wird, ist die Aggregation von Erythrozyten im Rahmen von zwei verschiedenen Techniken: optische Pinzetten und Mikrofluidik.
Experimente auf Einzelzellebene ergaben, dass die Adsorption von Makromolekülen an der RB-Oberfläche unter raschem Wechsel des umgebenden Mediums erfolgt. Die in dieser Arbeit vorgestellte Technik erlaubt die Quantifizierung der adsorbierten Makromoleküle und könnte auch zur Quantifizierung der Adsorption von Plasmaproteinen verwendet werden.
Darüber hinaus untersuchten wir die (Dis-)Aggregation von mehreren RB-Paaren in verschiedenen Medien. Dextran wurde und wird immer noch zur Aufklärung der Aggregationsmechanismen verwendet. Unsere Arbeit zielte darauf ab, Dextran mit einem reinen Depletant (fd-Virus) zu vergleichen und zu zeigen, ob es zur Verifizierung des Depletionsmodells verwendet werden kann. Unsere Ergebnisse legen nahe, dass Dextran nicht als reines Depletant betrachtet werden kann. Wir fanden auch eine Diskrepanz in Bezug auf die gemessenen Kräfte. Die Aggregationskraft in Gegenwart von Dextran ist niedriger als die Disaggregationskraft. Im Gegenteil, die gemessenen Disaggregations- und Aggregationskräfte in Gegenwart eines reinen Depletants (fd-Virus) liegen in der gleichen Größenordnung.
Dank dreidimensionaler Simulationen, die am Forschungszentrum Jülich durchgeführt wurden, konnte unter Berücksichtigung des Einflusses des Spektrinnetzwerks ein vollständiges Phasendiagramm der RB-Dubletten erstellt werden. Experimente konnten eine Vielzahl dieser Dublettenformen reproduzieren. Zwei Dublettenformen, die männlich-weibliche und die sigmoid-bikonkave, erleichtern nachweislich die Nukleation zu größeren Aggregaten.

Eine weitere Reihe von Experimenten wurde unter Fluss durchgeführt. Das Strömungsfeld um einzelne Erythrozyten wurde untersucht. Hydrodynamisch gebildete Cluster von Erythrozyten wurden untersucht und mögliche Anwendungen für die Medikamentenverabreichung aufgezeigt. Es wurden Wirbel beobachtet und charakterisiert, die durch 3D-Simulationen der Universität Bayreuth unterstützt wurden. Wir zeigten, dass die Rotationsperiode in diesen Wirbeln einem quasilinearen Gesetz als Funktion des Abstands zwischen den roten Blutkörperchen folgt.
Die Bildung von Rouleaux in der Mikrozirkulation ist hauptsächlich auf hydrodynamische Kräfte, aber vor allem auch auf Adhäsionskräfte zurückzuführen. Darüber hinaus wurde der Beitrag von hydrodynamischen Kräften und Adhäsionskräften (induziert durch Dextran) auf die Disaggregation von Aggregaten unter Strömung in vitro, in einem verzweigten Netz von Verzweigungen und in einer Strömungskammer untersucht. Dabei wurde eine vorhandene Geschwindigkeit und Scherrate festgestellt, bei der die Adhäsionskräfte in den Kapillaren sowohl in Dextran als auch in Fibrinogen verschwinden. In Gegenwart von Fibrinogen gebildete Rouleaux haben sich als stabiler erwiesen und es ist zu erwarten, dass sie stärkere Interaktionsenergien aufweisen.
Weitere Experimente zum besseren Verständnis und zur Aufklärung des Aggregationsmechanismus sind noch geplant. Eines davon besteht in der Verwendung spezifischer Brückenbilder (DNA-Linker). Die (Dis-)Aggregation von RB könnte untersucht und mit Dextran und fd-Virus (reines Depletant) verglichen werden. Ziel ist es, herauszufinden, inwieweit es später in Plasma assimiliert werden könnte. Ähnliche Experimente mit autologem Plasma wurden bereits auf die gleiche Weise wie für Dextran und fd-Virus durchgeführt. Die Analyse die Daten ist noch im Gange, und ein direkter Vergleich mit den beiden anderen Protagonisten (Fd und DNA-Linker) könnte Aufschluss über die zugrunde liegenden Mechanismen der RB-Aggregation geben. Zusammengefasst wurden in dieser Arbeit viele Aspekte der physikalischen Eigenschaften von RB und deren Einfluss auf die Aggregation diskutiert. Unsere Arbeit zeigte, dass die Aggregation komplexer sein kann, als es den Anschein hat, und die in dieser Arbeit beschriebenen Techniken sind gute Werkzeuge, um die noch offenen Fragen anzugehen.

List of publications

M. Hoore, **F. Yaya**, T. Podgorski, C. Wagner, G. Gompper and D.A. Fedosov. "Effect of spectrin network elasticity on the shapes of erythrocyte doublets". Soft Matter, 2018, 14 (30), pp. 6278-6289.

K. Lee, E. Shirshin, N. Rovnyagina, **F. Yaya**, Z. Boujja, A. Priezzhev and C. Wagner. "Dextran adsorption onto red blood cells revisited: single cell quantification by laser tweezers combined with microfluidics". Biomed. Opt. Express, 2018, 9 (6), pp. 2755-2764.

P. Ermolinskiy, A. Lugovtsov, **F. Yaya**, K. Lee, C. Wagner and A. Priezzhev. "Effect of Red Blood Cell Aging in vivo on their Aggregation Properties in vitro: Measurements with Laser Tweezers". App. Sci, 2020, 10 (21), pp. 7581.

F. Yaya, J. Römer, A. Guckenberger, T. John, S. Gekle, T. Podgorski and C. Wagner. "Vortical flows induced by red blood cells". *Accepted in Microcirc.*, 2021.

A. Darras, K. Peikert, A. Rabe, **F. Yaya**, G. Simionato, T. John, A.K. Dasanna, S. Buvalyy, J. Geise, A. Hermann, D.A. Fedosov, A. Danek, C. Wagner and L. Kaestner. "Erythrocyte sedimentation rate as a new diagnostic biomarker for neuroacanthocytosis syndromes". *Accepted in Cells*, 2021.

F. Yaya, O. Korculanin, M. Babaki, C. Wagner, P. Lettinga and K. Lee "Unravelling the red blood cells aggregation mechanism". *In preparation*.

Bibliography

[1] O. K. Baskurt et al. “Comparison of three instruments for measuring red blood cell aggregation”. In: *Clin. Hemorheol. Microcirc.* 43 (4 2009), pp. 283–298.

[2] P Cabrales, A.G. Tsai, and M. Intaglietta. “Microvascular pressure and functional capillary density in extreme hemodilution with low- and high-viscosity dextran and a low-viscosity Hb-based O2 carrier”. In: *Am J Physiol Heart Circ Physiol.* 287 (1 2004), H363–H373.

[3] L. L. Munn and M. M. Dupin. “Blood Cell Interactions and Segregation in Flow”. In: *Ann. Biomed. Eng.* 36 (4 2008), pp. 534–544.

[4] S.N. Balaji and V. Trivedi. “Extracellular methemoglobin primes red blood cell aggregation in malaria: An in vitro mechanistic study”. In: *FEBS Lett.* 587 (4 2013), pp. 350–357.

[5] A.M. Dondorp et al. “Abnormal blood flow and red blood cell deformability in severe malaria”. In: *Parasitol Today* 16 (7 2000), p. 272.

[6] H. Schmid-Schonbein and E. Volger. “Red-cell aggregation and red-cell deformability in diabetes”. In: *Diabetes* 25.2 SUPPL (1976), 897—902.

[7] R.M. Bauersachs et al. “Red blood cell aggregation and blood viscoelasticity in poorly controlled Type 2 diabetes mellitus”. In: *Clin. Hemorheol. Microcirc.* 9.6 (1989), pp. 935–952.

[8] P. Connes et al. “Blood rheological abnormalities in sickle cell anemia”. In: *Clin. Hemorheol. Microcirc.* 68 (2-3 2018), pp. 165–172.

[9] J. Tripette et al. “Red blood cell aggregation, aggregate strength and oxygen transport potential of blood ar abnormal in both homozygous sickle cell anemia and sickle-hemoglobin C disease”. In: *Haematologica* 94 (8 2009), pp. 1060–1065.

[10] D. Davalos and K. Akassoglou. “Fibrinogen as a key regulator of inflammation in disease”. In: *Semin. Immunopathol.* 34 (2012), pp. 43–62.

[11] R. Fahraeus. “The suspension stability of the blood”. In: *Physiological Reviews* 9 (2 1929), pp. 241–274.

[12] D. Flormann et al. “The buckling instability of aggregating red blood cells”. In: *Sci. Rep.* 7 (1 2017), p. 7928.

[13] O. K. Baskurt and M. Funda. “Importance of measurement temperature in detecting the alterations of red blood cell aggregation and deformability studied by ektacytometry: A study on experimental sepsis in rats”. In: *Clin. Hemorheol. Microcirc.* 23 (1 2000), pp. 43–49.

[14] M.R. Hardeman et al. “Laser-assisted optical rotational cell analyser (L.O.R.C.A.); I. A new instrument for measurement of various structural hemorheological parameters”. In: *Clin. Hemorheol. Microcirc.* 14 (4 1994), pp. 605–618.

[15] K.M. Jan and S. Chien. “Role of surface electric charge in red blood cell interactions”. In: *J. Gen. Phys.* 61.5 (1973), pp. 638–654.

[16] M. Boynard and J.C. Lelievre. “Size determination of red blood cell aggregates induced by dextran using ultrasound backscattering phenomenon”. In: *Biorheology* 27 (1 1990), pp. 39–46.

[17] S. Shin et al. “Slit-flow ektacytometry: Laser diffraction in a slit rheometer”. In: *Cytom. Part B-Clin Cy* 65B (1 2005), pp. 6–13.

[18] S. Shin, J.X. Hou, and M. Singh. “Validation and application of a microfluidic ektacytometer (Rheoscan-D) in measuring erythrocyte deformability”. In: *Clin. Hemorheol. Microcirc.* 37 (2007), pp. 319–328.

[19] E. Franceschini, F.T.H. Yu, and G. Cloutier. “Simultaneous estimation of attenuation and structure parameters of aggregated red blood cells from backscatter measurements”. In: *J. Acoust. Soc. Amer.* 123 (2008), EL85–91.

[20] E. Franceschini et al. “Ultrasound characterization of red blood cell aggregation with intervening attenuating tissue-mimicking phantoms”. In: *J. Acoust. Soc. Amer.* 127.2 (2020), pp. 1104–1115.

[21] P. Steffen, C. Verdier, and C. Wagner. “Quantification of Depletion-Induced Adhesion of Red Blood Cells”. In: *Phys. Rev. Lett.* 110 (2013), p. 018102.

[22] D. Flormann. “Physical charaterization of red blood cell aggregation”. Doctoral thesis. NT Physik, 2017.

[23] A. Tozeren, K.L.P. Sung, and S. Chien. “Theoretical and Experimental Studies on Crossbridge Migration During Cell Disaggregation”. In: *Biophys. J.* 55 (3 1989), pp. 479–87.

[24] K. Buxbaum, E. Evans, and D.E. Brooks. “Quantitation of surface affinities of red blood cells in dextran solutions and plasma”. In: *Biochemistry* 21 (13 1982), pp. 3235–3239.

[25] S. Chien et al. "Energy balance in red cell interactions". In: *Ann. N.Y. Acad. Sci.* 416 (1983), pp. 190–206.

[26] R. Ben-Ami et al. "A synergistic effect of albumin and fibrinogen on immunoglobulin-induced red blood cell aggregation". In: *Am. J. Physiol. Heart. Circ. Physiol.* 285 (2003), pp. 2663–2669.

[27] R. Skalak and S. Chien. "Theoretical models of rouleau formation and disaggregation". In: *Ann. N.Y. Acad. Sci.* 416 (1983), pp. 138–148.

[28] J. Janzen and D.E. Brooks. *A critical reevaluation of the nonspecific adsorption of plasma proteins and dextrans to erythrocytes and the role of these in rouleaux formation. In Interfacial Phenomena in Biological Systems*. M. Bender, 1991.

[29] B. Neu and H.J Meiselman. "Depletion-mediated red blood cell aggregation in polymer solutions". In: *Biophys. J.* 83.5 (2002), pp. 2482–2490.

[30] K. Lee et al. "Optical tweezers study of red blood cell aggregation and disaggregation in plasma and protein solutions". In: *J. Biomed. Opt.* 21.3 (2016), p. 035001.

[31] A. Hoffmann et al. "Optical tweezers for confocal microscopy". In: *Appl Phys B* 71 (2000), 747–753.

[32] Kun Chen et al. "Diagnosis of colorectal cancer using Raman spectroscopy of laser-trapped single living epithelial cells". In: *Opt. Lett.* 31.13 (2006), pp. 2015–2017.

[33] C. Battle, L. Lautscham, and C.F. Schmidt. "Differential interference contrast microscopy using light-emitting diode illumination in conjunction with dual optical traps". In: *Rev. Scient. Instr.* 84 (2013), p. 053703.

[34] A. Y. Maklygin et al. "Measurement of interaction forces between red blood cells in aggregates by optical tweezers". In: *Quantum Electron.* 42 (6 2003), 500–504.

[35] Maria D. Khokhlova et al. "Peculiarities of RBC aggregation studied by double trap optical tweezers". In: *Biophotonics: Photonic Solutions for Better Health Care II*. Ed. by Jurgen Popp et al. Vol. 7715. International Society for Optics and Photonics. SPIE, 2010, pp. 116 –123.

[36] O. Aouane. "Modeling and simulation of the motion of deformable interfaces in a confined geometry : application to the study of the flow of red blood cells in microcirculation". Doctoral thesis. NT Physik, 2015.

[37] Z. Boujja. “Simulation of Red Blood Cells in Microcapillaries: On the Study of a Deformable Particle in Steady and Oscillating Poiseuille Flow”. Doctoral thesis. NT Physik, 2019.

[38] N. Tahiri et al. “Rheology of a vesicle suspension with finite concetration: A numerical study”. In: *Microvasc. Res.* 85 (2013), pp. 40–45.

[39] B. Kaoui et al. “Complexity of vesicle microcirculation”. In: *Phys. Rev. E* 84 (2011), p. 041906.

[40] M. Thiebaud and C. Misbah. “Rheology of a vesicle suspension with finite concentration: A numerical study”. In: *Phys. Rev. E* 88 (6 2013), p. 062707.

[41] D.A. Fedosov, M. Peltomäki, and G. Gompper. “Deformation and dynamics of red blood cells in flow through cylindrical microchannels”. In: *Soft Matter* 10 (24 2014), pp. 4258–4267.

[42] A. Kihm et al. “Classification of red blood cell shapes in flow using outlier tolerant machine learning”. In: *PLoS Comput. Biol.* 14.6 (2018), e1006278.

[43] A. Guckenberger et al. “Numerical-experimental observation of shape bistability of red blood cells flowing in a microchannel”. In: *Soft Matter* 14 (2018), p. 2032.

[44] P. Gaehtgens, C. Dührssen, and K.H. Albrecht. “Motion, deformation, and interaction of blood cells and plasma during flow through narrow capillary tubes.” In: *Blood Cells* 6.4 (1980), p. 799.

[45] V. Claveria et al. “Clusters of red blood cells in microcapillary flow: hydrodynamic versus macromolecule induced interaction”. In: *Soft Matter* 12 (2016), p. 8235.

[46] T.M. Fischer et al. “The stress-free shape of the red blood cell membrane”. In: *Biophys. J.* 34 (3 1981), pp. 409–422.

[47] E.A. Evans and Fung. “Improved measurements of the erythrocyte geometry”. In: *Microvasc. res.* 4 (1972), pp. 335–347.

[48] R.R. Hantgan et al. *Hemostasis and Thrombosis: Basic Principles and Clinical Practice*. Lippincott Williams and Wilkins, Philadelphia, PA, 2001, pp. 203–232.

[49] X. Weng et al. “Comparison and simulation of different levels of erythrocyte aggregation with pig, horse, sheep, calf, and normal human blood”. In: *Biorheology* 33 (4-5 1996), pp. 365–377.

[50] R. Plasenzotti et al. "Red blood cell deformability and aggregation behaviour in different animal species". In: *Clin. Hemorheol. Microcirc.* 31 (2004), pp. 105–111.

[51] L.O. Lamke and S.O. Liljedahl. "Plasma volume changes after infusion of various plasma expanders". In: *Resuscitation* 5 (2 1976), pp. 93–101.

[52] K. Lin et al. "Colloidal interactions in suspensions of rods". In: *Phys. Rev. Lett.* 87 (2001), p. 088301.

[53] A. Stroobants, H.N.W. Lekkerkerker, and T. Odjik. "Effect of electrostatic interaction on the liquid crystal phase transition in solutions of rodlike polyelectrolytes". In: *Macromolecules* 19 (8 1986), pp. 2232–2238.

[54] J. Newman, H.L. Swinney, and L.A. Day. "Hydrodynamic properties and structure of fd virus". In: *J. Mol. Biol.* 116 (3 1977), pp. 593–603.

[55] D.C. Prieve. "Measurement of colloidal forces with TIRM". In: *Adv. Colloid Interface Sci.* 82 (1-3 1999), pp. 93–125.

[56] P. Holmqvist, D. Kleshchanok, and P.R. Lang. "Interaction potential and near wall dynamics of spherical colloids in suspensions of rod-like fd-virus". In: *Eur. Phys. J. E.* 26 (1-2 2008), pp. 177–182.

[57] Christian Lang et al. "Effects of particle stiffness on the extensional rheology of model rod-like nanoparticle suspensions". In: *Soft Matter* 15 (Nov. 2018).

[58] B. Neu, R. Wenby, and H.J. Meiselman. "Effects of dextran molecular weight on red blood cell aggregation". In: *Biophys. J.* 95 (6 2008), 3059–3065.

[59] Shu Chien and Kung ming Jan. "Ultrastructural basis of the mechanism of rouleaux formation". In: *Microvasc. Res.* 5.2 (1973), pp. 155 –166. ISSN: 0026-2862.

[60] S. Chien and KM. Jan. "Red cell aggregation by macromolecules: Roles of surface adsorption and electrostatic repulsion". In: *J. Supramol. Struct.* 1 (4-5 1973), pp. 385–409.

[61] S. Chien. "Electrochemical interactions between erythrocyte surfaces". In: *Thromb. Res.* 8 (Supp.2 1976), pp. 189–202.

[62] Shu Chien et al. "Surface adsorption of dextrans on human red cell membrane". In: *J. Colloid Interface Sci.* 62.3 (1977), pp. 461 –470. ISSN: 0021-9797.

[63] E.H. Eylar et al. "The contribution of sialic acid to the surface charge of the erythrocyte". In: *J. Biol. Chem* 237 (6 1962), pp. 1992–2000.

[64] P. Bagchi, P.C. Johnson, and A.S. Popel. "Computational fluid dynamic simulation of aggregation of deformable cells in a shear flow". In: *Biochem. Eng. J.* 127 (2005), pp. 1070–1080.

[65] V. Schechner et al. "Significant dominance of fibrinogen over immunoglobulins, C-reactive protein, cholesterol and triglycerides in maintaining increased red blood cell adhesiveness/aggregation in the peripheral venous blood: a model in hypercholesterolaemic patients." In: *Eur. J. Clin. Invest.* 33 (11 2003), pp. 955–961.

[66] E.W. Merrill et al. "Effect of fibrinogen deduced by addition". In: *Circ. Res.* 18 (4 1966), pp. 437–446.

[67] Nobuji Maeda et al. "Fibrinogen-induced erythrocyte aggregation: erythrocyte-binding site in the fibrinogen molecule". In: *Biochim. Biophys. Acta Biomembr.* 904.1 (1987), pp. 81 –91. ISSN: 0005-2736.

[68] D. Lominadze and W.L. Dean. "Involvement of fibrinogen specific binding in erythrocyte aggregation". In: *FEBS Lett.* 517 (1-3 2002), pp. 41–44.

[69] I. A. Sokolova et al. "An effect of glycoprotein IIb/IIIa inhibitors on the kinetics of red blood cells aggregation". In: *Clin. Hemorheol. Microcirc.* 57 (3 2014), pp. 291–302.

[70] M. Dembo et al. "The reaction-limited kinetics of membrane-to-surface adhesion and detachment". In: *Proc. R. Soc. Lond. B. Biol. Sci.* 234 (1274 1988), pp. 55–83.

[71] Y.V. Pereverzev et al. "The Two-Pathway Model for the Catch-Slip Transition in Biological Adhesion". In: *Biophys. J.* 89 (3 2005), pp. 1446–1454.

[72] S. Asakura and F. Oosawa. "Interaction between particles suspended in solutions of macromolecules". In: *J. Polym. Sci.* 33 (126 1958), pp. 183–192.

[73] Bronkhorst P.J et al. "The mechanism of red cell (dis)aggregation investigated by means of direct cell manipulation using multiple optical trapping". In: *Br. J. Haematol.* 96.2 (1997), pp. 256–258.

[74] Marko Mravlak. "Depletion force". In: *Seminar*. 2008.

[75] B. Vincent et al. "Depletion flocculation in dispersions of sterically-stabilised particles ("soft spheres")". In: *Colloids Surf. A* 18 (2-4 1986), pp. 261–281.

[76] Z. Dogic et al. "Isotropic-nematic phase transition in suspensions of filamentous virus and the neutral polymer Dextran". In: *Phys.l Rev. E* 69 (Pt.1 2004), p. 051702.

[77] A.P. Chatterjee and K.S. Schweizer. "Correlation effects in dilute particle-polymer mixtures". In: *J. Chem. Phys.* 109 (23 1998), pp. 10477–10488.

[78] E. Eisenriegler. "Universal density-force relations for polymers near a repulsive wall". In: *Phys. Rev. E* 55 (Supp.B 1997), pp. 3116–3123.

[79] H.N.W. Lekkerkerker and R. Tuinier. *Colloids and the Depletion Interaction*. Springer, 2011.

[80] O. Baskurt, B. Neu, and H.J. Meiselman. *Theoretical microfluidics*. CRC Press, 2012.

[81] D Kuzman et al. "Effect of pH on red blood cell deformability". In: *Eur. J. Appl. Physiol.* 440.5 (2000), R193–4.

[82] L.E.Göran Eriksson. "On the shape of human red blood cells interacting with flat artificial surfaces — the 'glass effect'". In: *BBA-Gen. Subjects* 1036.3 (1990), pp. 193 –201. ISSN: 0304-4165.

[83] t. Hovav et al. "Alteration of red cell aggregability and shape during blood storage". In: *Transfusion* 39 (3 1999), pp. 277–281.

[84] J.R. Hess. "Conventional blood banking and blood component storage regulation: opportunities for improvement". In: *J. Blood Transfus.* 8 (Supp. 3 2010), s9–s15.

[85] M. Uyuklu et al. "Effects of storage duration and temperature of human blood on red cell deformability and aggregation". In: *Pflügers Arch.* 41 (4 2009), pp. 269–278.

[86] A. Ashkin. "Acceleration and Trapping of Particles by Radiation Pressure". In: *Phys. Rev. Lett.* 24 (4 1970), pp. 156–159.

[87] A. Ashkin et al. "Observation of a Single-Beam gradient Force Optical Trap for Dielectric Particles". In: *Opt. Lett.* 11 (1986), pp. 288–290.

[88] Y. Tadir et al. "Micromanipulation of sperm by a laser generated optical trap". In: *Fertil. Steril.* 52 (1989), pp. 870–873.

[89] E.M. Bonder et al. "Force production by swimming sperm-analysis using optical tweezers". In: *Int. J. Cell Biol.* 111 (1990), 421A.

[90] S.M. Block, D.F. Blair, and H.C. Berg. "Compliance of bacterial flagella measured with optical tweezers". In: *Nature(Lond.)* 338 (1989), pp. 514–518.

[91] A. Ashkin and J.M. Dziedzic. "Optical trapping and manipulation of viruses and bacteria". In: *Science* 235 (1987), pp. 1517–1520.

[92] A. Ashkin and J.M. Dziedzic. "Optical levitation by radiation pressure". In: *App. Phys. Lett.* 19 (1971), pp. 283–285.

[93] A. Ashkin and J.M. Dziedzic. "Optical levitation of liquid drops by radiation pressure". In: *Science* 187 (1975), pp. 1073–1075.

[94] K. D. Wulff et al. "Aberration correction in holographic optical tweezers". In: *Opt. Express* 14 (9 2014), pp. 4169–4174.

[95] M. Dienerowitz et al. "Holographic aberration correction: optimising the stiffness of an optical trap deep in the sample". In: *Opt. Express* 19 (24 2011), pp. 24589–24595.

[96] R.W. Gerchberg and W.O Saxton. "A practical algorithm for the determination of the phase from image and diffraction plane pictures". In: *Optik* 35 (1972), pp. 237–246.

[97] K. Svoboda and S.M. Block. "Biological Applications of Optical Forces". In: *Annu. Rev. Biophys. Biomol. Struct.* 23 (1994), pp. 247–285.

[98] H. Felgner, O. Muller, and M. Schliwa. "Calibration of light forces in optical tweezers". In: *App. Opt.* 34 (6 1995), pp. 977–982.

[99] Tolic-Nørrelykke I.M., K. Berg-Sørensen, and H. Flyvbjerg. "MatLab program for precision calibration of optical tweezers". In: *Comput. Phys. Commun.* 159 (3 2004), pp. 225–240.

[100] W. Singer et al. "Three-dimensional force calibration of optical tweezers". In: *J. Mod. Opt.* 47 (14-15 2000), pp. 2921–2931.

[101] J.T. Kuenstner and Norris K.H. "Spectrophotometry of Human Hemoglobin in the near Infrared Region from 1000 to 2500 nm". In: *J. Near Infrared Spec.* 2 (2 1994), pp. 59–65.

[102] C.K. Chow and T. Kaneko. *Boundary detection of radiographic images by a thresholding method*. Academic Press, New York, 1972, pp. 61–82.

[103] J.S. Weszka, R.N. Nagel, and A. Rosenfeld. "A threshold selection technique". In: *IEEE Trans. on Comput.* C-23 (1974), pp. 1322–1326.

[104] J. Matas et al. "Robust wide-baseline stereo from maximally stable extremal regions". In: *Image and Vision Comput.* 22 (10 2004), pp. 761–767.

[105] R.L. Kettig and D.A. Landgrebe. "Classification of multispectral image data by extraction of homogeneous objects". In: *IEEE Trans. Geosci. Remote Sens.* GE-14 (1 1976), pp. 19–26.

[106] A. Klinger. "Data structures and pattern recognition". In: *Proceedings of the First International Joint Conference on Pattern Recognition, Washington* (1973), pp. 497–498.

[107] N. Otsu. "A threshold selection method from gray-level histograms". In: *IEEE Transactions on Systems, Man and Cybernetics* 9 (1 1979), pp. 62–66.

[108] K. Lee et al. "Dextran adsorption onto red blood cells revisited: single cell quantification by laser tweezers combined with microfluidics". In: *Biomed. Opt. Express* 9 (6 2018), pp. 2755–2764.

[109] A. Cudd et al. "Dextran protection of erythrocytes from low-pH-induced hemolysis". In: *FEBS Lett.* 250 (2 1989), 293–296.

[110] D.E. Brooks. "The effect of neutral polymers on the electrokinetic potential of cells and other charged particles: III. Experimental studies on the dextran/erythrocyte system". In: *J. Colloid Interface Sci.* 43 (3 1973), 700–713.

[111] F.J. Alvarez et al. "Behaviour of isolated rat and human red blood cells upon hypotonic-dialysis encapsulation of carbonic anhydrase and dextran". In: *Biotechnol. Appl. Biochem.* 23 (Pt2 1996), 173–179.

[112] K. Lee, C. Wagner, and A.V. Priezzhev. "Assessment of the cross-bridge induced interaction of red blood cells by optical trapping combined with microfluidics". In: *J. Biomed. opt.* 22 (9 2017), p. 091516.

[113] K. Baskurt and H.J. Meiselman. "Erythrocyte aggregation: basic aspects and clinical importance". In: *Clin. Hemorheol. Microcirc.* 53 (1-2 2013), pp. 23–37.

[114] D. Guu et al. "Depletion induced clustering in mixtures of colloidal spheres and fd-virus". In: *J. Condens. Matter Phys.* 24.46 (2012), p. 464101.

[115] S. Rad, H. Meiselman, and B. Neu. "Impact of glycocalyx structure on red cell-red cell affinity in polymer suspensions". In: *Colloids Surf. B* 123 (2014).

[116] M. Hoore et al. "Effect of spectrin network elasticity on the shapes of erythrocyte doublets". In: *Soft Matter* 14 (30 2018), pp. 6278–6289.

[117] R. Skalak et al. "Mechanics of rouleau formation". In: *Biophys.l J.* 35 (3 1981), pp. 771–781.

[118] P. Ziherl and S. Svetina. "Flat and sigmoidally curved contact zones in vesicle–vesicle adhesion". In: *PNAS* 104 (3 2007), pp. 761–765.

[119] S. Svetina and P. Ziherl. "Morphology of small Aggregates of Red Blood Cells". In: *Bioelectrochemistry* 73 (2 2008), pp. 84–91.

[120] D. Yoon and D. You. "Continuum Modeling of Deformation and Aggregation of Red Blood Cells". In: *J. Biomech.* 49 (11 2016), pp. 2267–2279.

[121] M.A Peterson. "Linear response of the human erythrocyte to mechanical stress". In: *Phys. Rev. A* 45 (6 1992), pp. 1289–1294.

[122] Y. Park et al. "Dynamics of blood cell suspensions in microflows". In: *PNAS* 107 (11 2017), pp. 2865–2870.

[123] B. Evans A.A. Bhaduri, G. Popescu, and A.J. Levine. "Geometric localization of thermal fluctuations in red blood cells". In: *PNAS* 114 (11 2017), pp. 2865–2870.

[124] O.K. Baskurt et al. "New Guidelines for Hemorheological Laboratory Techniques". In: *Clin. Hemorheol. Microcirc.* 42 (2 2009), pp. 75–97.

[125] M. Brust et al. "The plasma protein fibrinogen stabilizes clusters of red blood cells in microcapillary flows". In: *Sci. Rep.* 4 (2014), p. 4348.

[126] D.A. Fedosov, B. Caswell, and G.E. Karniadakis. "A multiscale red blood cell model with accurate mechanics, rheology, and dynamics". In: *Biophys J.* 98.10 (2010), pp. 2215–25.

[127] S. Suresh et al. "Connections Between Single-Cell Biomechanics and Human Disease States: Gastrointestinal Cancer and Malaria". In: *Acta Biomater.* 1 (1 2005), pp. 15–30.

[128] S. Henon et al. "A new determination of the shear modulus of the human erythrocyte membrane using optical tweezers". In: *Biophys. J.* 76 (2 1999), pp. 1145–1151.

[129] M. Puig-de Morales-Marinkovic et al. "Viscoelasticity of the human red blood cell". In: *Am. J. Physiol. Cell Physiol.* 293 (2007), pp. C597–C605.

[130] R. Waugh and E.A. Evans. "Thermoelasticity of red blood cell membrane". In: *Biophys. J.* 26 (1), pp. 115–131.

[131] T. Svelc and S. Svetina. "Stress-free state of the red blood cell membrane and the deformation of its skeleton". In: *Cell and Mol. Bio. Lett.* 17 (0).

[132] D. Cordasco, Y. Alireza, and P. Bagchi. "Comparison of erythrocyte dynamics in shear flow under different stress-free configurations". In: *Phys. of Fluids* 26 (2014), p. 041902.

[133] B. Daily, E.L. Elson, and G. I. Zahalak. "Cell poking. Determination of the elastic area compressibility modulus of the erythrocyte membrane". In: *Biophys. J.* 45 (4 1984), pp. 671–682.

[134] P.B. Canham. "The minimum energy of bending as a possible explanation of the biconcave shape of the human red blood cell". In: *J. Theor. Biol.* 26 (1 1970), pp. 61–81.

[135] E.W. Merrill et al. "Rheology of human blood, near and at zero flow: Effects of temperature and hematocrit level". In: *Biophys. J.* 3 (3 1963), pp. 199–213.

[136] R. Skalak, S.R. Keller, and T.W. Secomb. "Mechanics of blood flows". In: *J. Biomech. Eng.* 103 (1981), pp. 102–115.

[137] S. Chien et al. "Effects of Hematocrit and Plasma Proteins on Human Blood Rheology at Low Shear Rates". In: *J. Appl. Physiol* 21 (1 1966), pp. 81–87.

[138] R.W. Samsel and A.S. Perelson. "Kinetics of Rouleau Formation. II. Reversible Reactions". In: *Biophys. J.* 45 (4 1984), pp. 805–824.

[139] F. Yaya et al. "Vortical flows induced by red blood cells". In: *Submitted in Microcirc.* - (2020), pp. –.

[140] N. Takeishi and Y. Imai. "Capture of microparticles by bolus flow of red blood cells in capillaries". In: *Sci. Rep.* 7.5381 (2017).

[141] Petia M Vlahovska, Dominique Barthès-Biesel, and Chaouqi Misbah. "Flow dynamics of red blood cells and their biomimetic counterparts". In: *C. R. Physique* 14.6 (July 2013), pp. 451–458.

[142] J.B. Freund. "Numerical Simulation of Flowing Blood Cells". In: *Annu. Rev. Fluid Mech.* 46 (2014), p. 67.

[143] Timothy W Secomb. "Blood Flow in the Microcirculation". In: *Annu. Rev. Fluid Mech.* 49.1 (Jan. 2017), pp. 443–461.

[144] M.M. Guest et al. "Red blood cells: change in shape in capillaries". In: *Science* 142.3597 (1963), p. 1319.

[145] Giovanna Tomaiuolo et al. "Red blood cell deformation in microconfined flow". In: *Soft Matter* 5.19 (2009), p. 3736.

[146] S Quint et al. "3D tomography of cells in micro-channels". In: *Appl. Phys. Lett.* 111.10 (Sept. 2017), pp. 103701–4.

[147] Hiroshi Noguchi and Gerhard Gompper. "Shape transitions of fluid vesicles and red blood cells in capillary flows". In: *PNAS* 102.40 (2005), p. 14159.

[148] Lingling Shi, Tsorng-Whay Pan, and Roland Glowinski. "Deformation of a single red blood cell in bounded Poiseuille flows". In: *Phys. Rev. E* 85.1 (Jan. 2012), pp. 016307–15.

[149] N Tahiri et al. "On the problem of slipper shapes of red blood cells in the microvasculature". In: *Microvasc. Res.* 85.C (Jan. 2013), pp. 40–45.

[150] Guillermo R Lázaro, Aurora Hernández-Machado, and Ignacio Pagonabarraga. "Rheology of red blood cells under flow in highly confined microchannels: I. effect of elasticity". In: *Soft Matter* 10.37 (June 2014), pp. 7195–12.

[151] L. Lanotte et al. "Red Cells' Dynamic Morphologies Govern Blood Shear Thinning Under Microcirculatory Flow Conditions". In: *Proc Natl Acad Sci U S A* 113 (47 2016), pp. 13289–13294.

[152] Ting Ye et al. "Numerical studies of a red blood cell in rectangular microchannels". In: *J. Appl. Phys.* 122.8 (Aug. 2017), pp. 084701–11.

[153] Felix Reichel et al. "High-Throughput Microfluidic Characterization of Erythrocyte Shapes and Mechanical Variability". In: *Biophys. J.* 117.1 (July 2019), pp. 14–24.

[154] Naoki Takeishi et al. "Haemorheology in dilute, semi-dilute and dense suspensions of red blood cells". In: *J. Fluid Mech.* 872 (Aug. 2019), pp. 818–848.

[155] J. Liam McWhirter, Hiroshi Noguchi, and Gerhard Gompper. "Flow-induced clustering and alignment of vesicles and red blood cells in microcapillaries". In: *PNAS* 106.15 (2009), p. 6039.

[156] J. L. McWhirther, H. Noguchi, and G. Gompper. "Deformation and clustering of red blood cells in microcapillary flows". In: *Soft Matter* 7 (2011), pp. 10967–10977.

[157] G. Tomaiuolo et al. "Red blood cell clustering in Poiseuille microcapillary flow". In: *Phys. of Fluids* 24.051903 (5 2012).

[158] G. Ghigliotti et al. "Why and how does collective red blood cells motion occur in the blood microcirculation". In: *Phys. Fluids* 24.10 (2012), p. 101901.

[159] O Aouane et al. "Hydrodynamic pairing of soft particles in a confined flow". In: *Phys. Rev. Fluids* 2.6 (June 2017), pp. 063102–21.

[160] H.S. Lew and Y.C. Fung. "The motion of the plasma between the red cells in the bolus flow". In: *Biorheology* 6 (2 1969), p. 109.

[161] Edgar E Nanne, Christian P Aucoin, and Edward F Leonard. "Molecular movement of bovine albumin in flowing suspensions of bovineerythrocytes". In: *Chem. Eng. Sci.* 65.24 (Dec. 2010), pp. 6389–6396.

[162] Randall Toy et al. "The effects of particle size, density and shape on margination of nanoparticles in microcirculation". In: *Nanotechnology* 22.11 (Feb. 2011), p. 115101.

[163] Tae-Rin Lee et al. "On the near-wall accumulation of injectable particles in the microcirculation: smaller is not better". In: *Sci. Rep.* 3 (June 2013), p. 2079.

[164] Hengdi Zhang and Chaouqi Misbah. "Lattice Boltzmann Simulation of Advection-Diffusion of Chemicals and Applications to Blood Flow". In: *Comput. Fluids* 187 (2019), pp. 1–62.

[165] Z Liu et al. "A unified analysis of nano-to-microscale particle dispersion in tubular blood flow". In: *Phys. Fluids* 31.8 (Aug. 2019), pp. 081903–11.

[166] Zixiang Liu et al. "Nanoparticle diffusion in sheared cellular blood flow". In: *J. Fluid Mech.* 871 (July 2019), pp. 636–667.

[167] J. Prothero and A.C. Burton. "The Physics of Blood Flow in Capillaries: I. The Nature of the Motion". In: *Biophys. J.* 1 (7 1961), p. 565.

[168] H. Amini, W. Lee, and D. Di Carlo. "Inertial microfluidic physics". In: *Lab Chip* 14 (2014), p. 2739.

[169] M. Zurita-Gotor, J. Blawzdziewicz, and E. Wajnryb. "Swapping trajectories: a new wall-induced cross-streamline particle migration mechanism in a dilute suspension of spheres". In: *J. Fluid Mech.* 592 (2007), pp. 447–469.

[170] W. Lee et al. "Dynamic self-assembly and control of microfluidic particle crystals". In: *PNAS* 28 (2013), pp. 22413–22418.

[171] T. Ohmura et al. "Oscillation and collective conveyance of water-in-oil droplets by microfluidic bolus flow". In: *Appl. Phys. Lett.* 107 (2015), p. 074102.

[172] Y. Shin et al. "Microfluidic assay for simultaneous culture of multiple cell types on surfaces or within hydrogels". In: *Nat. Protoc.* 7 (2012), p. 1247.

[173] S. Kim and S.J. Karrila. *Microhydrodynamics*. Dover, 2005.

[174] C. Pozrikidis. "Boundary Integral and singularity methods for linearized flow". In: *Cambridge University Press* (1992).

[175] A. Guckenberger et al. "On the bending algorithm for soft objects in flows". In: *Comput. Phys. Commun.* 207 (2016), p. 1.

[176] A. Guckenberger and S. Gekle. "Theory and algorithms to compute Helfrich bending forces: a review". In: *J. Phys. Cond. Mat.* 29.20 (2017), p. 203001.

[177] H. Bruus. *Theoretical microfluidics*. Oxford University Press, 2007.

[178] H.C. Kuhlmann and F. Romano. *Computational Modelling of Bifurcations and Instabilities in Fluid Dynamics*. Springer, 2018.

[179] A.R. Pries et al. "Red cell distribution at microvascular bifurcations". In: *Microvasc. Res.* 38 (1989), pp. 81–101.

[180] E. Kaliviotis, J. Sherwood, and S. Balabani. "Partitioning of red blood cell aggregates in bifurcating microscale flows". In: *Sci. Rep.* 7 (2017), p. 44563.

[181] J.M. Sherwood et al. "The effect of red blood cell aggregation on velocity and cell-depleted layer characteristics of blood in a bifurcating microchannel". In: *Biomicrofluidics* 6 (2012), p. 024119.

[182] Z. Shen et al. "Inversion of hematocrit partition at microfluidic bifurcations". In: *Microvasc. Res.* 105 (2016), pp. 40–46.

[183] P. Balogh and P. Bagchi. "Analysis of red blood cell partitioning at bifurcations in simulated microvascular networks". In: *Phys. of Fluids* 30 (2018), p. 051902.

[184] V. Doyeux et al. "Spheres in the vicinity of a bifurcation: elucidating the Zweifach–Fung effect". In: *J. Fluid Mech* 674 (2011), pp. 359–388.

[185] J.L.M. Poiseuille. "Recherches sur les causes du mouvement du sang dans les vaisseaux capillaires". In: *C.R. Acad. Sci.* 6 (1835), pp. 554–560.

[186] J.O Barber et al. "Deformation and partitioning in microvessel bifurcation". In: *Ann. of Bio. Eng.* 36 (2008), pp. 1690–1698.

[187] R.B. Francis. "Large-vessel occlusion in sickle cell disease: Pathogenesis, clinical consequences, and therapeutic implications". In: *Med. Hypotheses* 35 (1991), pp. 88–95.

[188] X. Li et al. "Biomechanics and biorheology of red blood cells in sickle cell anemia". In: *J. Biomech.* 50 (2017), pp. 34–41.

[189] S. Chien et al. "Model studies on distributions of blood cells at microvascular bifurcations". In: *Am. J. Physiol. Heart Circ. Physiol.* 248.4 (1985), H568–H576.

[190] T.F. Sherman. "On connecting large vessels to small. The meaning of Murray's law". In: *J. Gen. Physiol.* 78 (1981), pp. 431–453.

[191] P. Gaehtgens. "Distribution of flow and red cell flux in the microcirculation". In: *Scand J Clin Lab Invest.* 156 (2009), pp. 83–87.

[192] S. Chien et al. "Shear-dependent de-formation of erythrocytes in rheology of human blood". In: *Am. J. Physiol.* 219 (1970), 136–142.

[193] V. Viktova et al. "Micro-macrolink in rheology of erythrocyte and vesicle suspensions". In: *Biophys. J.* 95 (2008), p. 33.

[194] A Pries, N Neuhaus, and P Gaehtgens. "Blood viscosity in tube flow: dependence on diameter and hematocrit". In: *Am.J.Physiol.* 20 (1989), H1770–H1778.

[195] E. Kaliviotis and M. Yianneskis. "An energy-rate based blood viscosity model incorporating aggregate network dynamics". In: *Biorheology* 46 (2009), pp. 487–508.

[196] D. A. Fedosov et al. "Predicting human blood viscosity in silico". In: *PNAS* 108 (2011), 11772–11777.

[197] D. Flormann et al. "Is there a role of C-reactive protein in red blood cell aggregation?" In: *Int. Jnl. Lab. Hem.* 37 (2015), pp. 474–482.

[198] V. Viktova et al. "Fully automated digital holographic processing for monitoring the dynamics of a vesicle suspension under shear flow". In: *Biophys. J.* 95 (2008), p. 33.

[199] N. Callens et al. "Hydrodynamic lift of vesicles under shear flow in microgravity". In: *Europhys. Lett.* 83 (2008), p. 24002.

[200] T. Podgorski, G. Coupier, and C. Minetti. *Red Blood Cell Dynamics: The Contribution of Microgravity in the BIOMICS Project*. Intechopen, 2020.